Novel Chemistries and Materials for Grid-Scale Energy Storage: Quinones and Halogen Catalysis

Citation	No citation.
Accessed	February 19, 2015 2:12:09 PM EST
Citable Link	http://nrs.harvard.edu/urn-3:HUL.InstRepos:11744432
Terms of Use	This article was downloaded from Harvard University's DASH repository, and is made available under the terms and conditions applicable to Other Posted Material, as set forth at http://nrs.harvard.edu/urn-3:HUL.InstRepos:dash.current.terms-of-use#LAA

HARVARD UNIVERSITY
Graduate School of Arts and Sciences

DISSERTATION ACCEPTANCE CERTIFICATE

The undersigned, appointed by the

School of Engineering and Applied Sciences

have examined a dissertation entitled:

"Novel Chemistries and Materials for Grid-Scale Energy Storage: Quinones and Halogen Catalysis"

presented by : Brian Thomas Huskinson

candidate for the degree of Doctor of Philosophy and here by certify that it is worthy of acceptance.

Signature ______________________
Typed name: Prof. M. Aziz

Signature Frans Spaepen
Typed name: Prof. F. Spaepen

Signature ______________________
Typed name: Prof. R. Gordon

Signature ______________________
Typed name: Prof. S. Ramanathan

Date: *January 6, 2014*

Novel Chemistries and Materials for Grid-Scale Energy Storage: Quinones and Halogen Catalysis

A DISSERTATION PRESENTED
BY
BRIAN THOMAS HUSKINSON
TO
THE SCHOOL OF ENGINEERING AND APPLIED SCIENCES

IN PARTIAL FULFILLMENT OF THE REQUIREMENTS
FOR THE DEGREE OF
DOCTOR OF PHILOSOPHY
IN THE SUBJECT OF
APPLIED PHYSICS

HARVARD UNIVERSITY
CAMBRIDGE, MASSACHUSETTS
JANUARY 2014

Thesis advisor: Michael J. Aziz Brian Thomas Huskinson

Novel Chemistries and Materials for Grid-Scale Energy Storage: Quinones and Halogen Catalysis

Abstract

In this work I describe various approaches to electrochemical energy storage at the grid-scale. Chapter 1 provides an introduction to energy storage and an overview of the history and development of flow batteries. Chapter 2 describes work on the hydrogen-chlorine regenerative fuel cell, detailing its development and the record-breaking performance of the device. Chapter 3 dives into catalyst materials for such a fuel cell, focusing on ruthenium oxide based alloys to be used as chlorine redox catalysts. Chapter 4 introduces and details the development of a performance model for a hydrogen-bromine cell. Chapter 5 delves into the more recent work I have done, switching to applications of quinone chemistries in flow batteries. It focuses on the pairing of one particular quinone (2,7-anthraquinone disulfonic acid) with bromine, and highlights the promising performance characteristics of a device based on this type of chemistry.

To my parents, for their continued love and support.

Contents

Acknowledgments

I OWE A DEBT OF GRATITUDE to so many different people who were there for me in one way or another during my time at Harvard. Michael Aziz, my advisor, is deserving of first recognition. I will never forget how supportive Mike was, both professionally and personally. Mike displays a deep and genuine interest in his students that is impossible not to recognize. He also holds both himself and his students to a very high standard, and for that I am grateful. I am without question a better scientist because of the countless hours he has invested in me.

I'd also like to thank the rest of my thesis committee: Roy Gordon, Frans Spaepen, and Shriram Ramanathan. I took classes from the latter two (AP 282 with Prof. Spaepen and AP 218 with Prof. Ramanathan), and I learned a lot in both. AP 282 turned out to be the most difficult course I took in graduate school, but also one of the most rewarding. Prof. Gordon also deserves special mention, as he has been a wonderful mentor over the past year and a half or so when the quinone work really began to blossom.

Regarding research, I owe thanks to a number of collaborators, starting with Profs. Roy Gordon and Alán Aspuru-Guzik, who were both active on the Dept. of Energy ARPA-E grant that funded the quinone-related work discussed here. I'd also like to acknowledge their group members who were active on the project: Süleyman Er (who also contributed to the chlorine redox catalyst work), Changwon Suh, Lauren Hartle, Cooper Galvin, Rachel Burton, Bilen Aküzüm, and Xudong Chen. I'd also like to thank some of our collaborators at Sustainable Innovations, including Trent Molter, Josh Preston, and Phillip Baker.

Within the Aziz group, I'd first like to acknowledge those whom I collaborated with directly, beginning with Jason Rugolo. He served as a mentor to me early in my Ph.D., and I enjoy our friendship to this day. I'd also like to thank Dr. Michael Marshak, a postdoc in the group whose knowledge of chemistry greatly sped up our work on quinones. Michael Gerhardt, a graduate student in the group, was a dedicated contributor to the quinone work as well. As for the rest of the Aziz group, thanks to Dan Recht, Charbel Madi, Joy Perkinson, Austin Akey, and David Pastor. The ideas and helpful hands contributed by each of you are greatly appreciated.

To friends and family: I cannot express enough gratitude for the support you have given me. I'm fortunate to have lived a very blessed life thus far, and in no small part due to each of you. First, a thanks to my parents, to whom I dedicated this thesis and who have been truly wonderful to me. Your tireless support and encouragement, each of you in your own ways, is inspiring. To Emily, Matthew, and Megan: you are the best brothers and sisters anyone could hope for. To my grandparents, aunts, uncles, and cousins: your support and love has been remarkable. To my friends from Harvard: these were a great few years in no small part to you. Alex, you've been a wonderful girlfriend to me, and your enthusiasm always brightens my day. Kian, you are the man. One of the things I've least looked forward to about finishing graduate school is knowing that we won't be hanging out on a regular basis afterwards. I'd also like to mention Roger Diebold, who sat at the desk next to me for much of my Ph.D., and who I had more than a few fun nights out with. Same goes for Bill and Amanda Bonificio. Bill and I got in the habit of sharing a "spirited" weekly conversation during the football season that generally ended with Bill lamenting what a poor athlete Eli Manning is. I'd also like to mention Matt and Kate Pharr, who, between hosting a crawfish boil, Super Bowl and March Madness parties, and Matt and I placing a few misguided wagers, served to make these four and a half years that much more enjoyable. To my friends from Flower Mound: we always have a good time, and I always look forward to seeing you. Maybe I'll be back in Texas when this thing is turned in! To my friends from Yale: those truly were the shortest, gladdest years, and I cherish each of our friendships. I'd also like to acknowledge a number of people on Harvard staff, including Barbara Sewall, Stan Cotreau (of the machine shop), and Frank Molea (rest in peace).

For three years of graduate school, I was funded by a Graduate Research Fellowship awarded by the National Science Foundation. Other project funding came from the Dept. of Energy ARPA-E program. I also relied on resources provided by the Harvard Center for Nanoscale Systems.

Listing of figures

Listing of tables

Listing of acronyms

AQDS	9,10-anthraquinone-2,7-disulfonic acid
$AQDSH_2$	9,10-anthrahydroquinone-2,7-disulfonic acid (reduced form of AQDS)
CAES	compressed air energy storage
CER	chlorine evolution reaction
CRR	chlorine reduction reaction
DSA	dimensionally stable anode
EP	engineering parameter
GDE	gas diffusion electrode
OER	oxygen evolution reaction
OP	operating parameter
ORR	oxygen reduction reaction
PEM	proton exchange membrane
PHES	pumped hydroelectric storage
PTFE	poly-tetrafluoroethylene (Teflon)
QBFB	quinone-bromide flow battery
RDE	rotating disk electrode
rHBFC	regenerative hydrogen-bromine fuel cell
SEM	scanning electron microscope
SHE	standard hydrogen electrode
SOC	state-of-charge
XRD	x-ray diffraction

1

Introduction

The way we produce electricity is changing. Growth in the use of intermittent renewable sources like wind and solar is impressive (see Figure 1.1), but it places new and interesting pressures on the grid. In particular, we are largely accustomed to having foreseeable power output from generators while having uncertain demand from end users. Wind and solar introduce more

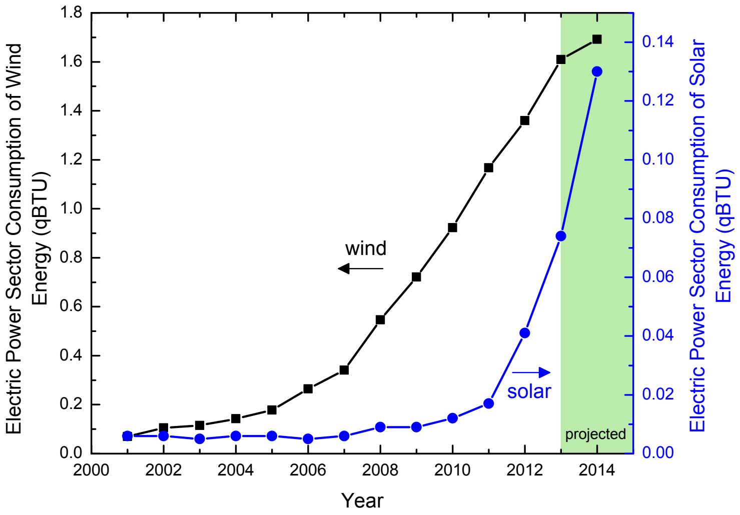

Figure 1.1. Growth in wind and solar electricity production [1]. Note the large difference in the scale of the y-axes.

uncertainty in that their power output is largely unpredictable, leading to the presence of stochastic elements in both the demand *and* supply profiles. Thus, as the fraction of total generation from renewables grows, so will many of the uncertainties associated with managing the grid. This is the essence of why grid-scale energy storage is important: energy storage allows for predictability and reliability that otherwise would not exist.

In general, it is not economically viable to store electricity on a large scale today [2]. All currently developed storage technologies have serious drawbacks that prevent their widespread adoption. By far the most prevalent storage option in use today is pumped hydroelectric storage (PHES), which is based on the simple principle of pumping water uphill with excess electricity and then running the water downhill through hydroelectric turbines to convert the stored potential energy back into electricity. Currently installed PHES capacity exceeds 127 GW worldwide, representing over 99% of *all* storage [3]. PHES, however, has massive land usage requirements, serious ecological consequences (due to the fact that dams and reservoirs are required, often affecting sensitive aquatic ecologies), and requires the appropriate topography (typically mountainous regions). The next most prevalent storage technology is compressed air energy storage (CAES), which is based on the principle of pumping air into pressurized caverns, with about 0.44 GW of installed capacity worldwide [3]. CAES's primary drawbacks are geographical constraints (the appropriate crustal geologies are needed to form the underground caverns) and poor cycling efficiency. The third most prevalent storage technology is the sodium-sulfur battery, with 0.32 GW installed capacity [3]. This type of battery suffers from efficiency concerns and cost concerns (they operate near 300 °C so they require expensive insulation and housing; the materials used are also quite hazardous). Other technologies, such as lead-acid batteries, nickel-cadmium batteries, flywheels, lithium-ion batteries, and redox flow batteries have been installed in select applications, but their usage is very limited. They all, at this point, suffer from cost constraints: they are simply too expensive for large-scale implementation. Some of these technologies (Li-ion, vanadium redox flow batteries) may also suffer from resource constraints in the future [4].

When these storage capacity numbers are compared to total installed electric generation capacity in the world, which well exceeds 2,300 GW [5], it becomes apparent that electricity storage is still in its nascent stages. Despite these current limitations, many different players are pursuing research and development of a variety of storage technologies. The reason is simple: there is a large number of potential applications for storage devices, and the market for storage is expected to expand rapidly in the coming years.

The particular applications of a storage device depend on the particular properties of each device [6]. Some devices, such as supercapacitors, can be used to store small amounts of energy but deliver it extremely quickly (i.e. with very high powers), allowing for management on the micro- to millisecond time scale. Devices like these can be used for frequency regulation, for example. Other devices, like flow batteries, have response times in the seconds time scale and are therefore more appropriate for applications like peak shaving and load leveling: absorbing excess production when demand is weak and releasing that production when demand is high. Overviews of these applications can be found elsewhere [6–9].

The focus of this dissertation will be on flow batteries that place a premium on a particular set of metrics: high performance (high current and power densities, which translate to low $ kW^{-1}), low energy costs (low $ kWh^{-1}), and high efficiencies. Indeed, it has been argued that capital cost (both $ kW^{-1} and $ kWh^{-1}) is the single most important metric to use when considering a storage device [8], and the work that follows focuses exclusively on systems that have the possibility of achieving very low costs.

This dissertation essentially consists of two parts: halogen chemistries in electrochemical devices (Chapters 2-4) and organic chemistries in electrochemical devices (Chapter 5). All of these chapters are pushing towards the same goal: the development of an inexpensive, commercially viable flow battery. Chapter 2 focuses on a device that pairs chlorine on the positive electrode with hydrogen on the negative electode, making a cell with a 1.36 V equilibrium potential. This so-called hydrogen-chlorine regenerative fuel cell is capable of performing with remarkable efficiencies and power densities, and, as is detailed in the chapter, the cell we designed and tested is the best performing cell of its kind ever built: a peak galvanic power density exceeding 1.6 W cm^{-2} and a power density exceeding 0.5 W cm^{-2} at 90% voltage efficiency were achieved, despite very low catalyst loadings (< 0.15 mg Ru cm^{-2}). The cell relies on a novel catalyst for the chlorine redox reaction: a mixed oxide alloy consisting of cobalt oxide doped with ruthenium at about 10 mol% (more formally written as $(Ru_{0.09}Co_{0.91})_3O_4$). The effects of Cl_2 gas pressure, electrolyte acid concentration, and hydrogen electrode humidification are also reported, along with substantive comparisons to the H_2-Cl_2 fuel cell model of Rugolo *et al.* [10]. The content of this chapter is based primarily on work published in Huskinson *et al.* [11].

Chapter 3 focuses on the development and testing of various metal oxide alloys in our group, with the goal of finding effective chlorine redox catalysts with minimal precious metal content. Our search was inspired by the use of so-called dimensionally-stable anodes, or DSAs, in the industrial production of chlorine. Typical DSAs are composed of mixed oxides of TiO_2 and RuO2, with about a 30 mol% Ru content $(Ru_{0.3}Ti_{0.7}O_2)$ [12]. Given this starting point, we explore an expanded composition space to find particular oxide alloys that were promising for our application. This chapter details the use of alloys of ruthenium with cobalt, nickel, titanium, tin, and manganese oxides. Half-cell measurements are done to determine exchange current densities for the different oxide materials. It is found that ruthenium-cobalt oxide alloys are generally the most effective, demonstrating excellent catalytic ability and good stability, but other alloys, including ruthenium-nickel in particular, are capable of performing comparably or even slightly better at certain compositions. X-ray diffraction results of a subset of these oxides are also presented.

Chapter 4 introduces the hydrogen-bromine flow battery, detailing the development of a performance model of this kind of cell. Modeling work began on the hydrogen-chlorine cell (the subject of Chapter 5 in Jason Rugolo's thesis [13]), and that work is expanded and applied to the hydrogen-bromine cell here. The interesting and sometimes subtle effects of temperature, electrolyte composition, electrode performance, and other parameters on cell performance are detailed, highlighting the excellent performance that these devices are capable of achieving. Our model differs from previous work in two key ways: (1) we include the effects of temperature on equilibrium potentials, membrane resistances, electrode activation kinetics, and mass transport of species to and from the electrode surface, and (2) we systematically vary the cell operating parameters, such as temperature and electrolyte composition, while also varying cell engineering parameters, discussed within the chapter, to identify performance "sweet spots." The large parameter space we explore is unrivaled in the literature. The content of this chapter is based primarily on work published in Ref. [14].

Chapter 5 focuses on the use of a class of organic molecules known as quinones in an energy storage device. Quinones are compelling for a number of reasons: they are ubiquitous in nature, they have the potential to be very inexpensive to manufacture at a large scale, they rely exclusively on earth-abundant elements, they exhibit excellent redox kinetics, and they have reasonably high solubilities in water. This chapter discusses our work with quinones, detailing initial investigations and finally moving into our selection of one particularly promising molecule: 2,7-anthraquinone disulfonic acid (AQDS). Half-cell measurements were done on AQDS, allowing us to determine its diffusion coefficient, the rate constant for its redox reaction on a glassy carbon electrode, and the associated transfer coefficient. Fittingly, this chapter ends by uniting the halogen work with the quinone work, detailing the development of an anthraquinone-bromine flow battery. Two iterations of this battery (so-called "Generation 1" and "Generation 2" cells) are described. The batteries use inexpensive carbon electrodes, combining the AQDS/$AQDSH_2$ couple with the Br_2/Br^- redox couple, and the Generation 2 cell yields a peak galvanic power density exceeding 0.6 W cm^{-2} at 1.3 A cm^{-2}. Cycling of the QBFB showed 99.99% storage capacity retention per cycle. Much of the content of this chapter is based on work published in Ref. [15].

Chapter 6 summarizes the work and discusses some possible future directions for research.

2

The Hydrogen-Chlorine Fuel Cell: Experimental Advances

Hydrogen-halogen electrochemical devices are of interest for a number of applications. Flow batteries utilizing these chemistries could be used for grid-scale electrical energy storage

[6, 9, 16, 17]. Cells that utilize either chlorine (Cl_2) or bromine (Br_2) have generated particular interest [18–23]. Fluorine has limited viability due to its highly corrosive and toxic nature, iodine is limited due to the low equilibrium potential associated with iodine's redox reaction (+0.54 V vs. a standard hydrogen electrode (SHE)), and astatine is both radioactive and phenomenally rare. Figure 2.1 is a schematic showing how a cell using Cl_2 would operate in both electrolytic (charge) and galvanic (discharge) modes, using either a serpentine (a) or interdigitated (b) flow field design. Note that we use the term "regenerative fuel cell" to refer to an electrochemical cell designed for operation in both galvanic and electrolytic modes in steady state, in which the reactants and products are fluids and their activities are time-independent. If one were to take a regenerative fuel cell and add external storage tanks to hold the reactants and products, thereby forming a closed system to be charged and discharged, then even when the cell is operated at constant current, the reactant and product activities become functions of time, or state of charge. We refer to such a device as a "flow battery." Our own device is capable of being operated in either of these manners: in the results reported here the gas pressures are constant but the hydrochloric acid concentration is not, and we do not collect the products and recycle them. Although it has some of the characteristics of both a flow battery and a regenerative fuel cell, it has more of the characteristics of the latter.

In addition to grid-scale electricity storage, the hydrogen-chlorine galvanic cell is the most immature component of an electrochemically accelerated chemical weathering process that could transfer CO_2 from the atmosphere to the ocean without ocean acidification [24, 25]. When used in this application, the device operates only in galvanic mode.

Because of relatively facile chlorine redox kinetics, H_2-Cl_2 cells are capable of operation with little activation loss associated with the chlorine electrode, in marked contrast to the

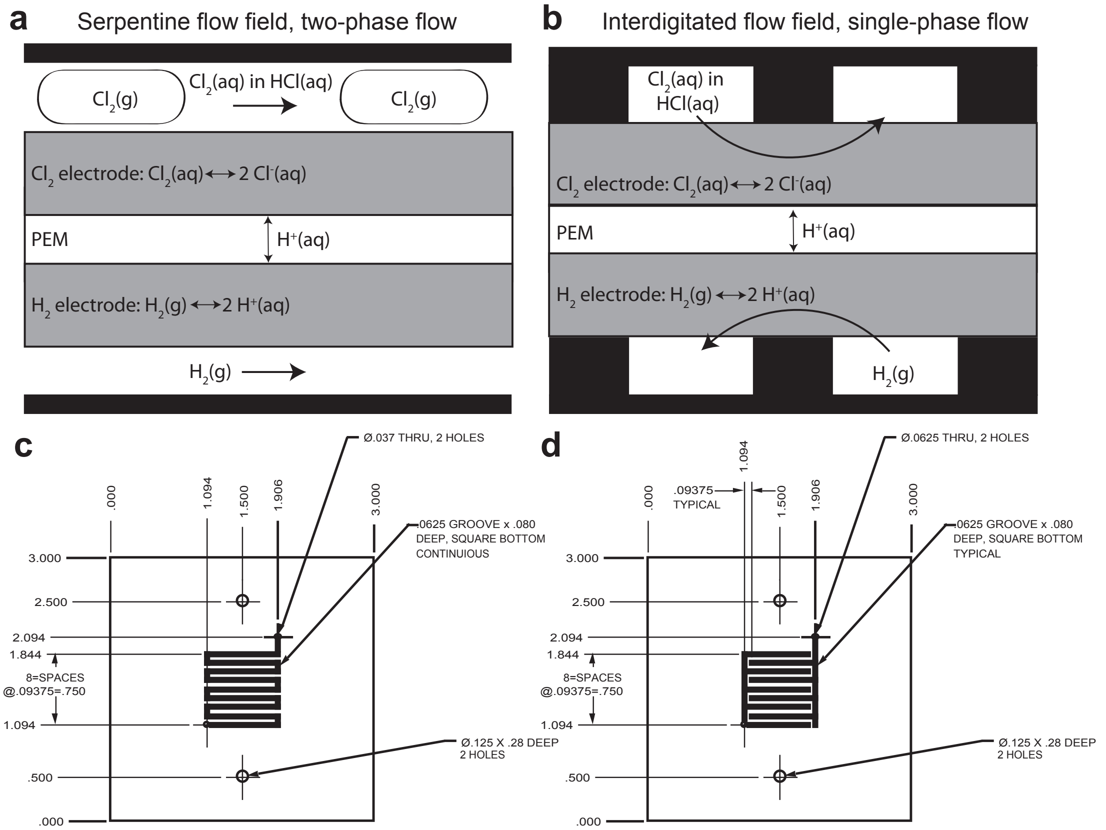

Figure 2.1. Schematics of a regenerative hydrogen-chlorine fuel cell: (**a**) Our fourth-generation cell utilizing serpentine flow fields, showing a cross-section along the length of a channel. In charge mode, hydrochloric acid (HCl) is electrolyzed to form Cl_2 on the anode side of the cell and H_2 on the cathode side. This process is not spontaneous, so a potential must be applied across the electrodes. In discharge mode, H_2 and Cl_2 are fed into the anode and cathode sides of the cell, respectively, spontaneously forming HCl and generating an external current. The proton exchange membrane (typically Nafion) must conduct H^+ ions in both modes (but the direction of conduction switches); (**b**) our fifth-generation cell utilizing interdigitated flow fields, showing a cross-section through the channels. Operation is identical to (a) except the fluid on the chlorine side is a single-phase liquid (HCl saturated with Cl_2) and the interdigitated design forces convection of the reactants through the electrode materials. (**c**) drawing of the serpentine flow field with exact dimensions; (**d**) drawing of the interdigitated flow field with exact dimensions.

hydrogen-oxygen fuel cell, in which sluggish oxygen reduction kinetics lead to a substantial activation overpotential. For comparison, measured values for the exchange current density for Cl_2 reduction on both smooth Pt and RuO_2 are 10 mA cm^{-2} and 0.01 mA cm^{-2} [26], respectively, whereas a comparable figure for O_2 reduction on Pt is 10^{-6} mA cm^{-2} [27].[i] Exchange current densities for the hydrogen oxidation/evolution reactions can be as high as 600 mA cm^{-2} on structured Pt electrodes [29], so no significant activation losses should be expected at the hydrogen electrode.

Fast reaction kinetics at both electrodes, along with other advantages such as rapid mass transport, mean that hydrogen-chlorine cells have the potential to operate at high current densities with high electric-to-electric efficiencies. Work on hydrogen-chlorine fuel cells began in the 1970s, focusing on applications in both grid-scale energy storage [20, 22, 30, 31] and in high-power applications for select missile and space programs [32, 33]. Power densities exceeding 0.3 W cm^{-2} were achieved in the late 1970s, with round-trip efficiencies at 300 mA cm^{-2} of up to 75% [20]. Subsequently, power densities approaching 0.5 W cm^{-2} were reached [28]. Materials stability issues limited the practical application of earlier cells, e.g. Pt dissolution in hydrochloric acid [28]. There is still a significant incentive to improve electrode materials, particularly by reducing costs through the decreased usage of precious metals. Both studies mentioned above relied on precious metal catalysts. Yeo *et al.* [20] used a ruthenized graphite electrode, where loadings are not reported, while Thomassen *et al.* [28] tested both 0.5 mg Pt cm^{-2} and 1.0 mg Rh cm^{-2} commercial gas-diffusion electrodes (GDEs), neither of which was stable over long time periods.

Due to the success of dimensionally stable anodes (DSAs) in the industrial production of

---

[i] It is worth noting that, in the presence of chlorine, Pt can dissolve by forming hydroplatinic acid (H_2PtCl_6), so Pt is not a suitable material for use as a chlorine electrode material [28].

chlorine in the chlor-alkali process, RuO_2-based compounds appear promising as electrode materials for use in a halogen electrode. A typical DSA composition used in the chlor-alkali process is $(Ru_{0.3}Ti_{0.7})O_2$ [12]. When DSAs were first developed, they represented a marked improvement over graphite as an electrode material in membrane cells, since graphite would oxidize and disintegrate with operation, effectively clogging the cell [34]. Thus, because of their remarkable stability, DSAs enabled the chlor-alkali industry to move away from mercury cells (which rely on large amounts of mercury in operation) to more efficient membrane cells by vastly improving the operational characteristics of the latter.

After the development of DSAs, work was done by other groups, perhaps most notably by S. Trasatti, exploring the use of mixed oxides other than RuO_2-TiO_2 in the anodic evolution of chlorine [35–38]. DSA oxide alloys have typically been examined only in the anodic direction (i.e. oxidizing Cl^- to Cl_2) and at relatively high pH (typically around pH 2-4), which are the conditions around which chlor-alkali membrane cells operate [34, 35, 37]. Despite these operational differences, we were able to use the work cited above as a starting point for developing our own catalyst materials. Mondal *et al.* examined both the cathodic and anodic behavior of a couple different ruthenium oxide alloys in both hydrochloric and hydrobromic acids near pH 0 and identified the composition near $(Ru_{0.1}Co_{0.9})_3O_4$ as particularly promising for chlorine redox catalysis [39]. To fabricate the cell reported here, we developed a method of depositing this electrocatalyst onto the fibers of Toray carbon paper. In this work we demonstrate the successful operation of an $(Ru_{0.09}Co_{0.91})_3O_4$ alloy as a catalyst material for a regenerative hydrogen-chlorine fuel cell. We observed negligible activation losses, even with precious metal loadings as low as 0.15 mg Ru cm^{-2}. In our fourth-generation cell (the previous three generations were developed by Jason Rugolo and are discussed in his thesis [13]), we observed a maximum cell power density exceeding 1 W cm^{-2}, which is twice as large as values previously reported, values that also relied on significantly higher precious metal loadings on the Cl_2-side of the cell. Furthermore, we observed a power density of approximately 0.4 W cm^{-2} at 90% galvanic efficiency. This is an important figure of merit when considering these devices for grid-scale energy storage, where round-trip electric-to-electric efficiencies are very important. The effects of Cl_2 gas pressure, electrolyte acid concentration, and hydrogen electrode humidification are also reported, along with substantive comparisons to the H_2-Cl_2 fuel cell model of Rugolo *et al.* [10].

The fifth-generation cell further improves on these metrics by including several important changes: (1) the flow fields were switched from a serpentine design to an interdigitated design, leading to vastly improved mass transport behavior due to the forced convection this design induces, (2) electrodes were stacked 6x on the chlorine side of the cell, leading to a thicker electrode, greater surface area, and a larger flow path, (3) Nafion 211 (25 μm thick) was used instead of Nafion 212, leading to reduced ohmic losses, and (4) flow into the cell consisted of a single-phase liquid flow of HCl saturated with Cl_2 gas, as opposed to the two-phase flow seen in Figure 2.1a that was used in the fourth-generation cell. Practically, this last step had to be taken due to the constraints of using a diaphragm pump, which is poorly equipped to deal with two-phase flow (as opposed to the centrifugal pump used in the fourth-generation design), but it may have also had the effect of improving membrane hydration. All of these changes led to significantly improved performance, with a maximum power density exceeding 1.65 W cm^{-2} and a power density at 90% galvanic efficiency in excess of 0.5 W cm^{-2}. To our knowledge, these data represent the best performance of any halogen-based fuel cell ever reported in the literature, including results on bromine-based devices.

2.1 EXPERIMENTAL METHODS

ELECTRODE SYNTHESIS

The chlorine-side electrode consisted of a Toray carbon paper coated with a single-phase $(Ru_{0.09}Co_{0.91})_3O_4$ alloy synthesized using standard wet chemical techniques. Before coating, the following protocol was used to clean the carbon paper: (1) several rinses in DI-H_2O (18.2 MΩ ultrapure, Millipore), (2) sonication in isopropyl alcohol (VWR International) for 10 min., (3) soak in hot (80 °C) 50% H_2SO_4 (reagent grade, Sigma Aldrich) for 30 min., (4) soak in hot (80 °C) 6 M hydrochloric acid (HCl, ACS reagent grade, Sigma Aldrich) for 30 min., and (5) several rinses in DI-H_2O. The individual pieces of carbon paper were then dried and weighed. To deposit the catalyst material, a 2 cm^2 square of cleaned carbon paper was dipped in a solution of 0.1 M $RuCl_3$ + 1 M $CoCl_2$ in 12.1 M HCl, dried at 90 °C for 15 minutes, then oxidized in an air furnace at 350 °C (with a 45 min. ramp to 350 °C and a 60 min. hold at this temperature). This procedure was repeated twice to achieve a total Ru loading of 0.15 mg Ru cm^{-2}. The hydrogen-side electrode used 2 cm^2 of either a standard ELAT®gas diffusion electrode (GDE) with a Pt loading of 0.5 mg cm^{-2} (Fuelcellstore.com), or a reformate anode utilizing a finely divided platinum/ruthenium alloy on carbon black (loading of about 0.6 mg Pt-Ru cm^{-2}, Alfa Aesar). Little difference in performance was seen between the two. The fifth-generation cell utilized identical materials as those just described, except, on the chlorine side of the cell, six electrodes were stacked on top of one another to increase the total electrode thickness. Micrographs of the chlorine electrode were obtained using a scanning electron microscope (SEM, Ultra55, Zeiss).

Fuel cell construction and test bench characteristics

The fuel cells studied here comprised a mixture of commercially available and custom-made components. Figure 2.2a shows an image of the actual cell and Figure 2.2b shows a schematic of the cell architecture. Circular endplates were machined out of solid aluminum. 3" x 3" pyrolytic graphite blocks with either single-serpentine flow channels (channel width = 0.0625 in., channel depth = 0.08 in., landing between channels = 0.031 in., Fuel Cell Technologies, Inc.) or interdigitated flow channels (channel width = 0.0625 in., channel depth = 0.08 in., landing between channels = 0.031 in.) were used as current collectors. Nafion®211 (25 μm thick) or 212 (50 μm thick) was used as a proton-exchange membrane (PEM, Alfa Aesar), and poly-tetrafluoroethylene (PTFE) gasketing was used to seal the cell assembly. Before insertion into the cell, the following procedure was used to pretreat the PEM: (1) immersion in 85 °C DI-H_2O for 15 min., (2) immersion in 5% H_2O_2 (ACS reagent grade, Mallinckrodt Chemicals) for 30 min., (3) rinse with DI-H_2O, (4) ion-exchange twice in 0.05 M H_2SO_4 for 30 min. each, and (5) rinse in DI-H_2O four times, each for 15 min. Membranes were stored in DI-H_2O when not in use.

Six bolts (3/8"-16) torqued to 10.2 Nm completed the cell assembly, and PTFE tubing was used to transport reactants and products into and out of the cell. Holes bored into the aluminum endplates allowed for the insertion of thermometers into each endplate to monitor the cell temperature. The cell was kept on a hotplate for temperature control. Furthermore, the liquid electrolyte reservoir was heated to improve thermal management. The system, when operating, holds about 0.8 L of electrolyte. All measurements were conducted in a test bench designed and

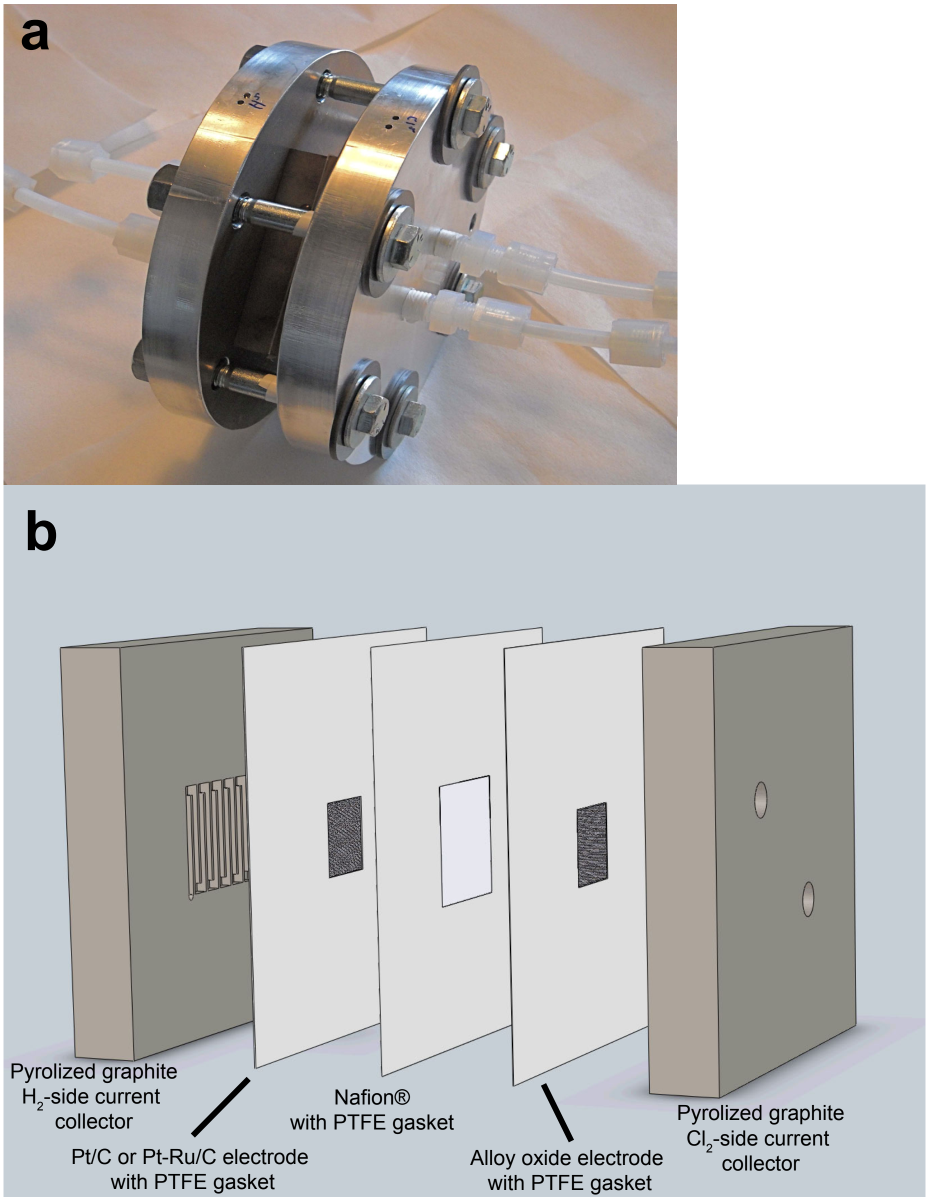

Figure 2.2. (**a**) Image of the actual cell, showing the circular aluminum endplates and the square graphite current collectors in between and (**b**) schematic showing the square internal components of the fuel cell. The circular aluminum endplates are not shown in (b). This hardware was used in both the fourth- and fifth-generation cells.

assembled by Sustainable Innovations, LLC.[ii] The bench exhausted to a fume hood, and all reactant gases (H_2 and Cl_2) were stored inside the hood. No exposed gas lines existed outside this negative pressure environment, so that, if there were a line rupture or gasket failure along any portion of the test set-up, no harmful gases could enter the researchers' airspace. This is a particularly important feature of our experimental setup, as we are using chlorine at both high temperatures and high pressures. Figure 2.3 shows an image of the test bench apparatus.

H_2 gas (zero grade, 99.99%, Matheson Tri-Gas) was fed to the hydrogen side of the cell. For non-humidified H_2 electrode experiments, the dry gas stream was fed directly to the cell. In studying the effects of humidification, the dry H_2 gas stream was first bubbled through a heated reservoir of DI-H_2O before entering the cell. The reservoir was maintained about 3 $^\circ$C cooler than the actual cell to prevent condensation of H_2O within the cell, which could potentially flood the hydrogen electrode. H_2 flow rates were maintained between 50-100 mL min^{-1}. Assuming the equilibrium vapor pressure of water is reached in gas exiting the bubbler, and assuming an ideal mixture of gases, the humidity level is independent of the hydrogen gas pressure and is solely a function of temperature. The water vapor pressure entering the cell therefore ranges from about 0.35 psia (near 20 $^\circ$C) to 1.8 psia (near 50 $^\circ$C; values calculated using the Antoine equation).

On the chlorine side, a two-phase flow was fed into the cell (see Figure 2.1a) for the fourth-generation cell results and a single-phase liquid flow was fed into the cell for the fifth-generation cell results. The liquid phase in both cells consisted of dilute hydrochloric acid saturated with $Cl_2(aq)$. In the fourth-generation cell, bubbles of Cl_2 gas (high purity, 99.5%, Matheson) accompanied this liquid phase (by teeing the pump outlet line into the Cl_2 gas flow

---

[ii] I made a number of important changes to this test bench, including the addition of a humidifier and the use of different pumps.

Figure 2.3. Image of the test bench designed by Sustainable Innovations. The entire cavity of the bench is held under negative pressure for safety reasons.

line, two-phase flow was achieved). Having a liquid phase meant there was continuous transport of H_2O into the cell and to the membrane surface, thereby keeping it hydrated. This allowed for the use of dry H_2 gas on the hydrogen side (note that the effect of humidifying the H_2 side is discussed later). The cell pressure was controlled via needle valves on the outlet tubes from the cell, and, in general, the H_2 side pressure was maintained at 5 psi higher than the Cl_2 side of the cell. Either a centrifugal pump (fourth-generation) or a diaphragm pump (fifth-generation) was used to circulate HCl into and out of the Cl_2 side of the cell. It is worth noting that, because the electrolyte is continuously recirculated, the HCl concentration increases with time as current is being drawn from the cell. Because the electrode areas are relatively small (2 cm^2), though, the cell has to run for long periods of time before there are significant concentration changes.[iii] Acid flow rates were maintained around 100 mL min^{-1}. for all tests. As part of the results reported here, we test cell performance at three different values of the initial HCl concentration (0 M, 1 M, and 2 M). All fifth-generation cell data were collected with a 1 M HCl electrolyte and a humified H_2 electrode.

FUEL CELL MEASUREMENTS

Before introducing either reactant into the cell, a nitrogen (N_2, ultra high purity, Matheson) purge of the entire system was done, taking the system up to operating pressures and temperatures to ensure no leaks were present and to flush any O_2 from the system. Reactants were then introduced on both sides of the cell, making sure that no significant pressure differential (i.e. $>$10 psi) develops across the membrane as the reactant pressures are increased. Once reactant flows, pressures, and the system temperature had stabilized, a DC electronic load

---

[iii] Running at 1 A cm^{-2}, for example, it would take nearly 11 hours of operation to change the electrolyte concentration by 1 M.

(Circuit Specialists, Inc.) was used to draw current from the cell. An independent Fluke multimeter was used to make voltage readings across the endplates of the cell. For collection of voltage vs. current density curves, a given current would be drawn from the cell, and the voltage, once stabilized, would be read from the multimeter. Typically, the voltage stabilized immediately, but, as the limiting current density was approached, the voltage values became much less stable, leading to measurement difficulties. Measurements were repeated at least three times (and sometimes up to five) to reduce this error. For electrolytic operation, the cell was connected to a DC regulated power supply (Circuit Specialists, Inc.) to apply a potential across the cell. A multimeter was again used for independent voltage measurements.

Measures of efficiency

It is important to define a number of efficiency terms that appear throughout this dissertation. First, the voltage efficiency has the following definition:

$$\text{cell voltage efficiency} = \begin{cases} \frac{E(i)}{E_{eq}} & : i \geq 0 \quad \text{(galvanic)} \\ \frac{E_{eq}}{E(i)} & : i \leq 0 \quad \text{(electrolytic)} \end{cases} \tag{2.1}$$

where E_i is the cell voltage during operation and E_{eq} is the cell equilibrium potential. At zero current density, the voltage efficiency is 100%. The coulombic efficiency is defined for an arbitrary process r occurring at an electrode in the following way [40]:

$$\text{coulombic efficiency for } r\text{th process} = \frac{Q_r}{Q_{total}} \tag{2.2}$$

where Q_r is the number of coulombs involved in the rth process and Q_{total} is the total number of coulombs transferred at the electrode. A difference between Q_r and Q_{total} arises when there are other reactions (say, processes s and t) occurring at the electrode. Note that one can divide both Q_r and Q_{total} by time to give i_r and i_{total}, the current for the rth reaction and the total current, respectively, which provides an "instantaneous" coulombic efficiency as opposed to a cumulative coulombic efficiency. This form of Equation 2.2 is more useful when dealing with devices that operate at steady-state, like fuel cells, as opposed to flow batteries which have a fixed amount of charge capacity. For the purposes of this chapter, process r is considered to be the chlorine redox reaction, while process s can be considered to be oxygen evolution. Minimizing the extent of oxygen evolution is an important consideration in a hydrogen-chlorine regenerative fuel cell.

The energy conversion efficiency is the product of the voltage efficiency and coulombic efficiency, and the round-trip efficiency of the device is the product of the energy conversion efficiency in galvanic mode and the energy conversion efficiency in electrolytic mode.

2.2 Results and Discussion

Electrode characterization

Micrographs of the electrodes as deposited can be seen in Figure 2.4. The $(\mathrm{Ru}_{0.09}\mathrm{Co}_{0.91})_3\mathrm{O}_4$ oxide alloy forms highly non-uniform polycrystalline clusters on the surface of individual carbon fibers. Electrodes were made with loadings typically around 0.15 mg Ru cm^{-2}. Note that this loading corresponds to a cost of about \$1.11 kW^{-1} for precious metals on the chlorine electrode at a power density of 0.5 W cm^{-2} and a Ru price of \$3700 kg^{-1}. Comparing this cost to a Dept. of Energy cost target of \$250 kW^{-1} for a grid-scale storage system, it is apparent that catalyst costs on the chlorine side are negligible. A much more detailed description of the catalyst material and its properties is given in Chapter 3 of this work.

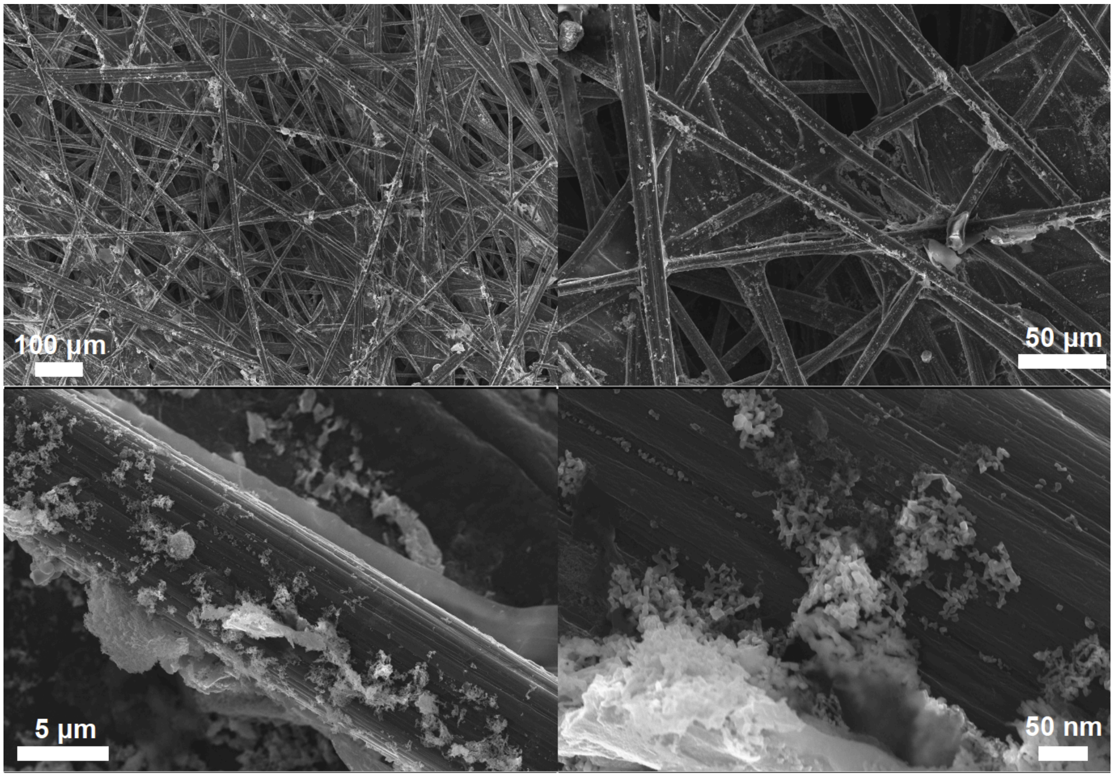

Figure 2.4. SEM micrographs of a ruthenium-cobalt oxide alloy electrode as deposited at four different levels of magnification. An $(\mathrm{Ru}_{0.09}\mathrm{Co}_{0.91})_3\mathrm{O}_4$ oxide alloy was deposited on a Toray carbon paper substrate, with a loading of 0.15 mg Ru cm^{-2}.

FOURTH-GENERATION CELL PERFORMANCE

The performance of the cell when operated in both the galvanic and electrolytic directions at 50 °C and 12 psig Cl_2 pressure is shown in Figure 2.5. The power density is also reported. Notice that the data are smooth as the cell moves from galvanic to electrolytic operation, indicating good reversibility for the reaction and acceptable membrane performance in both modes. The increasingly rapid drop in voltage with increasing galvanic current density is an indication that we are approaching the mass transport-limited current density, at which the rate of reactant ($Cl_2(aq)$) diffusion through the acid bubble wall limits the reaction rate (assuming that $H_2(g)$ transport is so fast as to never be the rate-limiting mass flux, which is common in the hydrogen-oxygen fuel cell community). In subsequently reported results, we show that increasing the chlorine gas pressure increases the limiting current density by raising the concentration of dissolved $Cl_2(aq)$. In contrast, in electrolytic mode, we do not encounter a mass transport limitation with increasing current density . In this case the reactant is Cl^-, which is present in relatively high concentrations.

In practice, there are two reasons why one would not want to operate at too high a voltage in electrolytic mode despite the absence of a mass-transport limitation. First, the electrolytic voltage efficiency of the cell $\left(\frac{E_{eq}}{E_{cell}}\right)$ drops with increasingly negative current densities. Second, the coulombic efficiency of the electrolytic reaction will decrease with increasing cell voltage due to the propensity to evolve O_2 at the chlorine electrode at higher voltages. Note that chlor-alkali cells generate 0.5-0.8 vol% O_2 in the product stream when operating around 0.4 A cm^{-2} [41], so coulombic efficiencies in this cell should remain above 98% over a large operational range.[iv]

[iv] Assuming that O_2 and Cl_2 are ideal gases, 0.5-0.8 vol% O_2 corresponds to 0.5-0.8 mol% O_2, which corresponds to a parasitic loss of 1.0-1.6%, because every mole of evolved O_2 gas releases four moles of electrons while every mole of evolved Cl_2 only releases two moles of electrons.

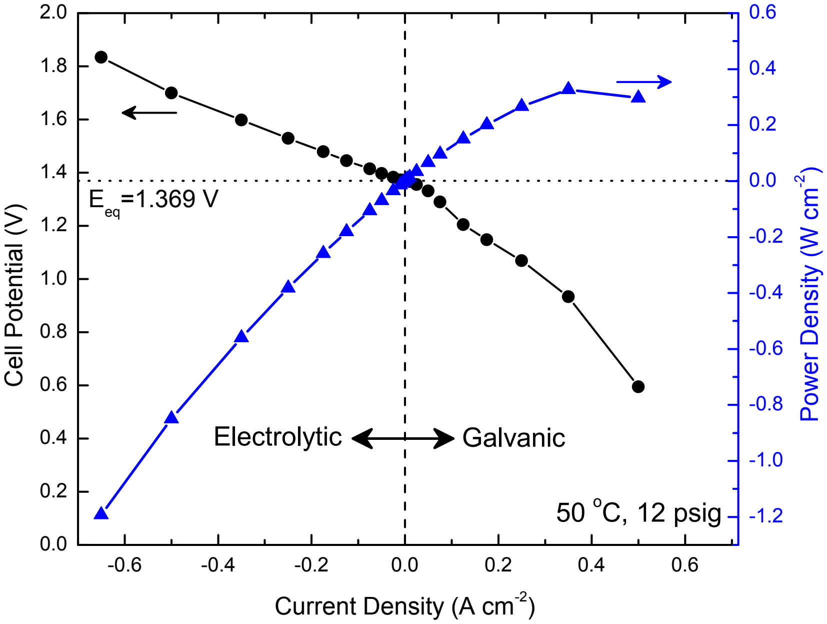

Figure 2.5. Potential vs. current density and power density vs. current density for the fourth-generation cell operated in both galvanic and electrolytic mode at 50 °C and a Cl_2 pressure of 12 psig. The cell equilibrium potential is denoted with a horizontal dotted line, and electrolytic and galvanic operation are separated by a vertical dashed line.

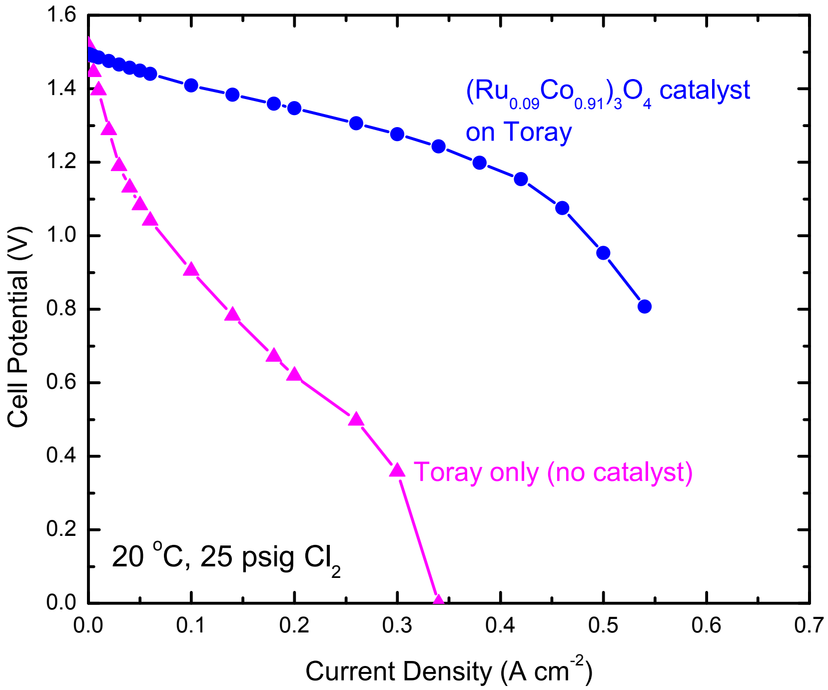

Figure 2.6. Cell potential vs. current density for a cell with no catalyst material on the Cl_2 electrode and a cell with the ruthenium-cobalt oxide alloy described previously. An ELAT®GDE was used on the hydrogen side in both experiments.

The importance of the chlorine electrocatalyst is illustrated in Figure 2.6. In the absence of the catalyst material, a large overpotential is observed, which is characterized by concave-upward curvature in the potential vs. current density data and is associated with sluggish charge-transfer kinetics at the chlorine electrode. In the presence of the catalyst, this overpotential is insignificant. The nonzero slope over the lower current densities in the catalyzed curve is primarily due to ohmic loss in the Nafion membrane, as will be shown later. The hydrogen-side catalyst is unchanged between the two cells: the hydrogen electrode overpotential is insignificant.

Cell performance in the galvanic direction was characterized over a wide range of operating conditions. Results in Figure 2.7 show the effect of changing the cell pressure. The difference is very pronounced: increasing the pressure from 12 psig to 70 psig results in a maximum power density increase from 0.41 W cm^{-2} to 1.01 W cm^{-2} (at 50 °C). Pressure has almost no effect on cell performance below current densities of 0.2 A cm^{-2}. This is due to the fact that the primary impact of increasing cell pressure is to drive more $Cl_2(g)$ into solution, thereby increasing its concentration and improving mass transport to the electrode-solution interface [10]. At low current densities, however, mass transport losses are insignificant, and therefore changes in cell pressure are inconsequential. Another noteworthy feature of the potential vs. current density plots in Figure 2.7 is the absence of a significant activation loss associated with the electrode charge-transfer kinetics, i.e. the current-potential curves are nearly linear at low overpotentials. Small differences in the cell equilibrium potential can be attributed to both differences in temperature and in the activity of Cl_2 as a function of pressure, in accordance with the Nernst equation. The effects of temperature are more modest, but this is likely due to the limited range in which temperature can be varied (Nafion cannot function as a conductor below 0 °C or above about 80 °C, and the test apparatus used in our lab restricts this range even further).

Another important characteristic of an H_2-Cl_2 cell is the performance dependence on acid concentration. Acid concentration affects a number of processes occurring in the cell. First, the PEM conductivity is a function of acid concentration. This conductivity should peak at about 2.3 M HCl [30]. Our results, however, indicate that the PEM conductivity in this cell is only a weak function of acid concentration: this is apparent by the approximately equal slopes of the three lines in Figure 2.8. One potential explanation for this observation is that, because HCl is being generated at the electrode-membrane interface when the cell is operated in galvanic mode, the membrane is exposed to an effective acid concentration much higher than the bulk acid

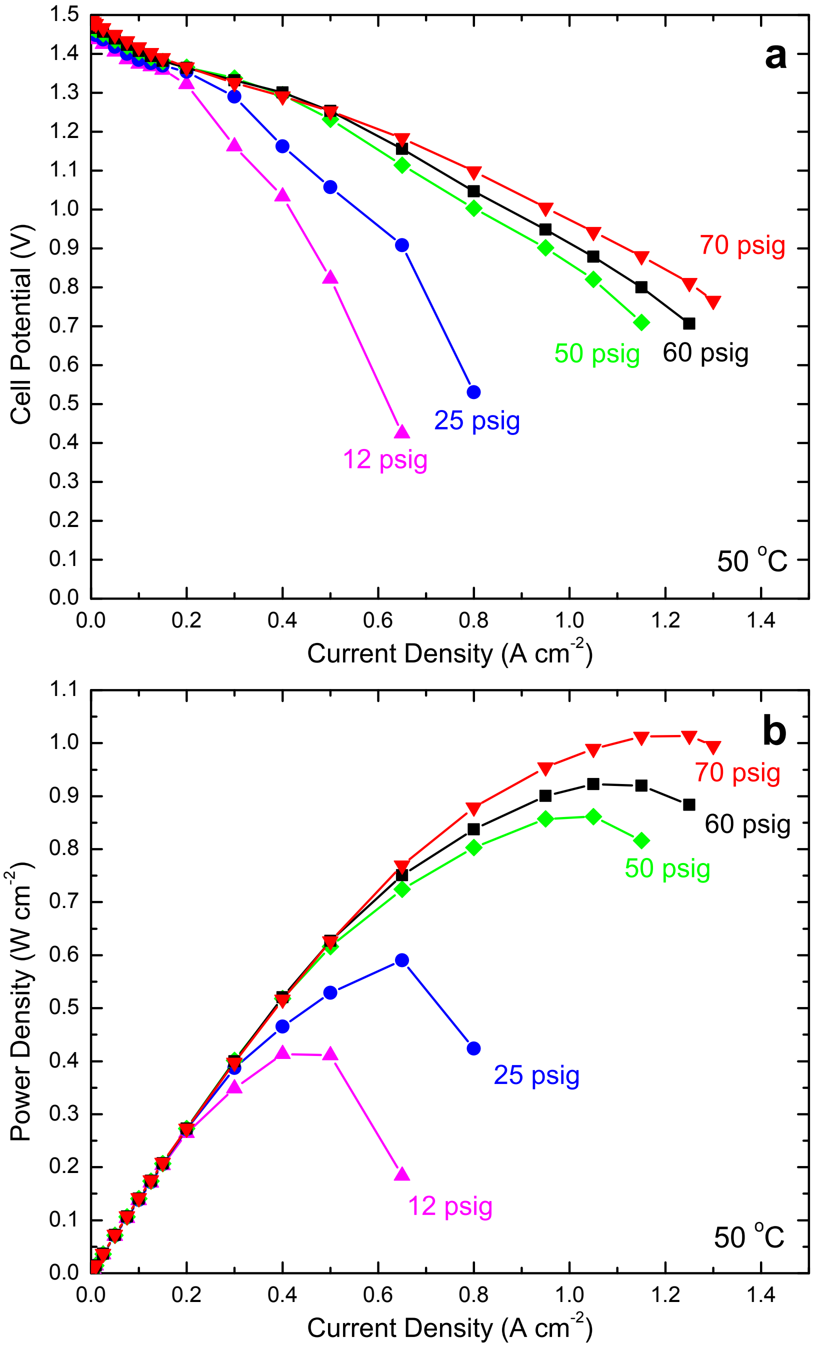

Figure 2.7. (**a**) Cell potential vs current density, and (**b**) power density vs. current density for five different cell pressures. Data were collected at 50 °C, and the hydrogen electrode was humidified.

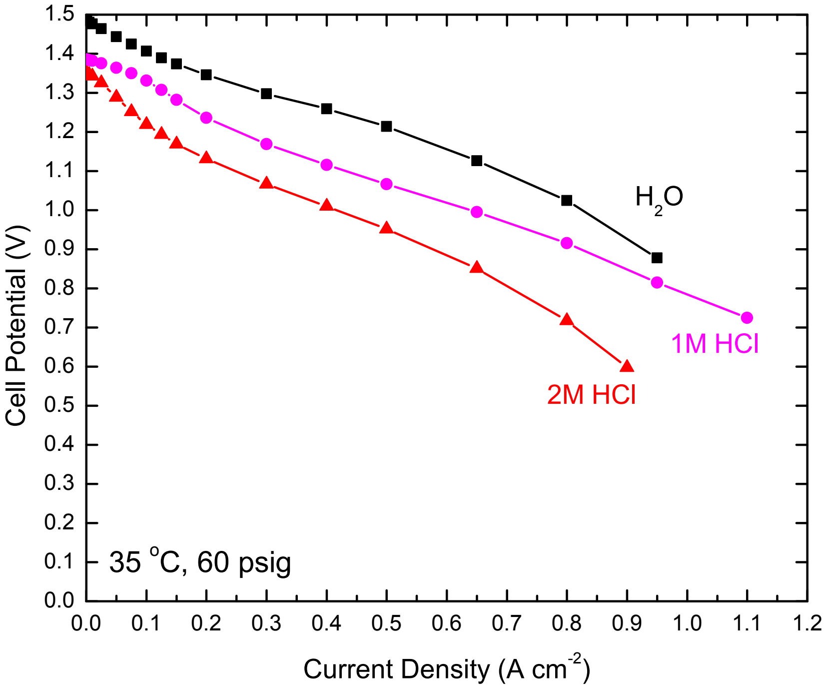

Figure 2.8. Cell potential vs. current density showing the effects of acid molarity on performance. The initial electrolyte concentration is indicated in the figure. "H_2O" refers to an initial electrolyte of pure water.

concentration, regardless of the value of the bulk concentration. Note also that the equilibrium potentials seen in Figure 2.8 vary with the acid molarity, as expected from the Nernst equation.

Hydrogen electrode humidification appears to improve cell performance, as can be seen in Figure 2.9. Increases in the maximum power density and the limiting current density of the cell were observed over the entire range of Cl_2 pressures explored. This is likely due to membrane dehydration becoming more of an issue at high current densities. Since the membrane conductivity is a strong function of its level of hydration, drying out the membrane has the effect of increasing resistive losses through the cell. Because there are two primary fluxes governing the

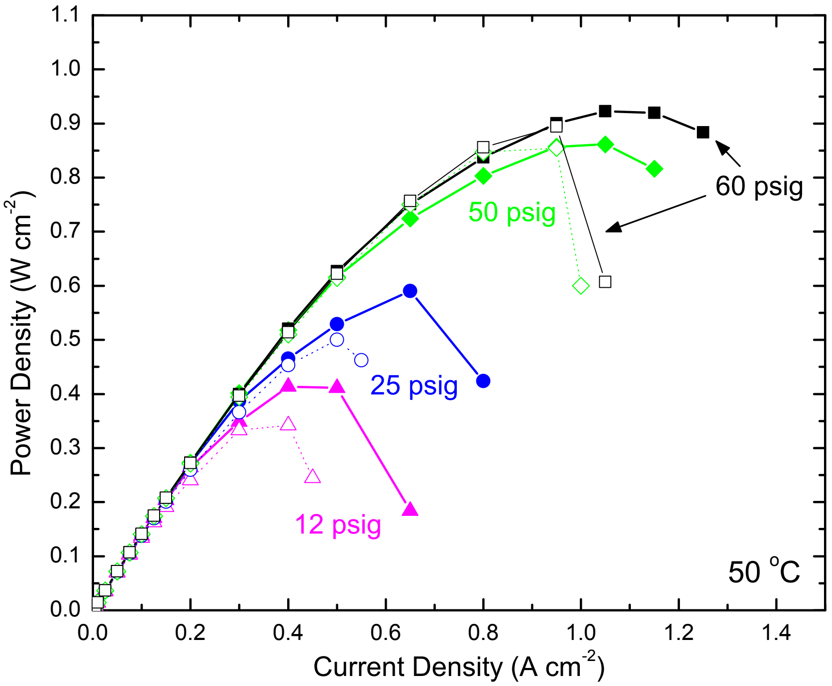

Figure 2.9. Effect of H_2-side humidification on cell performance. Dry anode data are shown with hollow markers and dashed lines at each of the pressures studied. Humidified anode data are shown with solid markers and solid lines.

water content of the membrane – a current-independent diffusive flux from the Cl_2 side (which is wet and therefore has a high H_2O activity) to the H_2 side and, in galvanic mode, a current-dependent electro-osmotic flux from the H_2 side to the Cl_2 side – at high current densities the electro-osmotic flux may become sufficiently large to dehydrate the membrane. In humidifying the H_2 electrode, this problem can be alleviated by delivering more water to the membrane via the H_2 gas stream. This likely explains the benefits seen from H_2 electrode humidification in Figure 2.9.

FOURTH-GENERATION CELL EFFICIENCY CHARACTERISTICS

Because chlorine ($Cl_2(aq)$) crossover through Nafion is known to be minimal [30] and we restrict our cell potential to a range in which oxygen evolution is slow [41], we expect the coulombic efficiency of this cell to be near 100% and therefore the energy conversion efficiency to be nearly indistinguishable from the voltage efficiency (see the discussion of measures of efficiency in the methods section). In Figure 2.10 we show the voltage efficiency as a function of power density for five different Cl_2 pressures. This format is particularly useful because it illustrates the tradeoff, as one varies the operating conditions, between the two most important figures of merit of the cell. Note that a power density of approximately 0.4 W cm^{-2} is reached at 90% efficiency for all pressures exceeding about 25 psig – the minimum pressure so that $Cl_2(aq)$ solubility does not cause a significant mass transport limitation for this particular cell. Second, a peak power density exceeding 1 W cm^{-2} was achieved at an efficiency around 56% for 70 psig. A separate experiment reached a peak power density of 1.15 W cm^{-2}, but this was not part of a series so it does not appear in the figures. Another important note is that at high efficiencies, i.e. at low current densities, the power density at 90% voltage efficiency in galvanic mode is nearly equal to the power density at 90% voltage efficiency in electrolytic mode (this is true due to the linear nature of the power density curve near equilibrium; see Figure 2.5). Thus, operating this cell at a power density of 0.4 W cm^{-2} equates to a round-trip efficiency of 81%.

COMPARISONS OF FOURTH-GENERATION PERFORMANCE TO AN H_2-CL_2 MODEL

Comparing the experimental results to the hydrogen-chlorine fuel cell model of Rugolo *et al.* [10] provides valuable insight into the behavior of the system and indicates directions for, and ultimate

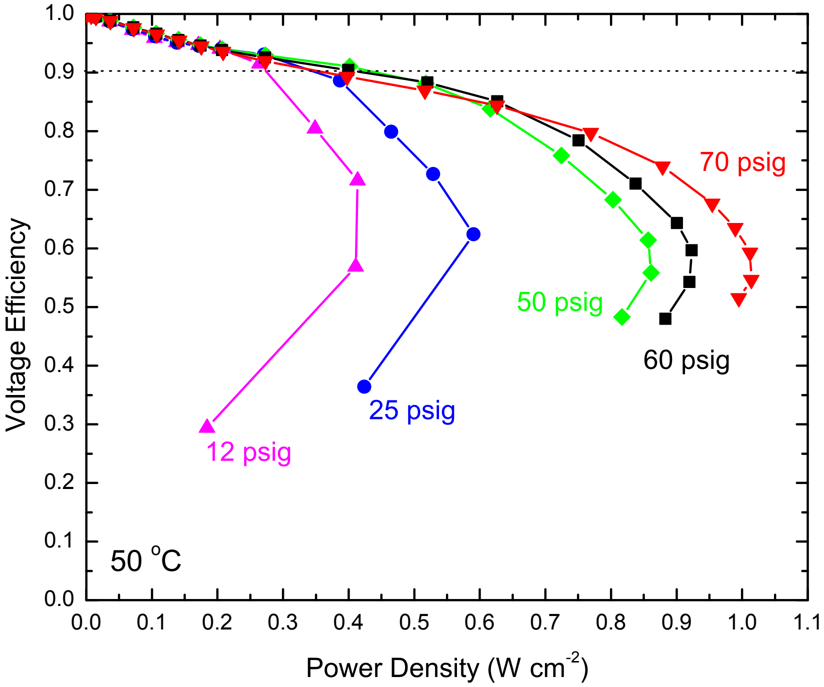

Figure 2.10. One-way galvanic efficiency vs. power density for five different Cl_2 pressures at 50 °C with H_2 side humidification. The horizontal dotted line indicates 90% efficiency.

limitations to, further improvement in the performance of a cell of this design.

The model accounts for voltage losses due to electrocatalytic activation at both electrodes, ohmic loss in the PEM, and $Cl_2(aq)$ mass transport through the chlorine gas bubble wall to the chlorine electrode. It predicts the voltage vs. current density behavior as one varies the following *Engineering Parameters* (EPs): PEM thickness, cell pressure, bubble wall thickness, and exchange current densities at both electrodes; and the following *Operating Parameters* (OPs): temperature and acid concentration.

We fit the model to our data using known values of all of these parameters[v] but three, which were treated as adjustable parameters. (1) The chlorine exchange current density, i_0^{Cl}, was chosen to be 175 mA cm^{-2} in order to fit the data. (2) A series resistance (denoted $R_{stack}A$) [vi], absent from the original model, accounting for ohmic losses through the current collectors, endplates, and all of the electrical connections to the DC electronic load and/or power supply. The best-fit value was 0.125 ohm-cm^2. (3) The diffusion layer thickness (denoted ε), which represents the critical mass transport parameter in the model, was chosen to be 5.85 μm in order to best fit the limiting current density seen in the 70 psig case, and then this same value was used for all of the other pressures. This is why the model appears to more accurately match the cell's maximum power density in the 70 psig case than in the 12 psig case in Figure 2.11. Because the model utilizes a simple form of Henry's law to obtain the concentration of $Cl_2(aq)$ in solution as a function of $Cl_2(g)$ pressure, the limiting current density should be directly proportional to the absolute pressure of gas in the system. However, in Figure 2.7 one can see that the limiting current density for the 12 psig case is approximately 0.65 A cm^{-2}, whereas the limiting current density for

---

[v] The value for the hydrogen electrode exchange current density, i_0^H, was held at 250 mA cm^{-2}, consistent with results in work by Neyerlin *et al.* [29]. We control directly the other known, non-adjustable parameters.

[vi] For dimensional consistency, the value of this resistance must be multiplied by the cell area.

the 70 psig case is about 1.25 A cm^{-2}. The model predicts, based on the absolute pressure ratio, that these values should span a range of a factor of 3.2 (based on converting 70 psi and 12 psi to absolute pressures, rather than gauge, and then looking at their ratio), whereas we find a range of less than a factor of two experimentally. Clarifying the reasons for this behavior will require further refinement of the model of mass transport behavior of this kind of system. Note that the model was developed with a simplified mass transport picture in mind, so it is unsurprising that the fit is least accurate in the regime where mass transport losses dominate (i.e. at high current densities).

We show the overall fit of the model to the data in Figure 2.11. Also shown for comparison are results from the“Base case” and “More Optimal case” modeled by Rugolo *et al.* [10]. The latter is their prediction of the performance that may reasonably be expected with further research and development on a cell of this design. Table 2.1 directly compares parameter values of the “Base case” and the “More Optimal case” of Rugolo *et al.*, and of the model fit to our experimental data. The variable ”L” refers to the Nafion membrane thickness and ”P_{gauge}” refers to the chlorine gas pressure. The experimental performance is well beyond that of the “Base case”, and based on these results we anticipate that further R&D could raise the power density at 90% galvanic efficiency by a factor of three to four.

FIFTH-GENERATION CELL PERFORMANCE

Building on the successful development of our fourth-generation cell, we implemented a number of important practical changes to improve cell performance, all of which were aimed at improving mass transport and reducing ohmic losses. The changes included the following: (1) the flow fields

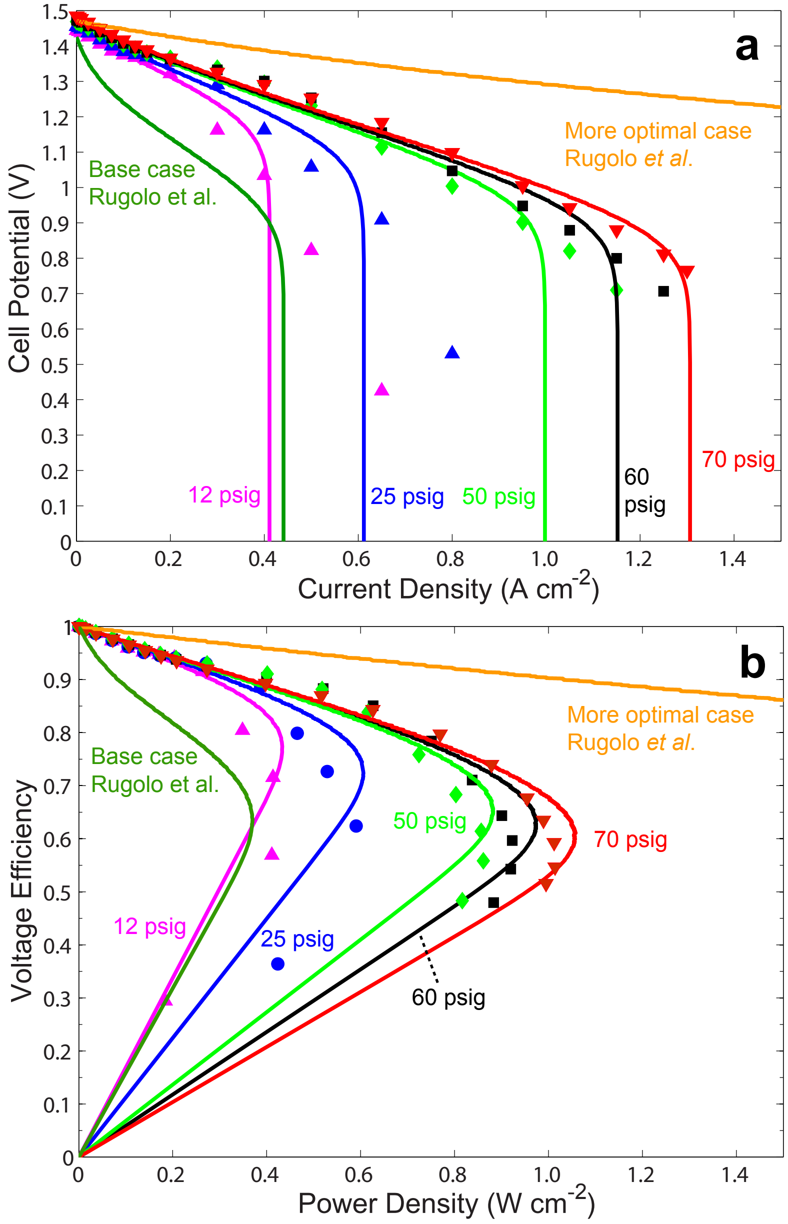

Figure 2.11. Comparison of model to experiment. Experimental data are indicated with symbols and model fits are shown using lines of corresponding color. (**a**) Cell potential vs. current density and (**b**) Voltage efficiency vs. power density. Also indicated are the "Base case" and "More Optimal case" scenarios described by Rugolo *et al.* [10].

Table 2.1. Parameters used in the "Base case", the "More Optimal case", and in fitting the model to the experimental data. Adjustable parameters are denoted in red italics.

	Base	**Fit**	**More Optimal**
i_0^{Cl} / **mA cm^{-2}**	10	*175*	250
i_0^{H} / **mA cm^{-2}**	250	250	600
ε / **μm**	3	*5.85*	1
L / μm	150	50	25
P_{gauge} / atm	1	1.8-5.8	5
$R_{stack}A$ / ohm-cm^2	0	*0.125*	0
Power at 90% Efficiency / W cm^{-2}	0.1	0.285-0.358	1.2

were switched from a serpentine design to an interdigitated design, leading to vastly improved mass transport behavior due to the forced convection this design induces, (2) electrodes were stacked 6x on the chlorine side of the cell, leading to a thicker electrode, greater surface area, and a larger flow path, (3) Nafion 211 (25 μm thick) was used instead of Nafion 212, leading to reduced ohmic losses, and (4) flow into the cell consisted of a single-phase liquid flow of HCl saturated with Cl_2 gas, as opposed to the two-phase flow used in the fourth-generation cell. As can be seen in Figures 2.12-2.14, cell performance was markedly improved with these changes. Limiting current densities reached 2.9 A cm^{-2} in the galvanic direction and exceeded 1.5 A cm^{-2} in the electrolytic direction for the 70 psig case (Figure 2.12), greatly exceeding performance observed in the fourth-generation cell, where galvanic limiting current densities were about 1.3 A cm^{-2}.

Looking at the dependence of the cell performance on Cl_2 gas pressure, drastic performance gains were seen by increasing the pressure to > 50 psig, as can be seen in Figure 2.13. Note that these plots likely underestimate the performance at low pressures, though[vii], as measurements are

---

[vii] As the limiting current density is approached, the potential begins bouncing around, likely due to the pulsating nature of the flow. This bouncing is much more severe in the low-pressure regime, thus complicating measurements and leading to conservative, underestimated limiting current densities.

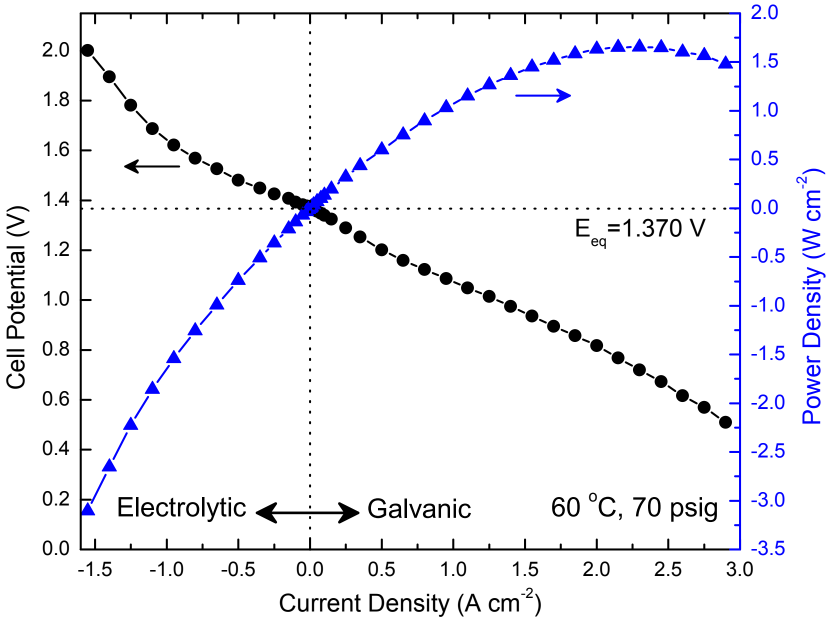

Figure 2.12. Potential vs. current density and power density vs. current density for the fifth-generation cell operated in both galvanic and electrolytic mode at 60 °C and a Cl_2 pressure of 70 psig. The cell equilibrium potential is denoted with a horizontal dotted line, and electrolytic and galvanic operation are separated by a vertical dashed line.

more difficult under those conditions. At 12 psig, a power density exceeding 0.6 W cm^{-2} was achieved. This increased to 0.8 W cm^{-2} in the 25 psig case, 1.45 W cm^{-2} in the 50 psig case, and 1.65 W cm^{-2} in the 70 psig case. To our knowledge, these results represent the best performance ever observed in a halogen-based flow cell (1.5 W cm^{-2} was achieved in a hydrogen-bromine device from Livshits *et al.* [23]).

Lastly, Figure 2.14 shows the cell's one-way galvanic efficiency vs. power density. The differences between the 12 psig case and the 70 psig case are much less pronounced at 90% efficiency than the differences at lower efficiencies/higher power densities, as can be seen in the figure. A power density exceeding 0.3 W cm^{-2} at 90% efficiency was achieved in the 12 psig case, with that number increasing to about 0.5 W cm^{-2} in the 70 psig case. For comparison, the 12 psig number is 0.3 W cm^{-2} at 90% efficiency in the fourth-generation cell (Figure 2.10), performing almost identically to the fifth-generation cell, while the 70 psig number in the fourth-generation cell is 0.4 W cm^{-2}, slightly underperforming the newer cell.

2.3 CONCLUSIONS

We have developed a high-performance hydrogen-chlorine regenerative fuel cell that incorporates a $(Ru_{0.09}Co_{0.91})_3O_4$ alloy as a chlorine redox electrocatalyst, which is the subject of the following chapter. We described two different cells: a fourth-generation design utilizing a serpentine flow field and two-phase flow and a fifth-generation design utilizing an interdigitated flow field and single-phase flow. In both cells, we observed no significant activation losses, even with chlorine electrode precious metal loadings as low as 0.15 mg Ru cm^{-2}. In the fourth-generation cell, the peak galvanic power density exceeded 1 W cm^{-2}, which is twice that of previous work with much

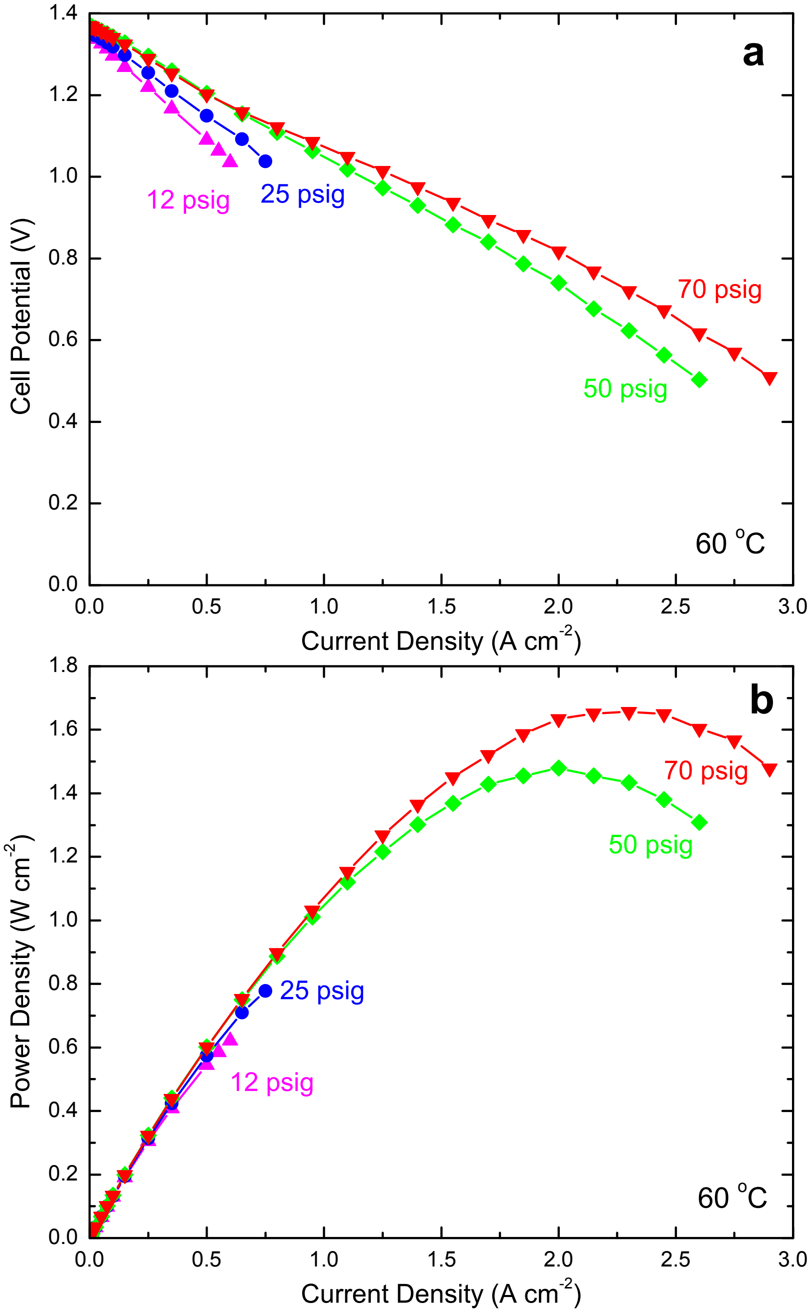

Figure 2.13. (**a**) Cell potential vs current density, and (**b**) power density vs. current density at four different cell pressures. Data were collected at 60 °C, and the hydrogen electrode was humidified.

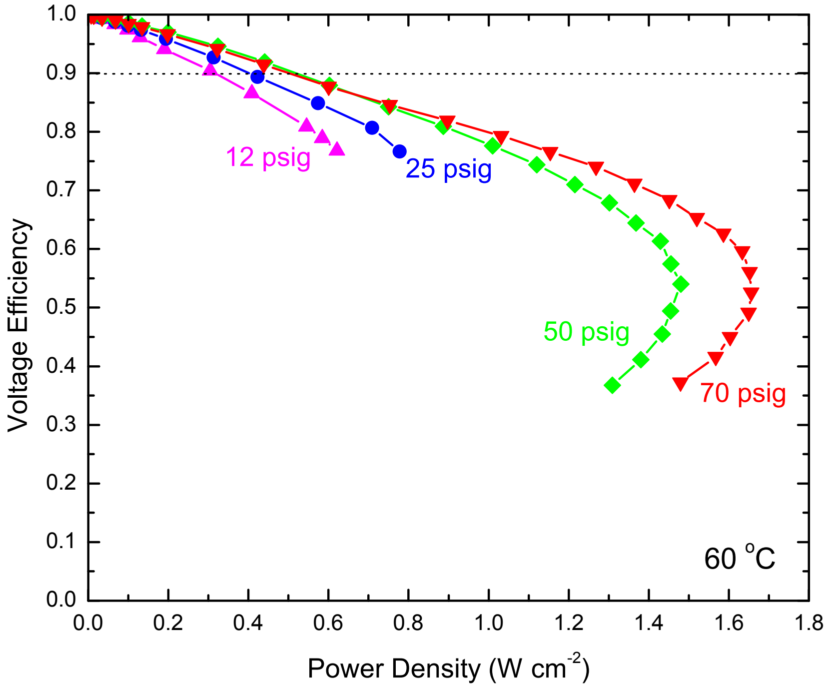

Figure 2.14. One-way galvanic efficiency vs. power density for four different Cl_2 pressures at 60 °C with H_2 side humidification. The horizontal dotted line indicates 90% efficiency.

higher precious metal loadings on the Cl_2 electrode. A power density of nearly 0.4 W cm^{-2} was obtained at 90% voltage efficiency, which is an important figure of merit when considering these devices for grid-scale electrical energy storage. The effects of Cl_2 gas pressure, electrolyte acid concentration, and hydrogen electrode humidification were reported. We also compared the fourth-generation cell results to the H_2-Cl_2 fuel cell model of Rugolo *et al.*, to which we added a series resistance term to better fit the experimental results seen here. The experimental performance is well beyond that of the "Base case" in the model, and the comparison to the model indicates the R&D directions needed for another factor of 3-4 improvement in power density in order to reach the envisioned "More Optimal" case. Performance was improved even further in the fifth-generation cell, with a maximum galvanic power density of 1.65 W cm^{-2} and a limiting current density of 2.9 A cm^{-2} in the 70 psig case. A power density exceeding 0.5 W cm^{-2} was obtained at 90% voltage efficiency. These results are not directly compared to the model of Rugolo *et al.* due to the fact that single-phase liquid flow was used in the fifth-generation cell, while the mass transport behavior of the model is based on a two-phase flow like that used in the fourth-generation cell.

Based on the high power densities and high efficiencies demonstrated here, we anticipate that a device such as this could be used in a flow battery configuration as a grid-scale electrical energy storage device. Further studies, including durability assessments and system-level integration, are necessary to determine its economic feasibility in this context. In the longer term, the device may become a component of a carbon sequestration scheme that mimics the natural chemical weathering process for CO_2 removal from the atmosphere.

3

Ruthenium-Based Oxide Alloys as Chlorine Redox Catalysts

ALONG WITH THE SUCCESSFUL DEVELOPMENT of high-performance hydrogen-chlorine regenerative fuel cells, which are based on the use of an $(Ru_{0.09}Co_{0.91})_3O_4$ oxide alloy catalyst on the chlorine electrode, we began experiments to try and understand the performance of this particular material and to search for other materials capable of performing comparably. This search was motivated by one simple goal: find a relatively inexpensive, stable material capable of effectively catalyzing both the chlorine evolution reaction (CER) and chlorine reduction reaction (CRR). The CER and CRR together form an important electrochemical redox couple, which takes the following form:

$$Cl_2 + 2e^- \rightleftharpoons 2Cl^- \tag{3.1}$$

where the right arrow indicates the CRR and the reverse direction is the CER. The CER is critical to the industrial production of Cl_2, the CRR is important to the operation of an H_2-Cl_2 fuel cell, and both reactions are important for the operation of a regenerative fuel cell or flow battery. The kinetics for this redox reaction are generally facile, especially when compared to oxygen reduction and evolution kinetics. RuO_2 and RuO_2-based materials are known to be excellent catalysts for the chlorine redox reaction, particularly oxide alloys composed of RuO_2 and another transition metal oxide. Alloys of RuO_2 with TiO_2 have been used for decades in the chlor-alkali industry as effective chloride oxidation catalysts in the chlorine evolution reaction [34, 42–44]. The TiO_2 imparts stability while the RuO_2 imparts excellent catalytic activity and electronic conductivity. Minimizing the amount of RuO_2 is beneficial from a cost perspective (see Table 3.1) and a stability perspective, but it inevitably leads to decreased electrode performance due to reduced activity and conductivity. Thus, typical RuO_2/TiO_2-based electrodes are about 30 mol% RuO_2, a sort of "optimum" concentration when considering the tradeoffs just mentioned [43, 45, 46].

While the majority of experimental work has been devoted to exploring the effectiveness of CER catalysts, some researchers have focused on catalysts related to the CRR. This reaction is critical to the function of an H_2-Cl_2 based fuel cell and any sort of chlorine-based flow battery where the ability to both oxidize chloride anions and reduce chlorine molecules in a reversible fashion is necessary. H_2-Cl_2 fuel cells, which generate hydrochloric acid and electricity as products, could be used in a variety of applications, such as space [33] and defense [32] (where high power and energy densities are critical). Thomassen *et al.* studied these cells extensively [21, 28] and also focused on effective catalysts for the CRR. In particular, platinum and ruthenium and the effects of oxide coverage were studied, noting that the catalytic activity can be particularly sensitive to the presence of an oxide film [26]. Other studies have shown that the catalytic activity can be very sensitive to preparation technique, as using metal nitrate precursors instead of metal chloride ones yields materials with different catalytic activities, likely due to the propensity of chloride ions to replace oxide ions on sublattice sites [43]. A study on oriented single-crystal RuO_2 electrodes concluded that the CER reaction rate was the same on $RuO_2(110)$ and $RuO_2(101)$ surfaces, while the CRR was significantly faster on the (110) surface under certain conditions [47]. Because of these considerations, it is important to understand that it is extremely difficult to generalize results from a given set of experiments, as small changes in the synthesis procedure can lead to significant differences in results. This is true for the experimental study of catalysis in general, which is why it has proven to be a particularly difficult field to understand.[i]

Much effort has been devoted to the potential use of regenerative H_2-Cl_2 cells as grid-scale storage devices, starting in the 1970s [17, 20, 22, 31], with more recent work from our group [10, 11, 39]. Of particular note, a previous publication from our group (and the previous chapter in this dissertation) utilized one of the catalysts being studied here: a ruthenium-cobalt oxide

---

[i] Nobel prizes are routinely awarded for groundbreaking work on catalysis (three in the last decade by my count), reinforcing the point that there is still a lot to understand about the huge and diverse field of catalysis.

alloy of composition $(Ru_{0.09}Co_{0.91})_3O_4$ was deposited on a Toray carbon paper and used as a positive electrode. Virtually no activation losses were observed, and power densities exceeding 1 W cm^{-2} were achieved [11]. The previous chapter details the development of this cell and the justification behind the use of this electrode material.

There is an extensive literature on mixed oxide alloys as catalyst materials (particularly Ru-Ti alloys), as well as on pure RuO_2 [37, 38, 45, 48–53]. Most studies examine these types of materials in the context of the oxygen evolution reaction (OER), but many look at the CER as well. There are very few studies on these materials as CRR catalysts. One of the most well studied types of materials are cobalt-based catalysts, which have been examined for applications in both the OER and the CER [35, 54–59]. Da Silva *et al.* systematically varied Ru content in cobalt oxide and determined these alloys had properties similar to Ru-Ti alloys, specifically mentioning the relatively high surface areas seen in both of these electrode materials [56]. Furthermore, the presence of the RuO_2 appears to have a stabilizing effect on the cobalt oxide, which in its pure form is susceptible to dissolution in acidic media [57]. Da Silva *et al.* also showed that alloys of RuO_2 and Co_3O_4 tend to have much higher electrochemicallly active surface areas than the pure oxides, suggesting that this is the root of their improved catalytic performance [56]. Furthermore, they conclude that having as little as 10 mol% RuO_2 is enough to completely determine the catalytic behavior of the system and lead to oxide stabilization in acid, attributing these effects to surface enrichment of RuO_2. Makarova *et al.* prepared rutile electrodes of nominal composition $Ru_{0.8}Co_{0.2}O_{2\text{-}x}$ and determined that the particle size can affect chemical composition: smaller particles compensate for Co doping by becoming oxygen deficient, while larger particles express a higher valency of Ru [58]. Burke *et al.* found that maximum OER performance occurred for 10-20 mol% RuO_2 in Co_3O_4 [54]. Interestingly, this is the

Table 3.1. Prices of various metals of interest, in USD kg^{-1}. Both the lowest and highest prices of the past five years are indicated for each metal.

	Pt	**Ru**	**Co**	**Ni**	**Sn**	**Ti**	**Mn**
Price ($\$ kg^{-1}$)	27,300-58,800	1,800-7,800	30-86	15-23	13-36	10-16	0.005-0.015
Source	[69]	[69]	[70]	[71]	[72]	[73]	[74]

approximate range where we observe maximum performance for Ru-Co oxide alloys in this work.

Manganese-based catalysts have been shown to be effective OER catalysts (MnO_2) [60, 61], but studies in the context of the CER are limited at best, with some work done at General Electric on alloys of Ru-Mn at compositions of up to 25 mol% Mn [62]. Nickel-based oxides were studied for both OER and CER by Macounová et al [63]. They prepared oxides of various compositions using a sol-gel method and tested them for both OER and CER activity. They determined that addition of 10 mol% Ni to RuO_2 maximized the activity of the materials towards the CER relative to pure RuO_2. Finally, tin-based catalysts have been studied in a variety of settings as well [64–67]. Ru-Sn oxide alloys (along with Ir, Ta, and Pt oxides) were examined by Comninellis *et al.*, who noted that yields for SnO_2 could be quite low due to the relatively high vapor pressure of the Sn precursors [66]. They also noted that lifetime performance was maximized for a 30 mol% Ru / 70 mol% Sn oxide alloy, and they speculate that the oxide formed may be $RuSn_2O_6$ as opposed to $(RuSn)O_2$. SnO_2 can also be used as an additive in industrial electrodes in order to enhance their selectivity for the CER with respect to the OER [67] and for stability purposes [68].

In light of all of this previous work, the goal of this chapter is to compare the catalytic activity of a variety of RuO_2-based oxide alloys towards both the CER and CRR. In particular, alloys consisting of Ru with Co, Ni, Mn, Cu, Sn, and Ti were prepared and their relative performance was compared. Ruthenium-cobalt (Ru-Co) oxide alloys were found to be the best performers.

Alloys with Ru concentrations less than 50% but greater than 5% were found to exhibit the best catalytic performance. When the Ru concentration is $> 50\%$, the oxide forms an unclear crystal structure. When the Ru concentration drops below 50%, the alloy preferentially adopts the spinel structure of Co_3O_4, and an increase in catalytic performance is seen. When the Ru concentration is too low ($< 5\%$), the activity drops off significantly, likely due to a combination of resistive and catalytic effects.

3.1 Experimental Methods

Electrode synthesis

Small niobium tabs were used as an electrode substrate (Figure 3.1). Prior to deposition of the catalyst layer, the tabs were pretreated in the following way: (1) brief sandblasting, (2) sonication for 10 min. in 70% isopropyl alcohol, (3) submersion in a hot (80 °C) 50% sulfuric acid (reagent grade, Sigma Aldrich) solution for 30 min., and (4) submersion in hot (80 °C) 6 M hydrochloric acid (ACS reagent grade, Sigma Aldrich) for 30 min. The individual substrates were thoroughly rinsed with DI-H_2O (18.2 MΩ ultrapure, Millipore) between steps and at the end. They were then dried and weighed.

Catalyst solutions were made using a variety of metal solutions and/or precursors: ruthenium (III) chloride hydrate (Alfa Aesar), cobalt (II) chloride (anhydrous, Alfa Aesar), copper (II) chloride (anhydrous, Aldrich), nickel (II) chloride hexahydrate (Sigma Aldrich), manganese (II) chloride tetrahydrate (Alfa Aesar), tin (II) chloride (anhydrous, Alfa Aesar), and titanium butoxide (Aldrich). To prepare the catalyst solution, the Ru precursor and one of the other metal precursors were added to a predetermined amount of concentrated HCl in the appropriate

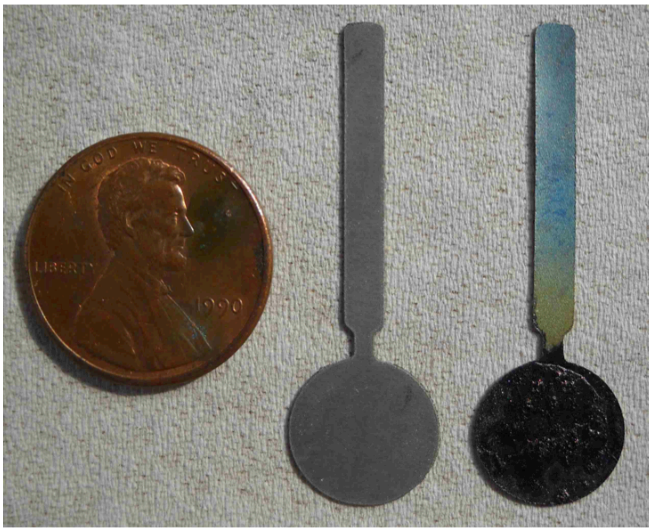

Figure 3.1. Image of both an RuO_2-coated and uncoated niobium tab electrode. A U.S. penny is also shown for scale.

amounts to give the desired molar ratio of the two metals (i.e. 1:1, 1:5, 1:10, etc.). The total concentration of dissolved metals was kept near 1 M for all solutions.

A small amount of the catalyst solution (20 μL) was then pipetted onto the circular portion of the niobium tab and evenly spread around. The tabs would be dried in an oven held near 90 °C for approximately 15 minutes to evaporate the HCl. The tabs were then moved to a furnace that was heated to 350 °C (45 minute ramp to 350 °C with a 60 minute hold at that temperature, followed by a 15 minute cool down). The tabs were then weighed to determine the amount of deposited catalyst material. The coating process was usually repeated three times to ensure an even coating of catalyst material. Note that only a weak dependence was seen between the electrode performance and the number of coats.

ELECTRODE CHARACTERIZATION

Electrochemical characterization was done using a BASI EC Epsilon potentiostat and a three-electrode cell. The working electrode was the niobium tab with deposited catalyst material (described above), the counter electrode was a large platinum foil, the reference electrode was Ag/AgCl (+0.210 V vs. SHE), and the electrolyte was 1 M HCl saturated with $Cl_2(aq)$. Linear sweep voltammetry was done on each electrode, with a scan rate of 10 mV s^{-1}. The equilibrium potential would first be measured, and then the potentiostat was swept from n mV in the negative (reduction) voltage direction to n mV in the positive (oxidative) direction, where n was either a 150 mV or a 200 mV deviation from equilibrium. Measurements were done a minimum of three times to ensure reproducibility among the individual sweeps, and the results were averaged. Overpotentials were calculated by finding the point where the average current density was nearest zero and then using that point as the zero overpotential point. This has the effect of subtracting out any current that arises due to the capacitance of the electrode.

Micrographs of the electrodes were obtained using a scanning electron microscope (SEM, Ultra55, Zeiss). X-ray diffraction was done by depositing the various oxide alloy materials used to form the electrode onto an amorphous substrate (glass microscope slides, VWR). θ-2θ scans were done from $2\theta = 10^\circ$ to 80° using a Bruker D8 Discover diffractometer. Copper K_α radiation was used. Lattice parameters were calculated using methods from Cullity [75].

3.2 RESULTS AND DISCUSSION

A comparison of the half-cell behavior of a variety of metals, all at a 1:5 molar ratio of ruthenium to the metal, is shown in Figure 3.4. Pure RuO_2 is also shown as a reference, and it slightly outperforms all the alloys at large overpotentials (both positive and negative). At high overpotentials, however, mass transport effects will be most pronounced, meaning the effects of surface morphology will be enhanced. At low overpotentials, or near equilibrium, mass transport effects are minimized, and the innate catalytic activity is more prominent. The inset in Figure 3.4 shows the same curves zoomed in near the origin. Here, the slope of the lines is a good indicator of relative catalytic activity: the higher the absolute value of the slope, the higher the catalytic activity (i.e. larger exchange current density). This fact can be deduced from looking at the Butler-Volmer equation:

$$i = i_0 \left[\exp\left(\frac{-\alpha n F \eta}{RT} \right) - \exp\left(\frac{(1-\alpha) n F \eta}{RT} \right) \right] \tag{3.2}$$

where i_0 is the exchange current density of the working electrode (in mA cm^{-2}), α is the transfer coefficient, n is the number of electrons involved in the rate-determining step of the reaction (n=1 is assumed here), F is Faraday's constant (96485 C mol^{-1}), η is the overpotential in V, R is the gas constant (8.314 J mol^{-1} K^{-1}), and T is the temperature (in K). For small x, one can make the following approximation:

$$e^x \approx 1 + x \tag{3.3}$$

which, when applied to Equation 3.2, simplifies this equation to the following form:

$$i = -i_0 \frac{nF}{RT} \eta. \tag{3.4}$$

Now, a plot of current density vs. overpotential (at low overpotentials) should yield a straight line with slope $-i_0 \frac{nF}{RT}$.[ii] From this, i_0 can be calculated. This number provides the simplest direct comparison of the catalytic performance of the various oxide alloys presented here. A list of the calculated i_0 values for the materials presented in this chapter is shown in Table 3.2. Note how the Ru-Co and Ru-Ni alloys are generally the best performers over the entire concentration range.

It is important to note that the exchange current densities calculated here are based on the geometric surface areas of the electrodes, not the true surface areas, so these numbers do not control for differences in surface areas between the different oxide materials. These surface areas may vary substantially, too, as is evident in the micrographs seen in Figures 3.2 and 3.3. In Figure 3.2, the "mudcracked" morphology typical of DSAs is evident, and it is clear that these oxide alloys tend to form as highly polycrystalline materials with very rough surfaces. Based on the measured i_0 of this as-deposited RuO_2 (4.36 mA cm^{-2}), and comparing it to a literature value for smooth RuO_2 (0.01 mA cm^{-2} [26]), we can estimate a surface area enhancement factor of approximately 400 for the pure RuO_2 electrode. These numbers are likely comparable for the other electrode materials.

From the inset of Figure 3.4, it is clear that the ruthenium-cobalt alloy is the best performer, but note that all of the other alloys are capable of performing reasonably well compared to the pure RuO_2 electrode. It is interesting that the Ru:Ti 1:5 alloy appears to be the worst performer, yet this is the material of choice (albeit at a different molar ratio and under different electrolyte conditions) for industrial chlorine production. This highlights the important fact that durability is often a more important concern than catalytic activity.

[ii] The negative reciprocal of this slope, $\frac{RT}{nFi_0}$, is the commonly-referenced parameter known as the charge transfer resistance (R_{ct}), which can be a good indicator of catalytic performance.

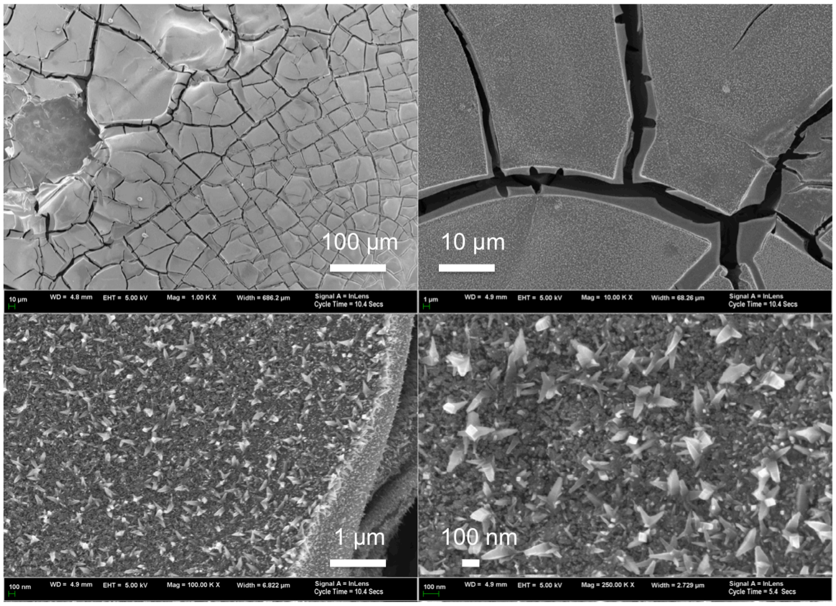

Figure 3.2. Micrographs of an as-deposited RuO_2 electrode tab.

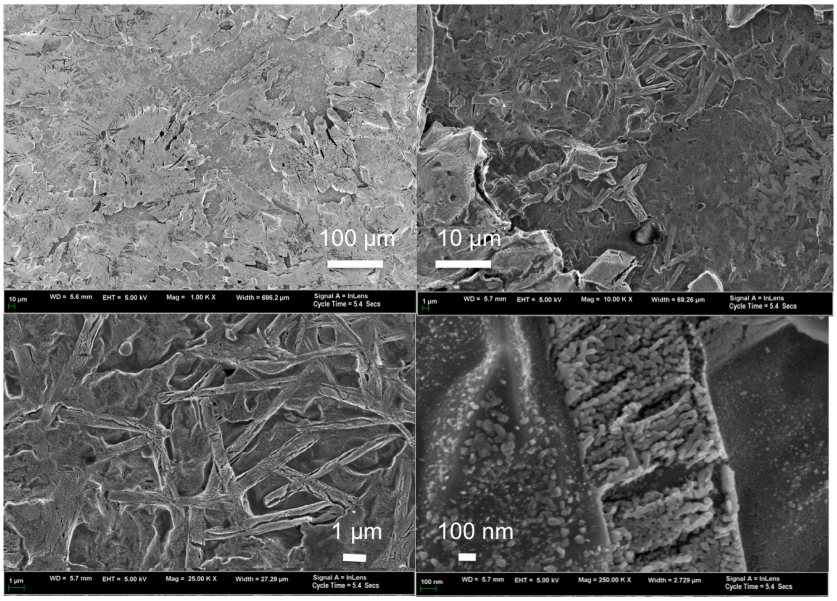

Figure 3.3. Micrographs of an as-deposited $(Ru_{0.09}Co_{0.91})_3O_4$ electrode tab.

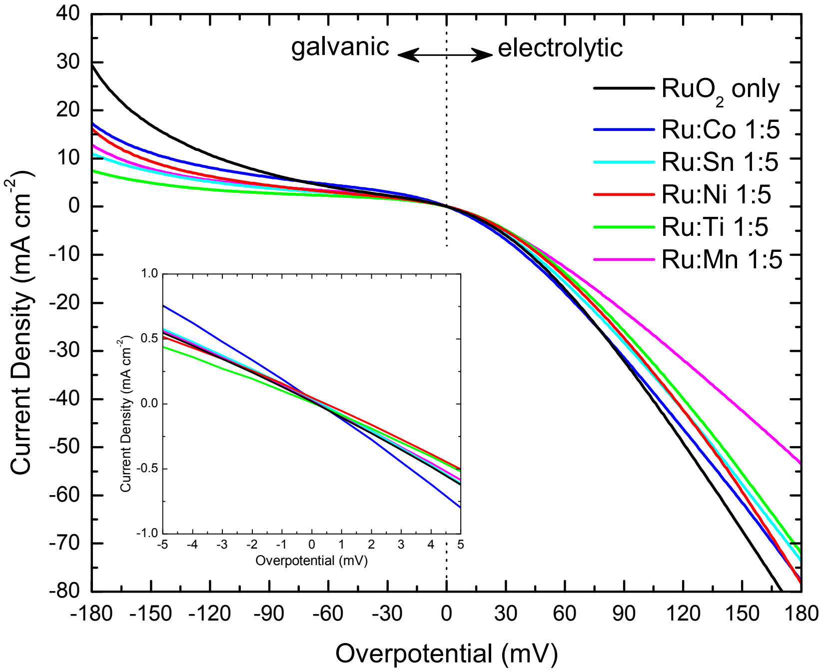

Figure 3.4. Current-potential curves for a variety of metal oxide alloy catalysts, all at a 1:5 molar ratio of ruthenium to another metal. Inset is a zoom of the curves at low overpotentials (i.e. near equilibrium).

Table 3.2. Calculated exchange current densities for various oxide alloy materials. All values are in mA cm^{-2}. For reference, the value for pure RuO_2 is 4.36 mA cm^{-2}. The largest value in each column is in red, and the largest value in each row is in bold.

	1:1	**1:5**	**1:10**	**1:20**	**1:50**
Ru:Co	2.52	**3.91**	2.63	2.69	1.23
Ru:Ni	**3.43**	3.04	3.33	2.55	0.71
Ru:Ti	**2.64**	1.82	0.58	0.25	
Ru:Sn	1.34	**3.00**	0.31	0.33	
Ru:Mn	0.90	**2.91**	1.75		

Looking at the ruthenium-cobalt alloys more closely, Figure 3.5 shows half-cell results for a concentration series with decreasing Ru content. First, the Ru:Co 1:1 and Ru:Co 1:10 alloys actually outperform pure RuO_2 at large negative overpotentials. In the eletrolytic direction, the Ru:Co 1:5 alloy comes closest to matching the performance of pure RuO_2 at large overpotentials. Zooming in near equilibrium, though, it is clear from the inset that Ru:Co 1:5 has the highest catalytic activity, with a calculated exchange current density of 3.91 mA cm^{-2}. One reason for this could be that the 1:5 alloy is the alloy with the highest Ru content that still exhibits the spinel structure of Co_3O_4. Figure 3.6 shows x-ray diffraction results for the Ru-Co concentration series. The diffraction peaks for the 1:5, 1:10, 1:20, and 1:50 alloys can all be accounted for by the expected peaks in pure Co_3O_4 (the amorphous hump seen in some of the patterns can likely be attributed to the glass substrate on which the oxide materials were deposited). Looking at Figure 3.6c, the Ru:Co 1:1 alloy clearly adopts a different crystal structure than the others, exhibiting some peaks that can be attributed to rutile RuO_2. Note that complete miscibility of the oxides is also attainable in the Ru-Ti systems commonly used in DSAs [43].

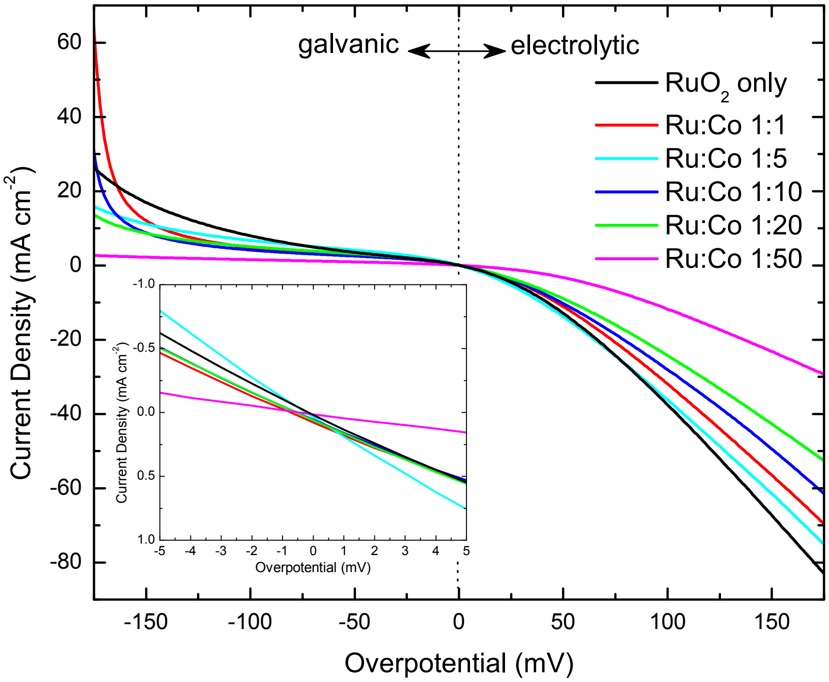

Figure 3.5. Current-potential curves for ruthenium-cobalt oxide alloys at a variety of Ru:Co molar ratios. Inset is a zoom of the curves at low overpotentials (i.e. near equilibrium).

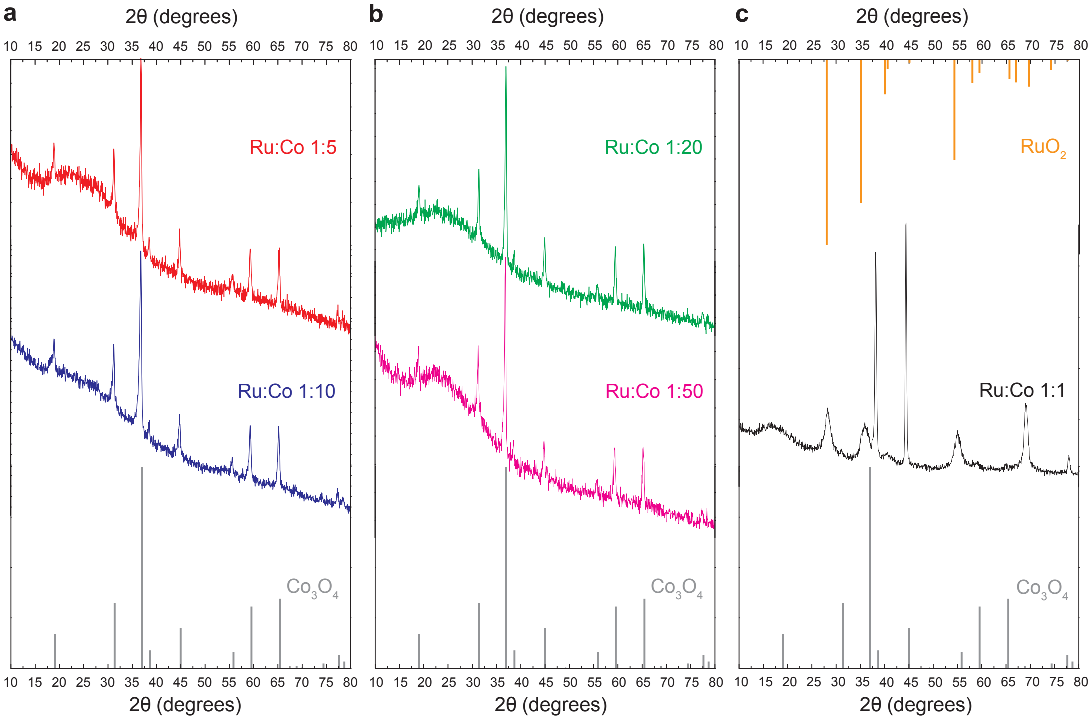

Figure 3.6. X-ray diffraction results for ruthenium-cobalt oxide alloys at a variety of Ru:Co molar ratios. (**a**) Ru:Co 1:5 and Ru:Co 1:10, with the expected lines for the spinel form of Co_3O_4 on the bottom. (**b**) Ru:Co 1:20 and Ru:Co 1:50, with the expected lines for the spinel form of Co_3O_4 on the bottom. (**c**) Ru:Co 1:1, which exhibits a different structure than the other compositions, with the expected lines for the spinel form of Co_3O_4 on the bottom and the expected lines for the rutile form of RuO_2 on the top.

The other oxide alloy of particular interest was ruthenium-nickel, since this material was predicted by theory[iii] to be a good catalyst for the chlorine redox reactions. Figure 3.7 shows a concentration series of Ru-Ni oxide alloys. The Ru:Ni 1:1 alloy is the best performer overall, but the 1:5, 1:10, and 1:20 alloys also perform reasonably well. There is no discernible trend in performance here, either because the nickel oxides are relatively insensitive to ruthenium content, or because of noise introduced in the results due to widely varying surface areas. The latter could be due to varying driving forces for crystal nucleation and growth, phenomena that are very sensitive to pretreatment and oxide formation conditions. Despite this, it is clear that Ru-Ni oxide alloys are capable of performing reasonably well when compared to pure RuO_2 electrodes.

Besides catalytic activity, another important property of these catalysts is their durability: their ability to withstand low pH and both oxidative and reductive potentials. To test the durability of the oxide alloy under operational conditions, an Ru:Co 1:10 electrode was cycled between ± 200 mV overpotentials (i.e. the potential was held at a -200 mV overpotential for 20 seconds, then stepped to +200 mV for 20 seconds, then stepped back down, and so on). This electrode was slightly different than the others tested previously in that, before the alloy material was deposited, the substrate was oxidized to form a native oxide layer on the substrate to improve the adhesion of the deposited alloy.[iv] This helps to minimize delamination of the film over time. Figure 3.8 shows the results from 2400 cycles. This plot is best understood by first looking at the inset, which

---

[iii] Theoretical work was done by Süleyman Er and will be included in an upcoming publication.

[iv] The exact nature of this oxide is unclear, as niobium exhibits unusual oxidation features that are strongly dependent on temperature, pressure, and the nature of the Nb surface [76]. The oxide generated here likely consists of a mixture of NbO_2 and NbO_x where x is close to 0.5 [77]. Both of these adopt a tetragonal structure. NbO_2 is a semiconductor and NbO_x may exhibit an electrical conductivity comparable to NbO, which is metallic [78]. The lower current densities observed in Figure 3.8 as compared to Figure 3.5 are likely due to the resistivity of this oxide film.

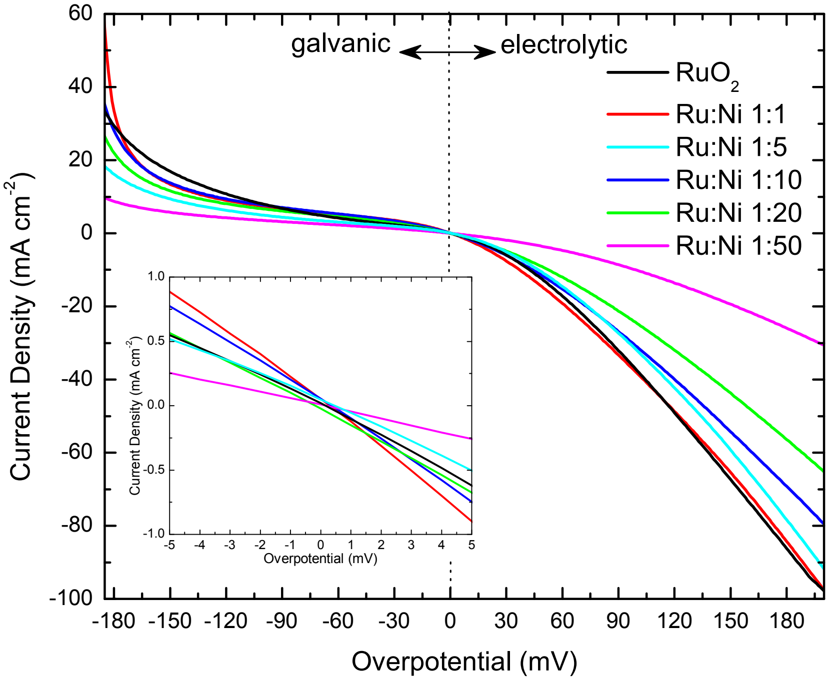

Figure 3.7. Current-potential curves for ruthenium-nickel oxide alloys at a variety of Ru:Ni molar ratios. Inset is a zoom of the curves at low overpotentials (i.e. near equilibrium).

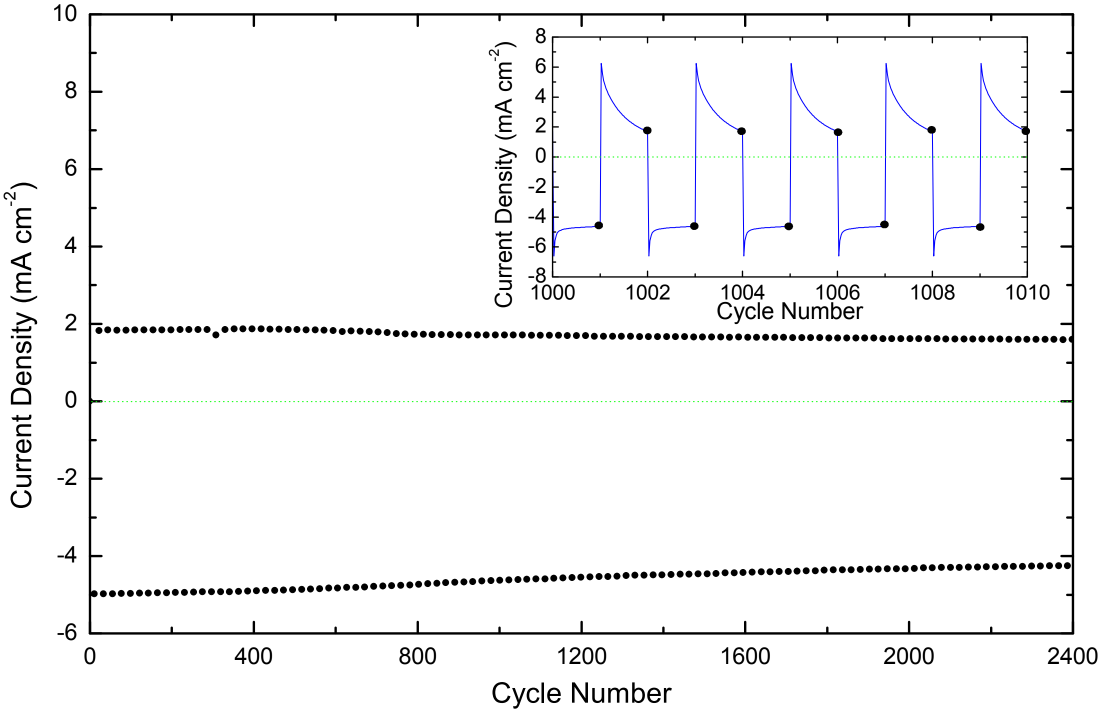

Figure 3.8. Cycling data for a Ru:Co 1:10 oxide alloy electrode. The potential was cycled between ± 200 mV overpotentials 2400 times, and the current response was measured. The inset shows a zoom of 5 cycles: the current at the end of each cycle is marked with a black dot. These dots are then plotted in the larger frame for the entirety of the 2400 cycles. A data point from every 11th cycle is shown.

shows a zoom on 10 cycles from the middle of the experiment. At the end of each cycle, the current density is marked with a black dot. These dots are then plotted in the main frame of the figure, zooming out to include all of the cycles (points are only shown for every 11th cycle due to the density of the data). Some minor fade in performance is apparent. After this test, small oxide alloy particles could be seen sitting on the bottom of the test glassware, almost certainly broken off by chlorine bubble formation, indicating that this performance fade may be due to physical loss of catalyst material from the electrode as opposed to chemical degradation or corrosion.

3.3 CONCLUSIONS

In this chapter, our exploration of a variety of oxide alloy catalyst materials was detailed. These materials were deposited onto niobium substrates using a standard wet-chemical-synthesis technique, forming highly polycrystalline thin films. Through a variety of half-cell measurements, ruthenium-cobalt oxide alloys were determined to be the most catalytically active material towards the CER and CRR. Measured exchange current densities were 3.91 mA cm^{-2} for the Ru:Co 1:5 ($(Ru_{0.17}Co_{0.83})_3O_4$) material and 2.63 mA cm^{-2} for the Ru:Co 1:10 ($(Ru_{0.09}Co_{0.91})_3O_4$) material. In both of these oxide alloys, they adopt the normal spinel structure of Co_3O_4, as confirmed by XRD analysis. For the Ru:Co 1:10 material, it is capable of being cycled a large number of times with only a small amount of loss in catalytic activity. Much of this loss may actually be attributable to mechanical degradation of the electrode, as Cl_2 bubble formation appears to slowly break off pieces of the catalyst material.

Further studies, including the development of a process for depositing thin, smooth films of this material, would be necessary to determine the complete degradation mechanisms for the electrodes and to provide exact measurements of the exchange current densities. Regardless, the goal of this project was to find stable, active, inexpensive catalyst materials for the CER/CRR, and these results indicate that ruthenium-cobalt alloys represent at least one promising class of materials that meets this goal.

4

Modeling the Hydrogen-Bromine Regenerative Fuel Cell

OUR MODELING EFFORTS began with the hydrogen-chlorine fuel cell, the results of which can be found in Refs. [10] and [13]. As our efforts began to shift towards alternate chemistries, we found it important to extend our model to a hydrogen-bromine system. This particular system has a couple advantages over a hydrogen-chlorine sytem. First, bromine is a liquid under standard conditions, simplifying system operation as compared to a two-phase gas-liquid system using chlorine. Second, bromine has a considerably higher solubility in its complementary acid (HBr) than chlorine does in its acid (HCl). This leads to much improved mass transport characteristics for a hydrogen-bromine system. With these advantages in mind, we set out to adapt our hydrogen-chlorine model to a hydrogen-bromine system. The majority of the text below can be found in our publication on this model titled, "Performance Model of a Regenerative Hydrogen Bromine Fuel Cell for Grid- Scale Energy Storage" [14].

The regenerative hydrogen-bromine fuel cell (rHBFC) is an energy storage device that facilitates the following electrochemical reaction:

$$\mathrm{H_2(g)} + \mathrm{Br_2(g)} \rightleftharpoons \mathrm{2HBr(aq)}. \tag{4.1}$$

Figure 4.1 shows a schematic of the cell. In discharge (galvanic) mode, H_2 and Br_2 react to produce electricity and HBr(aq). In charge (electrolytic) mode, electricity is consumed to split HBr(aq) into H_2 and Br_2, which is then stored in tanks until the electricity is needed.

Earlier studies on hydrogen-bromine electrochemical devices demonstrated promising performance. In a study by Yeo and Chin from 1980, round-trip electric-to-electric efficiencies were reported at about 70% for current densities between 150 to 225 mA cm^{-2}, depending on the electrolyte composition, with the cell capable of operation to at least 300 mA cm^{-2} [19]. Soon after, work on HBr electrolyzers led to devices capable of operating around 330 mA cm^{-2} in electrolytic mode [32]. In more recent work, Livshits *et al.* (2006) reported current densities in

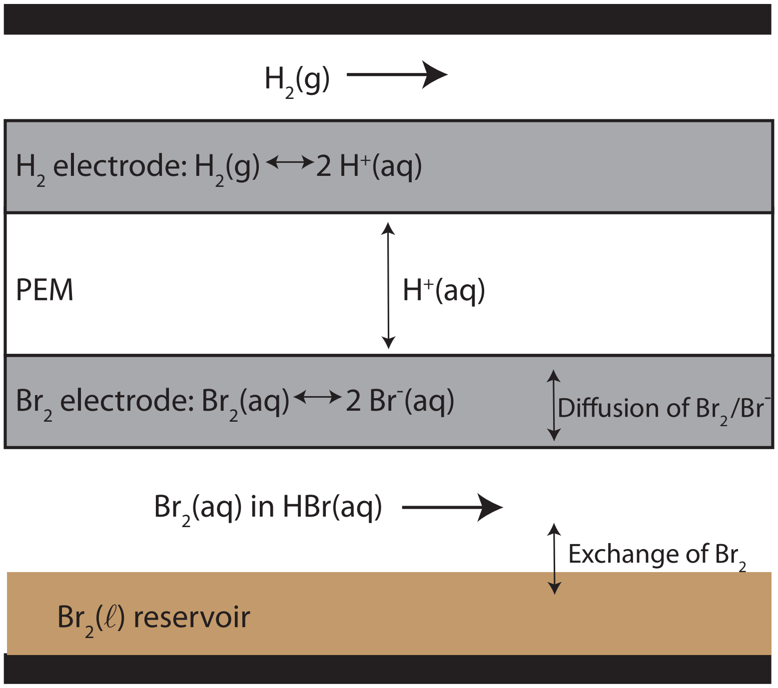

Figure 4.1. Schematic of a regenerative hydrogen-bromine fuel cell. In charge or electrolytic mode, hydrobromic acid is electrolyzed to produce hydrogen and bromine using electrical energy from an external source. The products are stored in tanks for future re-conversion to electricity. In discharge or galvanic mode, hydrogen and bromine react to produce hydrobromic acid and electricity.

excess of 2400 mA cm^{-2}, with the cell power density exceeding 1500 mW cm^{-2} at 80 °C, by utilizing a novel, non-standard membrane [23]. Kreutzer *et al.* (2012) achieved power densities exceeding 450 mW cm^{-2} near 750 mA cm^{-2} (at 45 °C) for a cell utilizing a standard Nafion membrane [79].

Modeling the performance of hydrogen-bromine systems has been done before [18, 19], with the most developed model coming from Savinell *et al.* [i] Our model differs from previous work in two key ways: (1) we include the effects of temperature on equilibrium potentials, membrane resistances, electrode activation kinetics, and mass transport of species to and from the electrode surface, and (2) we systematically vary the cell operating parameters, such as temperature and electrolyte composition, while also varying cell engineering parameters, discussed below, to identify performance "sweet spots." The large parameter space we explore is unrivaled in the literature. In exploring this large parameter space, certain simplifications were made (such as effectively reducing the mass transport behavior to a single engineering parameter) that allow us to explore a very broad range of possible cell characteristics, e.g. examining a cell with severe mass transport limitations vs. a cell with minimal mass transport limitations. This was done so that this model could be used as a guide to future R&D efforts, helping to identify aspects of the cell performance that demand the most attention.

4.1 THE MODEL

The purpose of this model is to determine the cell potential (in volts) as a function of current density (in mA cm^{-2}) for a given set of operating parameters (OPs: temperature and electrolyte composition) and engineering parameters (EPs: electrode exchange current densities, membrane

---

[i] Work on gas-phase systems has been done as well [80], but is not discussed here.

thickness, diffusion layer thickness, and H_2 gas pressure). In this study, we consider the EPs and OPs as well as the dependent physical properties that determine cell losses, such as proton exchange membrane (PEM) conductivity, electrode kinetics, and bromine/bromide mass transport in solution. Our objectives are to predict cell voltage efficiency and cell power density p as functions of current density and to determine how these functions change as we vary both the OPs and the EPs. The model was used to evaluate cell potentials in both charge mode and discharge mode, but for the majority of results presented here, we omit the electrolytic, charge-mode behavior. Typically, a cell that shows good performance in discharge mode also shows good performance in charge mode (particularly within the confined concentration range used in this model), allowing us to simplify the presentation of the model results. We primarily consider two different sets of EPs: a "Base Case" with relatively conservative values for the EPs, which should be attainable today, and a "More Optimal Case" that uses more optimistic values that should be attainable with further research and development. Justifications for the values of each of these parameters are provided in the relevant subsections of this chapter.

The energy conversion efficiency of the cell is the product of the voltage efficiency and the coulombic efficiency, and the round-trip efficiency of the device is the product of the energy conversion efficiency in galvanic mode and the energy conversion efficiency in electrolytic mode. The primary coulombic loss is via reactant crossover through the membrane, which we discuss later. If this loss is small enough, then the energy conversion efficiency is indistinguishable from the voltage efficiency. The voltage efficiency of the cell is a function of the current density i, with one expression for the galvanic direction and a different one for the electrolytic direction. In the galvanic case (which we take as defining positive i), hydrogen and bromine react to produce hydrobromic acid and electricity. The voltage efficiency is the electrical energy per charge produced (the cell potential $E(i)$), divided by the electrical energy per charge that could be produced reversibly (the equilibrium potential E_{eq}). In the electrolytic case (negative i), electrical energy is supplied to split HBr(aq) into H_2 and Br_2 for energy storage. Here, the voltage efficiency is the maximum possible electrical energy returned per charge stored, E_{eq}, divided by the electrical energy per charge spent in doing the electrolysis, $E(i)$:

$$\text{cell voltage efficiency} = \begin{cases} \frac{E(i)}{E_{eq}} & : i \geq 0 \ \ \text{(galvanic)} \\ \frac{E_{eq}}{E(i)} & : i \leq 0 \ \ \text{(electrolytic)}. \end{cases} \tag{4.2}$$

The power density (in mW cm^{-2}) is the amount of power produced per cell area. It is equal to the cell potential multiplied by the current density:

$$p = i \cdot E(i). \tag{4.3}$$

Because of the high cost of fuel cells per unit cell area, cells having high efficiencies at large power densities are desirable.

The cell potential deviates from its equilibrium value due to several loss mechanisms, all of which lead to the generation of heat in the cell. We identify four overpotentials in the cell: the hydrogen and bromine electrode overpotentials (η_H and η_{Br}; the latter actually includes two losses: one due to electrode activation and one due to mass transport limitations at the bromine electrode), and the membrane resistance overpotential (η_R). Each overpotential is a function of current density and depends on the OPs and a subset of the EPs.

The overall cell potential can thus be expressed as the equilibrium cell potential minus the individual losses:

$$E(i) = E_{eq} - \eta_R(i) - \eta_H(i) - \eta_{Br}(i), \tag{4.4}$$

where all of the above quantities are in volts. E_{eq} is a function of temperature and of the activities of the reactants and products, which themselves depend on temperature and concentration. η_R is determined by the conductance of the membrane, which depends on temperature, acid concentration, and membrane thickness. The overpotentials at the two electrodes arise from two different effects: an activation loss due to the kinetics involved with the electron transfer at the surface, and a mass transport loss due to the depletion of the reactants and enrichment of the products near the electrode surface at non-zero current densities. We ignore the mass transport effect at the hydrogen electrode due to presumed fast transport of gaseous hydrogen, whereas we include the bromine mass transport because of the relatively slow transport of $\mathrm{Br_2(aq)}$ in aqueous solution. This overpotential is denoted η_{MT}.

THE EQUILIBRIUM POTENTIAL, E_{eq}

The equilibrium potential is that of the combined half-cell reactions, where all potentials are relative to that of a standard hydrogen electrode (SHE):

$$H_2(g) \rightleftharpoons 2H^+(aq) + 2e^- \qquad E_{eq} = 0.000 \text{ V} \tag{4.5a}$$

$$Br_2(aq) + 2e^- \rightleftharpoons 2Br^-(aq) \qquad E_{eq} = 1.087 \text{ V}. \tag{4.5b}$$

The equilibrium potential can be described by the Nernst equation:

$$E_{\mathrm{eq,Nernst}} = E_0^{'} + \frac{R(T + 273.15)}{nF} \ln \left(\frac{a_{\mathrm{Br_2}} a_{\mathrm{H_2}}}{a^2_{\mathrm{HBr(aq)}}} \right), \tag{4.6}$$

where $R = 8.314\,\mathrm{J\,mol\,K^{-1}}$ is the universal gas constant, T is the temperature (in $^\circ$C), n is the number of electrons transferred in the reaction ($n = 2$ here), and $F = 96485\ \mathrm{C\,mol^{-1}}$ is Faraday's constant. The activities of Br_2, HBr and H_2 are denoted $a_{\mathrm{Br_2}}$, a_{HBr}, and $a_{\mathrm{H_2}}$, respectively. They are defined by the following equations:

$$a_{\mathrm{Br_2}} = \frac{\gamma_{\mathrm{Br_2}} c_{\mathrm{Br_2}}}{c_0}, \tag{4.7}$$

and

$$a_{\mathrm{HBr}} = \frac{\gamma_{\mathrm{HBr}} c_{\mathrm{HBr}}}{c_0}, \tag{4.8}$$

and

$$a_{\mathrm{H_2}} = \frac{\gamma_{\mathrm{H_2}} p_{\mathrm{H_2}}}{p_0}, \tag{4.9}$$

where $c_{\mathrm{Br_2}}$ and c_{HBr} are the concentrations of Br_2 and HBr, respectively (in molarity, M), c_0 is the standard concentration of 1 M, $p_{\mathrm{H_2}}$ is the H_2 gas pressure, p_0 is the standard pressure of 1 atm, and $\gamma_{\mathrm{Br_2}}$, γ_{HBr}, and $\gamma_{\mathrm{H_2}}$ are the activity coefficients of Br_2, HBr, and H_2, respectively .

$E_0^{'}$ is the temperature-dependent equilibrium potential when all activities are unity. $E_0^{'}$ must be chosen so that $E_{\mathrm{eq}} = 1.087$ V at the standard temperature, pressure, and concentration of 25 °C, 1 atm, and 1 M, respectively. Assuming the difference between reactant and product entropies is independent of temperature, $E_0^{'}$ is a linear function of temperature, whose slope is given by the entropy of formation divided by $2F$ [81, 82]:

$$E_0^{'} = 1.2679 - 0.0006105(T + 273.15). \tag{4.10}$$

This equation can then be substituted into the Nernst equation to provide a full expression for the cell equilibrium potential:

$$E_{\text{eq,Nernst}} = 1.2679 - 0.0006105(T + 273.15) + \frac{RT}{2F} \ln \left(\frac{a_{\text{Br}_2} a_{\text{H}_2}}{a^2_{\text{HBr(aq)}}} \right). \tag{4.11}$$

One method of approximating the equilibrium potential involves using Equation 4.11 and setting all of the activity coefficients equal to unity. This procedure provides what we term the "ideal" equilibrium potential, $\text{E}_{\text{eq,ideal}}$, with the following form:

$$E_{\text{eq,ideal}} = 1.2793 - 0.0006104(T + 273.15) + \frac{RT}{2F} \ln \left(\frac{[Br_2][H_2]}{[HBr(aq)]^2} \right) \tag{4.12}$$

where $[\text{Br}_2]$ and $[\text{HBr(aq)}]$ represent the normalized concentrations of bromine and hydrobromic acid (i.e. $[\text{Br}_2] = c_{\text{Br}_2}/c_0$ and $[\text{HBr}] = c_{\text{HBr}}/c_0$) and $[\text{H}_2]$ represents the normalized pressure of H_2 gas (i.e. $[\text{H}_2] = p_{\text{H}_2}/p_0$).

Another way we calculate the equilibrium potential is to use a semi-empirical expression from Yeo and Chin [19]. The expression takes the following form:

$$E_{\text{eq,Yeo}} = \varphi - (T - 25) \left(4.3 + 1.86 \cdot \ln \frac{12.36X}{1 - X} \right) \cdot 10^{-4} + 4.31 \cdot 10^{-5} \cdot T \left(\ln f_{\text{H}_2} + \ln a_{\text{Br}_2} \right) \tag{4.13}$$

where X is the weight fraction of HBr in solution, f_{H_2} is the fugacity of H_2 gas, and φ takes the following form:

$$\varphi = \begin{cases} 1.073 - 0.0567 \cdot \ln\frac{12.36X}{1-X}, & \text{if } 0.016 < X < 0.11 \\ 1.095 - 0.1042 \cdot \ln\frac{12.36X}{1-X}, & \text{if } 0.11 < X < 0.28 \\ 1.336 - 0.2581 \cdot \ln\frac{12.36X}{1-X}, & \text{if } 0.28 < X < 0.58 \end{cases} \cdot \tag{4.14}$$

To compute the weight fraction of HBr in solution, X, we use the following expression:

$$X = \frac{\mathrm{MW_{HBr}M}}{\rho_{\mathrm{HBr}}} \tag{4.15}$$

where $\mathrm{MW_{HBr}}$ is the molecular weight of HBr (80.91 g mol^{-1}), M is the molarity of HBr (in mol L^{-1}), and ρ_{HBr} is the density of HBr(aq) (in g L^{-1}).

The density itself is a function of temperature and concentration, and has been presented in empirical form by Novotný and Söhnel [83]:

$$\rho_{\mathrm{HBr(aq)}} = \rho_{\mathrm{H_2O}} + A_\rho M + B_\rho MT + C_\rho MT^2 + D_\rho M^{3/2} + E_\rho M^{3/2}T + F_\rho M^{3/2}T^2 \tag{4.16}$$

where the temperature-dependent density of water, $\rho_{\mathrm{H_2O}}$ (in g L^{-1}) is given by the empirical expression:

$$\rho_{\mathrm{H_2O}} = 999.65 + 0.20438T - 0.06174T^{3/2}. \tag{4.17}$$

The parameters are as follows: $A_\rho = 59.98$, $B_\rho = -0.1300$, $C_\rho = 0.001061$, $D_\rho = -1.263$, $E_\rho = 0.02160$, and $F_\rho = -0.0001647$, each having units necessary to give their respective terms

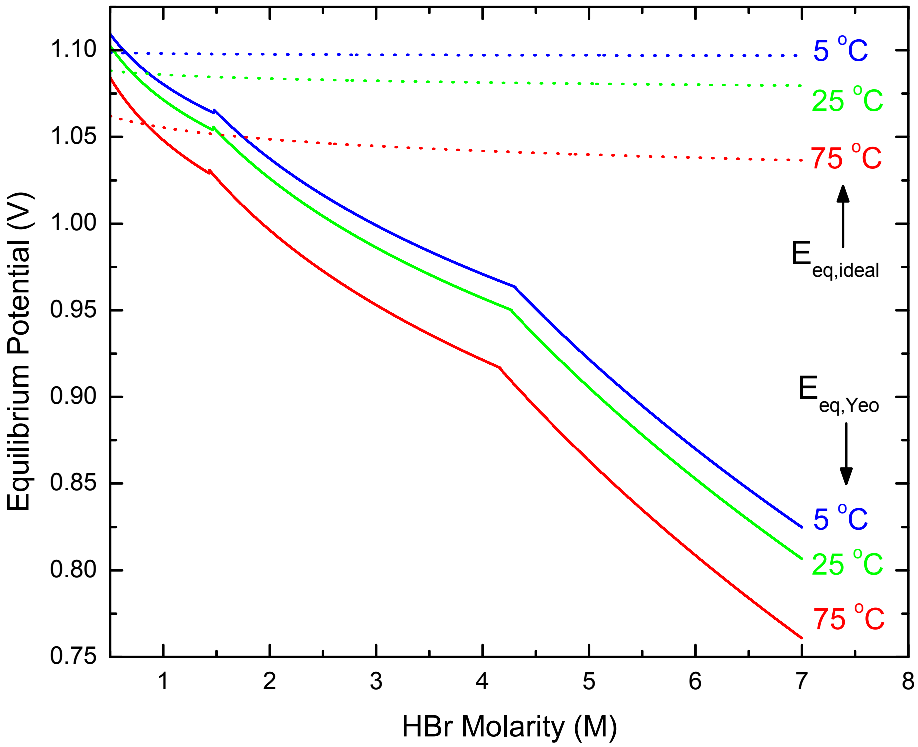

Figure 4.2. Equilibrium potential vs. HBr molarity at 5 °C, 25 °C, and 75 °C, calculated using Equations 4.12 ($E_{eq,ideal}$, dotted lines) and 4.13 ($E_{eq,Yeo}$, solid lines). Strong deviations from ideality are seen at high acid concentrations for $E_{eq,Yeo}$. The three "tiers" seen in $E_{eq,Yeo}$ result from the definition of φ in Equation 4.14.

density units of g L^{-1}.

This expression for the equlbrium potential from Yeo and Chin is in some sense the most useful, as it accounts for a lot of non-ideal behavior because it is a semi-empirical expression based on real cell measurements. Importantly, $E_{eq,Yeo}$ and $E_{eq,ideal}$ vary significantly from one another. Figure 4.2 highlights this, showing calculated curves for $E_{eq,Yeo}$ and $E_{eq,ideal}$ at 5 °C, 25 °C, and 75 °C. For subsequent calculations in this article, $E_{eq,Yeo}$ is used to represent the cell equilibrium potential.

THE MEMBRANE RESISTANCE OVERPOTENTIAL, η_{R}

The resistance of the proton exchange membrane is very important in determining the operational characteristics of a hydrogen-bromine cell. The membrane conductance (the reciprocal of the resistance) depends on the thickness of the membrane and the membrane conductivity, which is itself a function of temperature and acid concentration. The membrane conductivity is assumed to be independent of the membrane thickness and of the Br_2 concentration in solution. The resistance overpotential is calculated as follows:

$$\eta_R = \frac{l}{\sigma}\frac{i}{1000} \tag{4.18}$$

where l is the membrane thickness (in cm), σ is the membrane conductivity (in $\Omega^{-1}\mathrm{cm}^{-1}$), i is the current density (in mA cm^{-2}), and η_{R} is the resistive overpotential (in volts). The factor of 1000 assures consistency in units. Commercial DuPont Nafion membranes are typically available in thicknesses ranging from 25 to 250 μm. In the Base Case presented here, a value of 125 μm is used for the membrane thickness (equivalent to Nafion 115). The More Optimal case uses a 25 μm thick membrane (Nafion 211). From a voltage loss perspective, it always helps to decrease the thickness of the membrane, though this can only be done to a certain extent in practice: mechanical integrity of the membrane is very important, as membrane rupture would allow the uncontrolled mixing and reaction of H_2 and Br_2. Furthermore, reactant crossover increases with the use of thinner membranes, lowering the current efficiency of the cell. Thus, the membrane thickness is also practically limited by the degree of reactant crossover that can be tolerated in a given system. Yeo and McBreen (1979) measured the extent of bromine crossover under a variety of electrolyte concentrations [30]. Steady-state crossover current densities were reported as high as 3.57 mA/cm^2 for Br_2 in 12% HBr and as low as 0.0135 mA/cm^2 for Br_2 in 48% HBr for a Nafion 120 (250 μm thick) membrane. Assuming the crossover is inversely proportional to the membrane thickness, this would result in crossover current densities ranging from 0.135 mA cm^{-2} to 35.7 mA cm^{-2} in a 25 μm thick membrane, or 0.027 mA cm^{-2} to 7.14 mA cm^{-2} in a 125 μm thick membrane. The upper end of this range would represent a significant coulombic loss in a real cell, while the lower end would essentially be negligible. Further experimental studies are necessary to determine which end of this range is more applicable to cells of interest, and considerations of the crossover current density are essential in determining the ideal operating conditions (especially HBr/Br_2 concentrations) for this type of cell.

The membrane conductivity is a complicated function of both HBr(aq) concentration and temperature. Data from both Baldwin [84] and Sone *et al.* [85] were used for the calculations here, with the latter providing activation energies for proton conduction in Nafion in pure water (i.e. 0 M acid). The conductivity is assumed to take on an Arrhenius form:

$$\sigma(\mathrm{M,T}) = \mathrm{A(M)}e^{\frac{-E_a(M)}{RT}} \tag{4.19}$$

where A(M) is a pre-exponential factor (in $\Omega^{-1}\mathrm{cm}^{-1}$) and $E_a(M)$ is an activation energy (in J mol^{-1}). Baldwin provides data for σ and E_a at five different molarities ranging from 1.34 M HBr to 7.32 M HBr (a total of 23 data points). Sone *et al.* provide data for σ and E_a at 0 M HBr (i.e. Nafion in pure water). Using these values, the pre-exponential factor A can be calculated for the six molarities studied in these references. Now, having values for A(M) and E_a(M) at six different molarities, Equation 4.19 can be used to calculate values for σ at any given temperature for each of the six molarities. A spline interpolation was then done in Matlab ®using the six curves drawn from Equation 4.19, so that σ could be calculated for an arbitrary value of the acid concentration

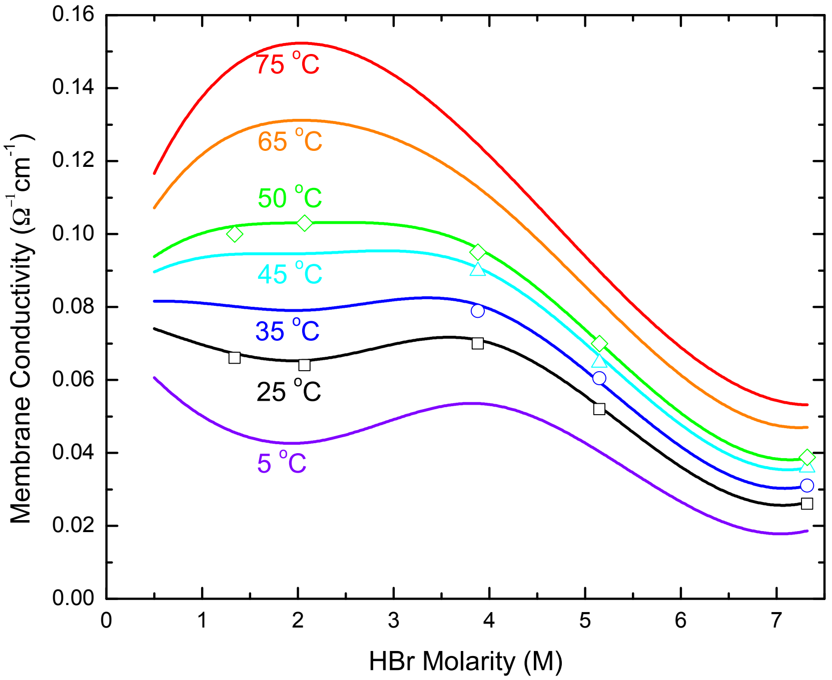

Figure 4.3. Membrane conductivity vs. acid molarity at several different temperatures, calculated using data from both Baldwin and Sone *et al.* The data points shown are a subset of those provided by Baldwin [84].

between 0 M and 7.32 M. Figure 4.3 shows the membrane conductivity as a function of HBr molarity at a variety of temperatures. A subset of the data from Baldwin is included to indicate the quality of the fits. Notice that, at 5 °C, the conductivity experiences a local maximum near 4 M and a local minimum near 2 M. As the temperature is increased, the local maximum shifts to lower concentrations, and the local minimum disappears altogether, consistent with data from Baldwin. For temperatures $\geq$ 50 °C, the conductivity peaks near 2 M.

THE HYDROGEN ELECTRODE OVERPOTENTIAL, η_{H}

The activation overpotential at the hydrogen electrode, η_{H} (in volts), is defined using a concentration-independent form of the Butler-Volmer equation:

$$i = i_0^H \left[\exp\left(\frac{-\alpha F \eta_{\mathrm{H}}}{RT} \right) - \exp\left(\frac{(1-\alpha) F \eta_{\mathrm{H}}}{RT} \right) \right] \tag{4.20}$$

where i_0^H is the exchange current density of the structured hydrogen electrode (in mA cm^{-2}) and α is the transfer coefficient [86]. We neglect the effects of mass transport at the hydrogen electrode due to presumed fast transport of H_2 gas. For the model, we set the value of the transfer coefficient for both electrodes equal to 0.5. We invert Equation 4.20 numerically to obtain η_H as a function of i.

One important consideration is that the real surface area of the electrode is typically different, and often vastly different, than the projected surface area of the electrode. In a PEM fuel cell, electrodes are usually made up of finely dispersed catalyst particles that have a collective surface area much larger than the geometric area of the electrode. Technically, i_0 may also depend on temperature, but we ignore this dependence because of the uncertainty in the catalytic activity and because the area multiplier is much more significant.

The exchange current density of real hydrogen electrodes has been studied in detail in the context of hydrogen-oxygen PEM fuel cells. Neyerlin *et al.* (2007) report that for a structured fuel cell electrode, the increase in the effective hydrogen exchange current density over that of a single crystal surface can be as large as a factor of 500 [29]. They measured i_0^H values in the range 250-600 mA cm^{-2}. For the Base Case in this study, we set i_0^H equal to 250 mA cm^{-2}, and for the More Optimal Case, we set i_0^H equal to 600 mA cm^{-2}, based on these measurements. Note that all of the exchange current densities used in the model refer to structured electrodes with real surface areas considerably higher than the projected surface areas of the electrodes.

THE BROMINE ELECTRODE OVERPOTENTIAL, η_{Br}

In galvanic mode, the consumption of Br_2 and production of Br^- result in a depletion of Br_2 near the electrode and an enrichment of Br^-. The opposite occurs in electrolytic mode. For a given current density, the transport behavior of the system stabilizes at a steady-state concentration of reactant and product, so long as there exists a boundary somewhere in the system with a stable concentration and enough time is allowed to reach this steady state. In this case, we can express the concentrations of Br_2 and Br^- near the electrode as functions of current density.

The full, concentration-dependent Butler-Volmer equation describes the total bromine electrode overpotential:

$$i = i_0^{Br} \left[\frac{C_O^s(i)}{C_O^{bulk}} \exp\left(\frac{-\alpha F \eta_{\mathrm{Br}}}{RT} \right) - \frac{C_R^s(i)}{C_R^{bulk}} \exp\left(\frac{(1-\alpha) F \eta_{\mathrm{Br}}}{RT} \right) \right], \tag{4.21}$$

where C_O^{bulk} and C_R^{bulk} are the bulk concentrations of the oxidized and reduced forms, respectively, $C_O^s(i)$ and $C_R^s(i)$ are their respective concentrations near the electrode surface (all in mol cm^{-3}), and i_0^{Br} is the bromine electrode exchange current density (in mA cm^{-2}). The oxidized form is Br_2 and the reduced form is Br^-.

Values approaching 200 mA cm^{-2} for i_0^{Br} have been measured on structured commercial Pt/C electrodes with loadings of about 0.55 mg Pt cm^{-2} [79]. Values for i_0^{Br} on vitreous carbon are closer to 40 mA cm^{-2}, based on estimates by Savinell *et al.* [18], with this estimate based on work by White *et al.* [87] and Mastragostino *et al.* [88]. In our model, the bromine electrode exchange current density is set to 40 mA cm^{-2} for the Base Case, and 400 mA cm^{-2} for the More Optimal Case. We later vary this value (Figures 4.9 - 4.10) to show how it affects the cell performance.

We are interested in separating the losses that arise from mass transport and those that arise from activation of the charge-transfer reaction. In order to do this, we define the mass transport overpotential, η_{MT}, as the total bromine overpotential (η_{Br}, obtained from Eq. 4.21) minus the activation overpotential (η'_{Br}, obtained from Eq. 4.20, applied to bromine instead of hydrogen):

$$\eta_{\mathrm{MT}} \equiv \eta_{\mathrm{Br}} - \eta'_{\mathrm{Br}}. \tag{4.22}$$

To find η_{MT}, we determined the flux of reactants to the surface (and products away from it). The diffusive flux, J (in mol cm^{-2} s^{-1}) is given by

$$J = -D\frac{dC}{dx} \approx -D\frac{\Delta C}{\Delta x}, \tag{4.23}$$

where in the second expression we have made the linear concentration gradient approximation across the bromine-side electrode. D is the diffusion coefficient (in cm^2 s^{-1}). For diffusion of Br_2(aq), we label the diffusion coefficient D_{Br_2}. Δx is equal to ε, the diffusion layer thickness, and ΔC is the concentration difference across the thin film, namely $C_O^s(i) - C_O^{bulk}$ (in mol cm^{-3}). For each mole of Br_2 that diffuses to the electrode surface to react, $2F$ coulombs of electrons pass through the external circuit for bromine reduction. Thus, the flux is expressed as a current density according to $i = 2FJ \cdot 1000$, where the factor of 1000 is necessary for conversion from A to mA. Equation 4.23 can be solved for $C_O^s(i)$:

$$C_O^s(i) = C_O^{bulk} - \frac{\varepsilon}{2FD_{Br_2}}\frac{i}{1000}. \tag{4.24}$$

Ideally, data for D_{Br_2} as a function of temperature, Br_2 concentration, and HBr concentration would be used here, but such data do not appear to exist in the literature. As a result, we rely on a modified version of the Wilke-Change correlation [89] provided by Reddy and Doraiswamy for estimating liquid diffusivities [90]. The following equation is used to calculate D_{Br_2} in pure water (based on Equation 2 in Reddy *et al.*):

$$D_{\mathrm{Br}_2} = 10^{-7} \cdot \frac{(MW_{\mathrm{H_2O}})^{\frac{1}{2}}\, T}{\mu\, (V_1)^{\frac{1}{3}}\, (V_2)^{\frac{1}{3}}} \tag{4.25}$$

where $MW_{\mathrm{H_2O}}$ is the molecular weight of water (18.0153 g mol^{-1}), μ is the viscosity of the solution (in centipoise), V_1 is the molecular volume of the pure solute (in $\mathrm{cm}^3\ \mathrm{mol}^{-1}$), and V_2 is the molecular volume of the solvent, i.e. water (in $\mathrm{cm}^3\ \mathrm{mol}^{-1}$). In the case of bromine, V_1 is equal to 53.2 $\mathrm{cm}^3\ \mathrm{mol}^{-1}$, and for water V_2 is 18.9 $\mathrm{cm}^3\ \mathrm{mol}^{-1}$ [89]. The viscosity itself is temperature dependent, and can be calculated for H_2O using Equation 11 from Laliberté [91]:

$$\mu = \frac{T + 246}{(0.05594T + 5.2842)T + 137.37}. \tag{4.26}$$

Plugging Equation 4.26 into Equation 4.25 provides an expression for the diffusivity of Br_2 in H_2O. At 25°C , the calculated diffusion coefficient for Br_2 is 1.42 x 10^{-5} $\mathrm{cm}^2\ \mathrm{s}^{-1}$. We assume that this diffusivity is independent of the HBr concentration. For low concentrations of either HBr or Br_2, this assumption is reasonable. As the concentrations get higher and complexed species like Br_3^- and Br_5^- become more prevalent, then the diffusivity calculated here likely overestimates the real value for D_{Br_2}.

Bromine speciation can be very important to a system like this, particularly in the high concentration regimes, where Br_3^- and Br_5^- concentrations are likely significant. There is also the possibility of bromine hydrolysis, which is discussed elsewhere [92, 93]. In principle, Br_3^- and Br_5^- formation would affect both the electrode kinetics and mass transport through the system. There is some evidence that Br_3^- reduction occurs via a mechanism where Br_3^- first forms Br_2, which Br_3^- is in rapid equilibrium with, followed by reduction of Br_2 [88]. If this equilibrium is fast, then Br_3^- formation will likely have little effect on the observed electrode kinetics. The effect on transport will likely be more pronounced: as the concentrations of Br_3^- and Br_5^- increase, the mass transport limit will be adversely affected, as these species will have lower diffusion coefficients than that of Br_2. This is an important consideration, and future modeling efforts that involve a more complex mass transport model will need to account for such effects.

We model the bromide mass transport in a similar way to the bromine transport, with a few key differences. As Br_2 is reduced at the electrode, Br^- is produced and the local concentration, $C_R^s(i)$, increases. Protons also enter through the electrode at the same flux as the bromide is generated. As the concentrations increase at the electrode surface, the concentration gradient generates a diffusive flux of Br^- and H^+ away from the electrode.

The surface concentration is then modeled by:

$$C_R^s(i) = C_R^{bulk} + \frac{\varepsilon}{FD_{Br^-}} \frac{i}{1000}. \tag{4.27}$$

Note that the sign has changed (relative to Equation 4.24) because positive fluxes of Br^- require negative current densities. Also, a factor of two is absent from the second term because there is one charge per bromide ion, as opposed to two charges per bromine molecule in the previous case.

To estimate the diffusivity of Br^- in solution, we use Equations 4.25 and 4.26, with only the value of V_1 changing – to 27 $cm^3\ mol^{-1}$ for Br^-. At 25°C , the calculated value for D_{Br^-} is 1.78 x

10^{-5} cm^2 s^{-1}.

The last term to discuss here is the diffusion layer thickness $\Delta x = \varepsilon$ from Equation 4.23. This is the primary factor in determining the mass transport characteristics of the cell. A smaller value for ε results in larger diffusive fluxes of reactant to the surface, and therefore higher limiting current densities. In a real cell, the value for ε is a complicated function of the electrode and flow channel geometry and solution flow rates. For a simplified model, we assume that the value for ε is at most the thickness of the electrodes (i.e. approximately 125 μm) for the Base Case. This is akin to a cell setup where solution is being pumped over a porous, planar electrode and the limiting step in mass transport is diffusion of the active species through the electrode. Of course, real cells often add convective transport to this as well (by using interdigitated flow fields, for example), and so the effective values for ε seen are much lower than the electrode thickness. A lower bound on ε can be estimated using fluid mechanics. Assuming a porous, fibrous electrode with fiber diameters on the order of 10 μm, and assuming that the diffusion layer thickness is set by the formation of a boundary layer across these fibers, the thickness of this layer can be estimated using the Blasius solution for laminar flow over flat plates:

$$\varepsilon \approx 4.91 \left(\frac{\nu x}{u_0} \right)^{\frac{1}{2}} \tag{4.28}$$

where ν is the kinematic viscosity, x is the distance downstream from the beginning of the boundary layer, and u_0 is the free velocity. Using reasonable values for each of these parameters that result in the lowest possible ε (ν = 0.3 x 10^{-6} m^2 s^{-1}, x = 10 μm, and u_0 = 0.1 m s^{-1}), a value of ε = 25 μm is found. Therefore, in this model, we set ε to 125 μm for the Base Case, where the diffusion layer is the entire thickness of the electrode, and to 25 μm for the More Optimal Case, where the diffusion layer is set by the formation of a boundary layer across the electrode fibers.

In the exploration of OPs reported here, the cell temperature is varied from 5 °C to 75 °C, and the HBr(aq) molarity from 0.5 M to 7 M. The $Br_2(aq)$ concentration is always held equal to the HBr(aq) concentration. This is effectively modeling a cell in which there is a large reservoir of $Br_2(\ell)$ sitting underneath an aqueous mixture of $Br_2(aq)$ in HBr(aq). In general, as the HBr(aq) concentration increases as the cell is discharged, the solubility of Br_2 in the upper aqueous phase increases, both HBr(aq) and $Br_2(aq)$ concentrations in the upper phase increase, and the $Br_2(\ell)$ reservoir is depleted. This continues until the $Br_2(\ell)$ reservoir is gone, and then the $Br_2(aq)$ concentration begins to fall until it approaches zero. This model assumes that the $Br_2(\ell)$ reservoir is never completely consumed, so that the $Br_2(aq)$ concentration continuously increases with the HBr(aq) concentration in discharge mode. In charge mode, we make the same assumption – that an upper aqueous phase of $Br_2(aq)$ and HBr(aq) is in equilibrium with a $Br_2(\ell)$ reservoir – so that, as the HBr(aq) concentration falls in the aqueous phase, so does the $Br_2(aq)$ concentration.

4.2 RESULTS AND DISCUSSION

The model calculates the cell potential according to Equation 4.4, accounting for the various effects of concentration, temperature, and pressure on each of the overpotentials. The Base Case engineering parameters have the following values: hydrogen electrode exchange current density $i_0^H = 250$ mA cm^{-2}, Br_2 electrode exchange current density $i_0^{Br} = 40$ mA cm^{-2}, membrane thickness $l = 125$ μm, diffusion layer thickness $\varepsilon = 125$ μm, and H_2 gas pressure $p_{H_2} = 1$ atm. The More Optimal Case EPs have the following values: $i_0^H = 600$ mA cm^{-2}, $i_0^{Br} = 400$ mA cm^{-2}, $l = 25$ μm, $\varepsilon = 25$ μm, and H_2 gas pressure $p_{H_2} = 5$ atm. Figure 4.4 shows a directs comparison of the cell potential vs. current density and power density vs. current density for the Base Case and the

More Optimal Case. These calculations were done at 75 °C and 2 M HBr/Br_2,[ii] which are the operating parameters where the cell voltage efficiency is highest for both cases (see Figure 4.7). The maximum power density seen for the Base Case under these operating conditions approaches 530 mW cm^{-2}, with a limiting current density near 1200 mA cm^{-2} in galvanic mode. For the More Optimal Case in galvanic mode, the maximum power density is 2760 mW cm^{-2}, with a limiting current density just above 6000 mA cm^{-2}. In electrolytic mode, the limiting current density for the Base Case is about -750 mA cm^{-2}, and, for the More Optimal Case, the limiting current density in electrolytic mode is -3770 mA cm^{-2}. The limiting current densities are lower in the electrolytic direction because, when a mole of Br^- is oxidized, it frees 1 mole of electrons. In galvanic mode, when a mole of Br_2 is reduced, it liberates 2 moles of electrons. Thus, despite the higher diffusivity of Br^- in solution than Br_2, the limiting current density is actually lower in electrolytic mode.

Figure 4.5 shows calculated cell potentials for the (a) Base Case at 25 °C and 2 M HBr/Br_2, (b) More Optimal Case at 25 °C and 2 M HBr/Br_2, and (c) More Optimal Case at 75 °C and 2 M HBr/Br_2. The latter represents the conditions under which the cell efficiency is highest. The contributions of each of the individual losses are indicated as well. The horizontal dotted line shows the cell equilibrium potential.

Mass transport losses are minimal at relatively low current densities while, as the limiting current density is approached, mass transport losses dominate – until the cell potential is finally reduced to zero. It is also important to note that, at low current densities, the dominant loss for both the Base and More Optimal Cases is the bromine electrode overpotential. The relative

---

[ii] Since we maintain that the HBr and Br_2 concentrations are equal, this notation is referring to a solution of 2 M HBr(aq) and 2 M Br_2(aq) in H_2O. All subsequent notation is referring to equal concentrations of HBr and Br_2.

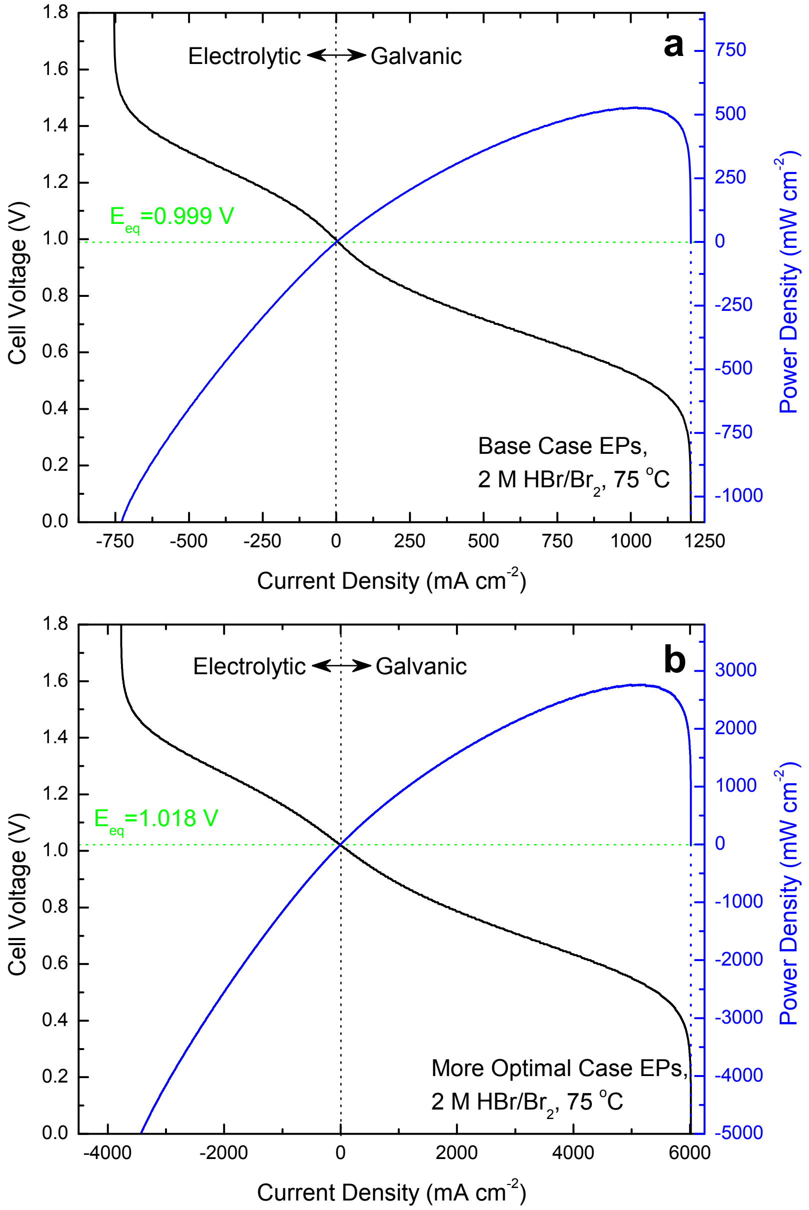

Figure 4.4. Voltage vs. current density (black) and power density vs. current density (blue) for the (**a**) Base Case and (**b**) More Optimal Case, both at 75 °C and 2 M HBr/Br$_2$ (the operating conditions that provide the highest voltage efficiency cell). The equilibrium potential is indicated with a green dotted horizontal line, and both galvanic and electrolytic operation are shown.

contributions of the losses are not vastly different between the Base Case and More Optimal Case: the hydrogen electrode activation overpotential is relatively more important in the More Optimal Case than in the Base Case because, in the More Optimal Case, the values of the bromine and hydrogen electrode exchange current densities are nearer one another. Comparing Figures 4.5b and 4.5c, the primary effects of raising the cell temperature are to increase the limiting current density due to enhanced reactant diffusivities and to improve the membrane conductivity, thereby reducing ohmic losses through the cell. The electrode kinetics becomes the most important factor affecting cell performance for the More Optimal Case cell operating under ideal conditions, indicating that electrode design is going to be an important factor in achieving high performance in these devices.

The two most relevant performance characteristics are the cell efficiency-vs.-current-density function and the maximum cell power density. On one hand, high cell efficiency is paramount for energy storage devices because lost energy is lost revenue. It is imperative that a storage device be able to operate at high efficiencies at reasonable current densities. On the other hand, operating at higher power densities reduces the capital cost for a given power-delivery capability, because one may buy less cell area for an equivalent power. The maximum power density also permits a determination of the minimum membrane area (and associated cost) necessary to achieve a required system power. In any real storage system (used to levelize wind power, for example), the cell operates over a distribution of current densities, constantly ramping up and down, depending on how much power is being generated by the turbines. Thus, both the maximum power density and the cell efficiency are important, so we explore both of these characteristics in this model. It is worth noting too, that, generally speaking, increasing the maximum power results in an efficiency increase over the entire current density range. It is important, however, to keep in mind that the

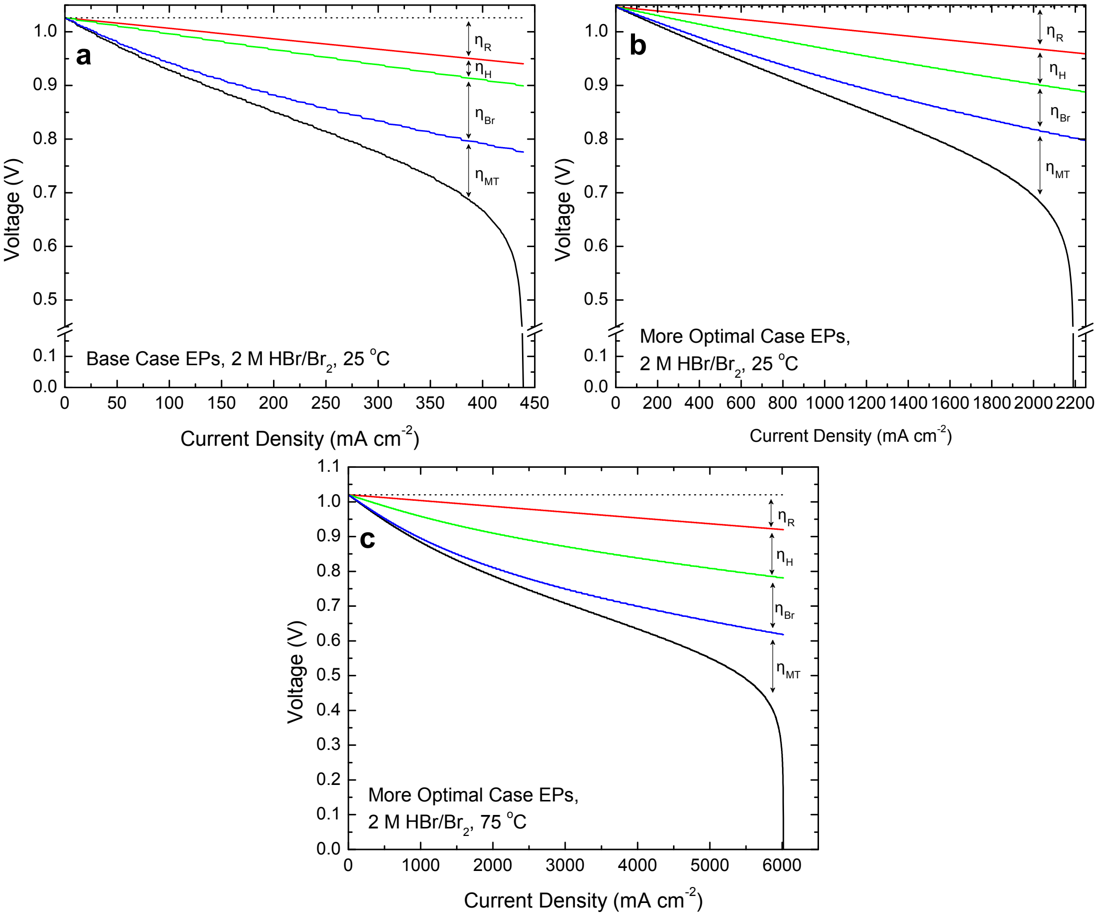

Figure 4.5. Voltage vs. current density for the (**a**) Base Case at 25 °C and 2 M HBr/Br$_2$, (**b**) More Optimal Case at 25 °C and 2 M HBr/Br$_2$, and (**c**) More Optimal Case at 75 °C and 2 M HBr/Br$_2$ (the operating conditions where the cell efficiency is highest). The contributions of each of the individual loss terms are indicated as well.

relative contributions of the individual loss mechanisms to the total loss may be significantly different at peak power than at high efficiency.

Varying the cell operating parameters of temperature and electrolyte composition drastically affects the cell performance, as demonstrated in Figure 4.6. The concentrations of HBr and Br_2 are varied for a cell operating at 25 °C with Base Case EPs in Figure 4.6a, and with the More Optimal Case EPs in Figure 4.6c. Increasing the concentrations leads to increased limiting current densities, but also, in accordance with the Nernst equation, leads to decreased equilibrium potentials. Note that in the 6 M HBr/Br_2 case for both Figures 4.6a and 4.6c, the mass transport limited current density is never actually reached: the cell potential goes to zero largely due to ohmic losses in the membrane. The behavior of a cell operating at 1 M HBr/Br_2 over three different temperatures is shown in Figure 4.6b for a cell with Base Case EPs, and in Figure 4.6d for a cell with More Optimal Case EPs. Increasing temperature leads to slightly reduced equilibrium potentials, but it also leads to significantly higher limiting current densities. All of the individual losses are reduced by increasing temperature, so, for this type of cell, higher temperatures always lead to higher voltage efficiencies.

Figure 4.7 shows how the maximum power density and galvanic power density at 90% voltage efficiency vary over the entire range of operating parameters explored, calculated using the Base Case EPs for the top row of the plots and the More Optimal Case EPs for the bottom row. For each combination of temperature and concentration (denoted by the points of intersection in the overlaid grid), a voltage vs. current density curve was calculated, similar to Figure 4.4, and, from this, a maximum power density and a galvanic power density at 90% voltage efficiency were calculated. The values of each of these were then plotted for every combination of temperature and concentration, forming the surfaces shown in Figure 4.7. As is evident from the figure, the

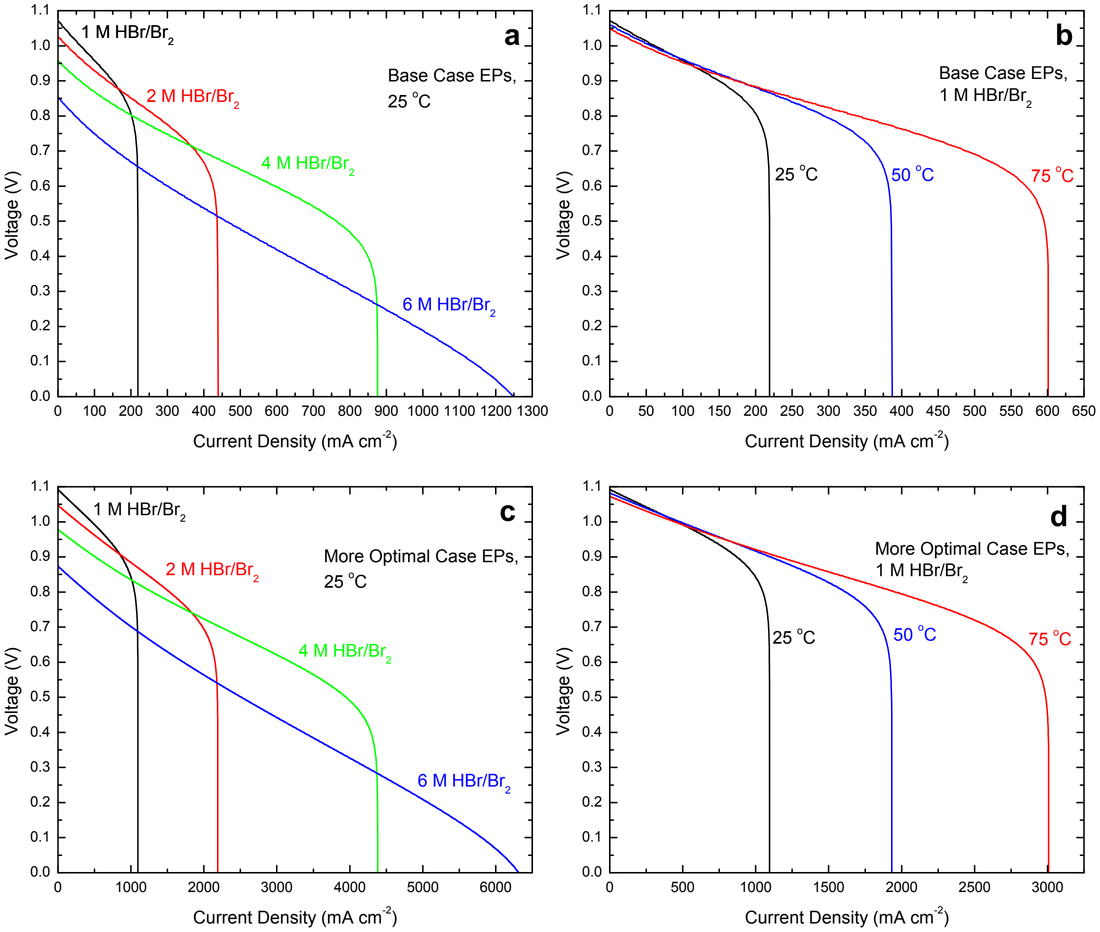

Figure 4.6. Voltage vs. current density over a range of operating conditions: (**a**) Base Case EPs, 25 °C, varying concentration; (**b**) Base Case EPs, 1 M HBr/Br$_2$, varying temperature; (**c**) More Optimal Case EPs, 25 °C, varying concentration; (**d**) More Optimal Case EPs, 1 M HBr/Br$_2$, varying temperature.

surfaces calculated for the Base Case and the More Optimal Case have a very similar shape. Furthermore, the effect of temperature is clear: higher temperatures lead to higher maximum power densities and higher power densities at 90% voltage efficiency. This is because an increased temperature reduces all of the individual losses. The effect of concentration is more complex, but, in general, the dominant effect is the membrane conductivity. At low temperatures, the conductivity has a local maximum near 4 M. As the temperature increases, this maximum shifts to lower molarities, and, at 75°C , the conductivity has an absolute maximum near 2 M. This explains the shift of the peak power density for a given temperature to lower molarities as the temperature is increased.

Figure 4.8 shows the cell voltage efficiency as a function of the galvanic power density under a variety of operating conditions for both the Base Case and the More Optimal Case. The dotted regions of each curve indicate areas of undesirable operation, as one would always choose to operate at the highest efficiency for a given power density.

Notice how, for the Base Case, the electrolyte composition has little effect on the predicted cell performance at 90% efficiency: only when the maximum power densities are approached do significant differences become evident. For the More Optimal Case running at 75 °C, the 1 M and 2 M curves are indistinguishable at high efficiencies, as both the membrane resistance and mass transport overpotentials are small there, but the curves do become quite different as the maximum power densities are approached. The mass transport limitation sets in first for the lower concentration. The 4 M curve is considerably worse over the majority of the efficiency range of interest, due to decreased membrane conductivity at this high acid concentration (see Figure 4.3); however, the high concentration forestalls the mass transport limitation, thereby reaching

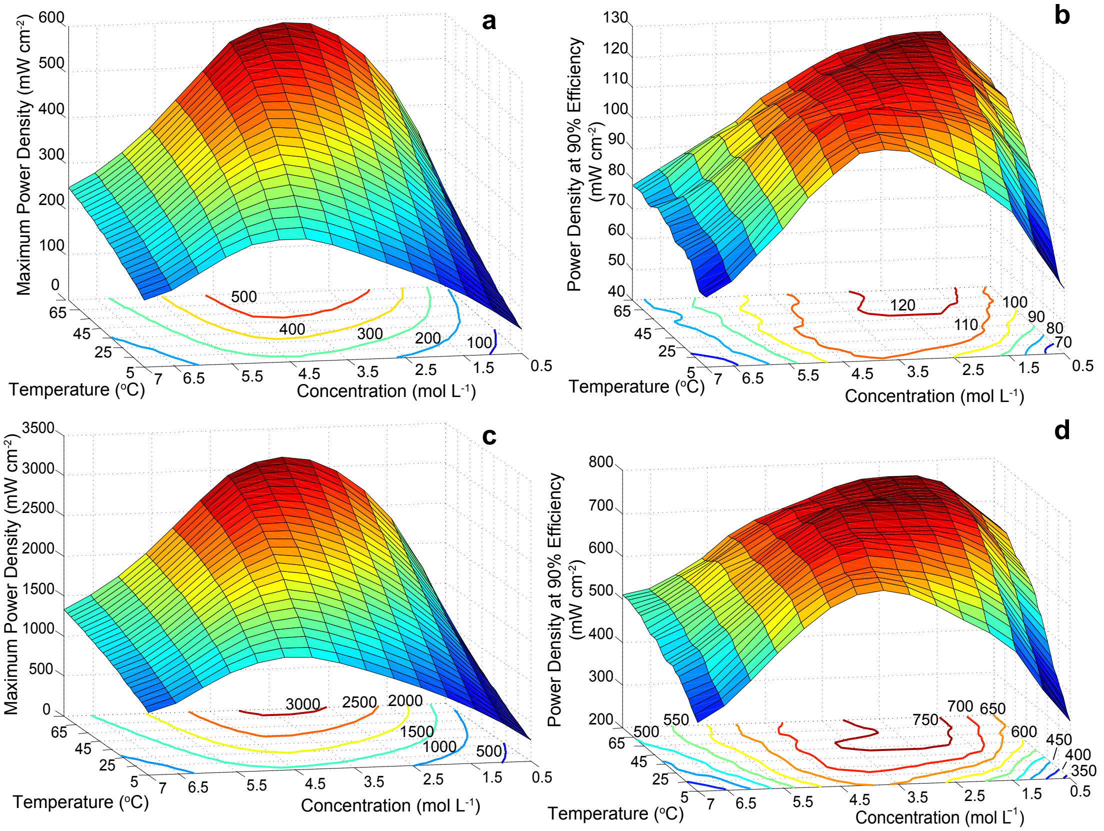

Figure 4.7. (**a**) Maximum power density vs. temperature and concentration for the Base Case, (**b**) Power density at 90% voltage efficiency vs. temperature and concentration for the Base Case, (**c**) Maximum power density vs. temperature and concentration for the More Optimal Case, and (**d**) Power density at 90% voltage efficiency vs. temperature and concentration for the More Optimal Case. These were calculated using the Base Case EPs for (a) and (b): H_2 electrode exchange current density i_0^H = 250 mA cm^{-2}, Br_2 electrode exchange current density i_0^{Br} = 40 mA cm^{-2}, membrane thickness $l = 125$ μm, diffusion layer thickness $\varepsilon = 125$ μm, H_2 gas pressure p_{H_2} = 1 atm and More Optimal Case EPs for (c) and (d): H_2 electrode exchange current density i_0^H = 600 mA cm^{-2}, Br_2 electrode exchange current density i_0^{Br} = 400 mA cm^{-2}, membrane thickness $l = 25$ μm, diffusion layer thickness $\varepsilon = 25$ μm, H_2 gas pressure p_{H_2} = 5 atm. Contour lines are projected onto the temperature-concentration plane. The “jaggedness” in (b) and (d) is due to computational mesh-size limitations and is not a real effect.

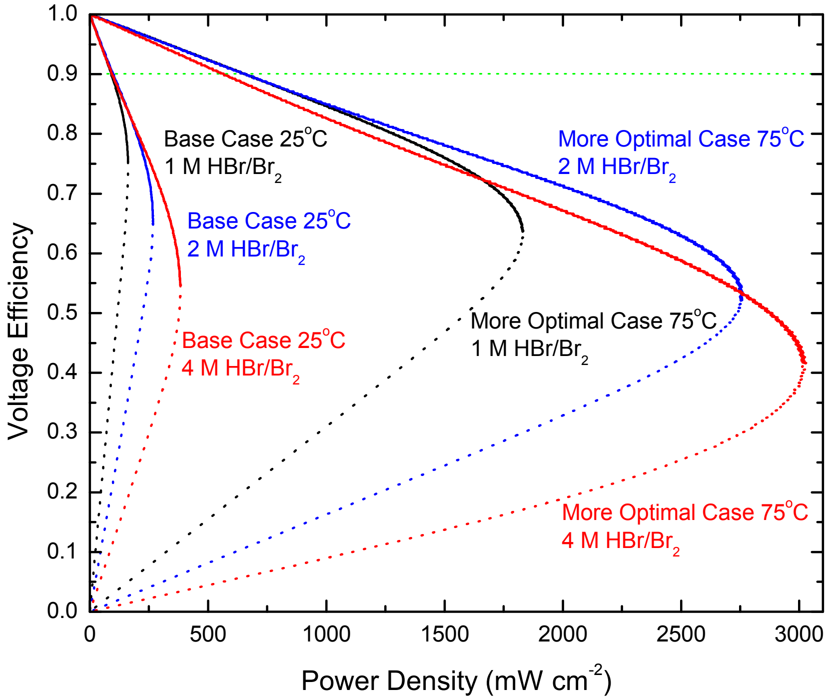

Figure 4.8. Voltage efficiency vs. power density under a variety of operating conditions for both the Base Case and the More Optimal Case. The dotted portions of the curves indicate regions of undesirable operation, as the efficiency decreases with decreasing power density. The green line indicates 90% voltage efficiency.

the highest power density.

In Figure 4.9, we report the variation of the maximum peak power density (the height of the highest point in Figure 4.7) as each of the engineering parameters (other than the hydrogen exchange current density, which is fixed at $i_0^H = 250$ mA cm^{-2}) is varied away from the Base Case while keeping the other four EPs fixed. Because higher temperatures always lead to higher cell efficiencies, the black (upper) dots were calculated at 75 °C, and the red (lower) ones at 5 °C. The black dots represent operation of the cell at 75 °C and the HBr/Br$_2$ concentration that results in the highest peak power density. The red (lower) dots represent operation at 5 °C and the HBr/Br$_2$ concentration that results in the lowest peak power density. In Figure 4.9a we varied i_0^{Br} from the certainly attainable value of 1 mA cm^{-2}, to the likely unattainable value of 1000 mA cm^{-2}. For this set of EPs, there are significantly diminishing returns for efforts to increase i_0^{Br} beyond about 100 mA cm^{-2}, but decreasing i_0^{Br} below the Base Case causes a substantial degradation in performance.

In Figure 4.9b we show how performance increases with decreasing membrane thickness, due to decreasing membrane resistance. Nafion is currently commercially available in thicknesses from 25 to 250 μm. In Figure 4.9c we show that the power performance declines considerably for large values of the diffusion layer thickness ε; this occurs because of small limiting current densities. Engineering a cell with as low a value of ε as possible is critical to achieving a high power density. Lastly, in Figure 4.9d, we show how the cell performance depends on the pressure of H$_2$ gas. Higher pressure gives a modest boost to the open circuit potential, but the gains to the maximum power density are minimal. Thus, it is apparent that increasing the H$_2$ pressure only has a modest effect on the cell performance.

While Figure 4.9 focuses on the effects on the peak power density of varying the individual

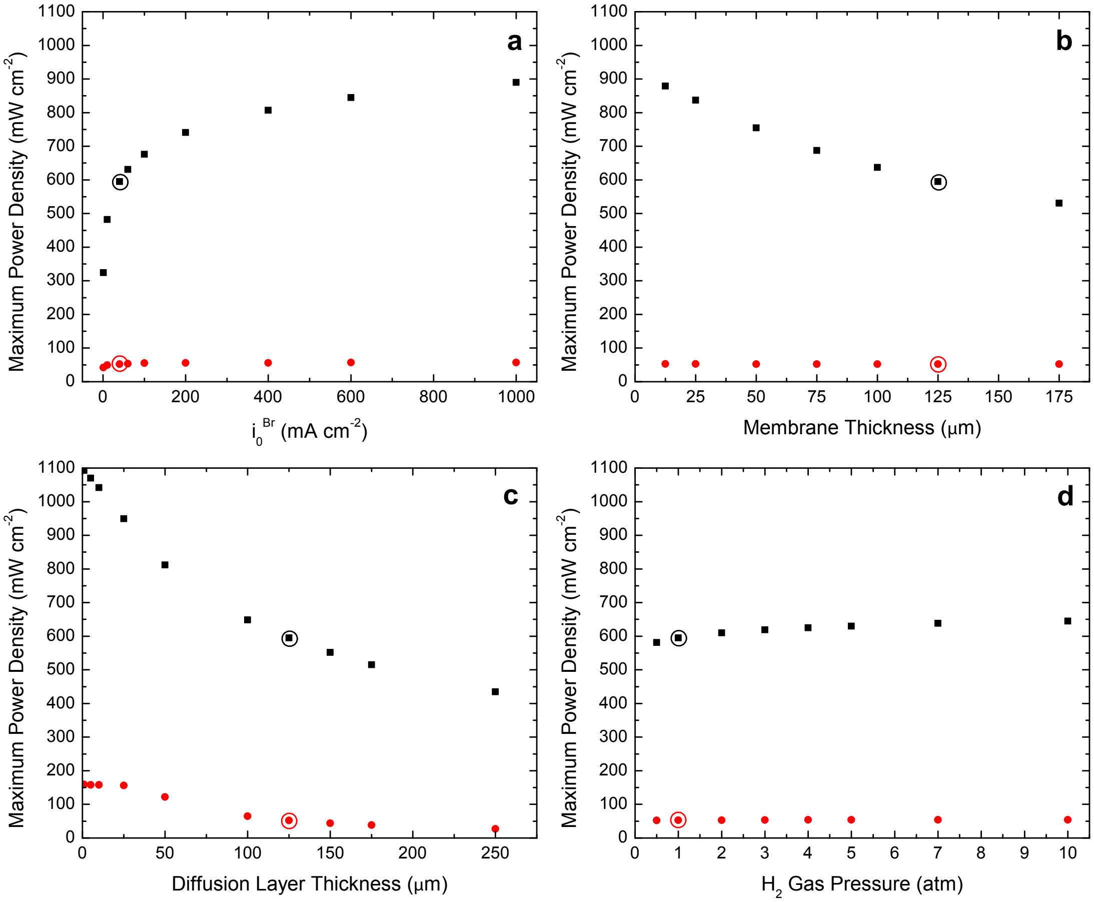

Figure 4.9. Dependence of performance on deviation from the Base Case engineering parameters. Maximum power densities are displayed as a function of each engineering parameter with the others held at their base values: H_2 electrode exchange current density $i_0^H = 250$ mA cm^{-2}, Br_2 electrode exchange current density $i_0^{Br} = 40$ mA cm^{-2}, membrane thickness $l = 125$ μm, diffusion layer thickness $\varepsilon = 125$ μm, H_2 gas pressure $p_{H_2} = 1$ atm. In (**a**) i_0^{Br} is varied, in (**b**) l is varied, in (**c**) ε is varied, and in (**d**) H_2 pressure is varied. The Base Case is circled in each plot. The black (upper) dots represent operation of the cell at 75 °C and the HBr/Br_2 concentration that results in the highest peak power density. The red (lower) dots represent operation at 5 °C and the HBr/Br_2 concentration that results in the lowest peak power density. The pairs of dots effectively bracket the expected cell performance over the entire range of temperatures and HBr/Br_2 concentrations explored in this study.

EPs, it is also important to understand how the cell power density at high efficiency varies with the EPs. The variations are not necessarily similar because different contributions dominate the loss at peak power and at high efficiency. From Figure 4.5, it is clear that the dominant loss at 90% galvanic efficiency is the bromine activation overpotential. Thus, varying the bromine electrode exchange current density should have the largest effect on cell performance at 90% efficiency. Figure 4.10a confirms this expectation. Figures 4.10b, 4.10c, and 4.10d show that the Nafion thickness, diffusion layer thickness, and H_2 pressure are much less critical to cells operating at high efficiencies: gains here only have a modest effect on cell performance.

Comparing the model to recent experimental results

Finally, we compare the model results to a recently published experimental report that is sufficiently detailed that a comparison is possible. Kreutzer *et al.* (2012) report on hydrogen-bromine cells that use a commercial electrode with a Pt loading of about 0.55 mg cm^{-2} for the bromine electrode [79]. In Figure 4.11, a fit of our model to a temperature series they collected is shown. Both potential vs. current density and power density vs. current density fits and data from Kreutzer *et al.* are included. The model curves at three different temperatures are shown as solid lines, and the data from Kreutzer *et al.* are indicated using markers (hollow circles for 23 °C, hollow triangles for 35 °C, and hollow squares for 45 °C). The data that are fit were collected at 23 °C, 35 °C, and 45 °C using a 2 M HBr/Br_2 electrolyte, 1.204 atm H_2 pressure (equivalent to 3 psig), and Nafion 212 (50 μm thick). The exchange current density for the Br_2 electrode used is calculated based on experimental results provided in the paper. They measured a Br_2/Br^- exchange current density of 0.3 mA cm^{-2} on flat Pt, and, because the structured electrodes used in the cell have reported surface area enhancement factors of about 556-667 cm^2

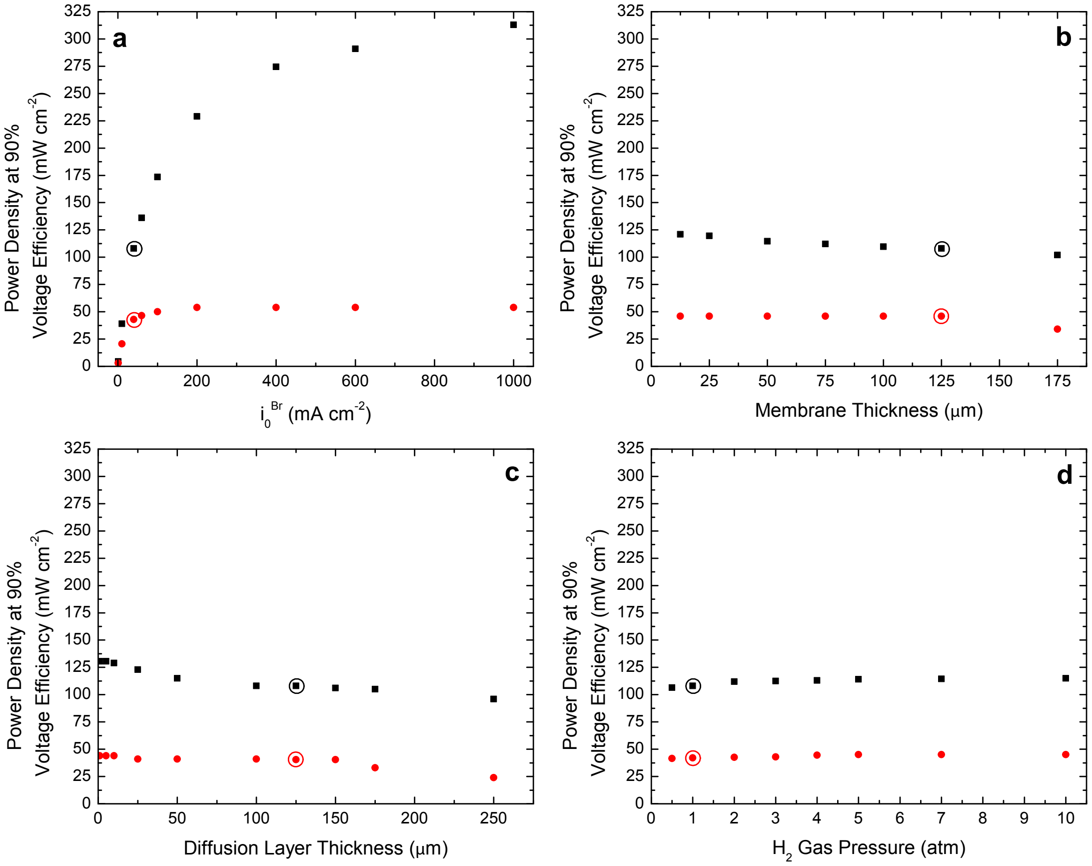

Figure 4.10. Dependence of performance on deviation from the Base Case engineering parameters. Power density at 90% voltage efficiency is displayed as a function of each engineering parameter with the others held at their base values: H_2 electrode exchange current density $i_0^H = 250$ mA cm^{-2}, Br_2 electrode exchange current density $i_0^{Br} = 40$ mA cm^{-2}, membrane thickness $l = 125$ μm, diffusion layer thickness $\varepsilon = 125$ μm, H_2 gas pressure $p_{H_2} = 1$ atm. In **(a)** i_0^{Br} is varied, in **(b)** l is varied, in **(c)** ε is varied, and in **(d)** H_2 pressure is varied. The Base Case is circled in each plot. The black (upper) dots represent operation of the cell at 75 °C and the HBr/Br_2 concentration that results in the highest peak power density. The red (lower) dots represent operation at 5 °C and the HBr/Br_2 concentration that results in the lowest peak power density. The pairs of dots effectively bracket the expected cell performance over the entire range of temperatures and HBr/Br_2 concentrations explored in this study.

of Pt per cm^2 of electrode, this corresponds to an exchange current density for the electrode of 167-200 mA cm^{-2}. A value of 183.5 mA cm^{-2} – the middle of this range – is used for model fitting purposes, and a value of 600 mA cm^{-2} is used for the hydrogen electrode exchange current density. With these EPs held constant, the only free parameter left to fit is the diffusion layer thickness ε. The best fit value for the 45°C curve is 116 μm, slightly under the Base Case value of 125 μm. The model fit is best when ε is permitted to vary, but, in practice, ε should be independent of temperature. Therefore, we use the value of 116 μm for all three curves, which we believe represents a more realistic fitting scenario. This does explain, though, why the fit is better at high current densities for the 45 °C data than either of the other two datasets. It appears that the model overestimates the effect of temperature on mass transport. Mathematically, the temperature dependence is encapsulated in Equations 4.25 and 4.26, which describe the species diffusivity and viscosity of water, respectively. Having experimental data for the diffusivities of Br_2 and HBr in aqueous mixtures of Br_2 and HBr and data for the viscosities of these solutions at a variety of compositions and temperatures would likely correct this overestimation, as they would account for the various complexing reactions (i.e. formation of Br_3^- and Br_5^-) and species interactions that naturally occur. Despite this, the quality of the fits is reasonable, working particularly well at low overpotentials and in electrolytic mode.

4.3 CONCLUSIONS

We developed a model for a PEM-based regenerative hydrogen-bromine fuel cell (rHBFC) including four voltage loss mechanisms: hydrogen electrode activation, bromine electrode activation, bromine electrode mass transport, and ohmic loss through the membrane. We

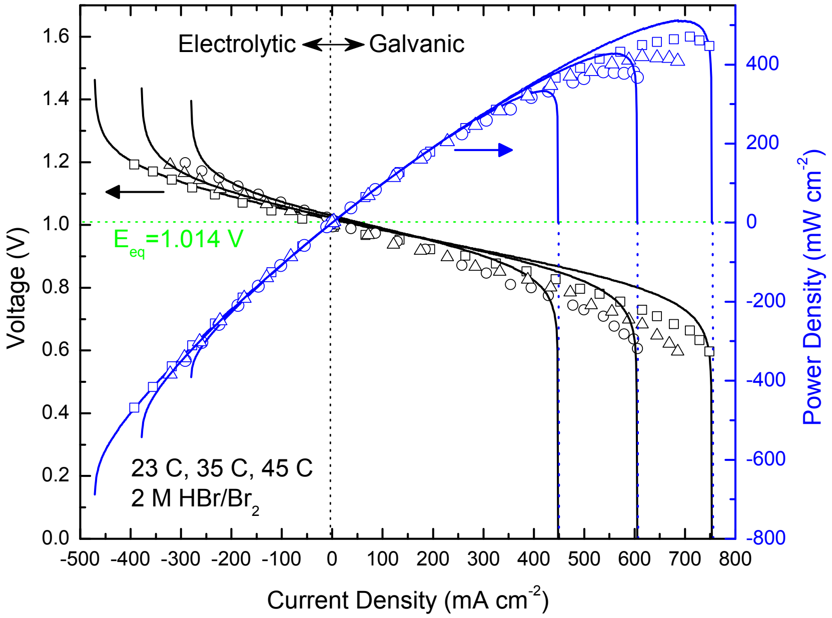

Figure 4.11. Comparison of model fits to data from Kreutzer *et al.* collected at 23 °C, 35 °C, and 45 °C using a 2 M HBr/Br_2 electrolyte. Model fits are shown using solid lines and data from Kreutzer *et al.* are indicated with markers (hollow circles for 23 °C, hollow triangles for 35 °C, and hollow squares for 45 °C). Values for the engineering parameters used in the model fits are the following: i_0^H = 600 mA cm^{-2}, i_0^{Br} = 183.5 mA cm^{-2}, membrane thickness l = 50 μm, H_2 gas pressure p_{H_2} = 1.2 atm, diffusion layer thickness ε = 116 μm. The only adjustable parameter was ε.

explored a large parameter space by looking at the dependences of each of these losses as a function of two “operating parameters”, acid concentration and temperature; and five “engineering parameters”, exchange current densities at both electrodes, membrane thickness, diffusion layer thickness, and hydrogen pressure. The model compares well with a recent experimental report of the behavior of a PEM-based hydrogen-bromine cell, particularly in the low current density regime and for electrolytic operation. We project that, with further R&D, a cell of this design could be developed that operates at greater than 90% voltage efficiency at current densities $>$700 mA cm^{-2} in both electrolytic and galvanic modes. The maximum power density for a “Base Case” cell is 530 mW cm^{-2} under the best operating conditions, and, for a “More Optimal Case” cell, 2760 mW cm^{-2}. Raising the operating temperature always improves the voltage efficiency, as all the losses explored here are made smaller by increasing the temperature. At 75 $^\circ$C, the membrane conductivity vs. HBr concentration peaks near 2 M. As the temperature is lowered, the conductivity peaks at progressively higher acid concentrations. For a high galvanic power density at 90% voltage efficiency, the only critical engineering parameter is i_0^{Br}: all other EPs have a weak effect on high efficiency operation. For a high peak power density, the most important engineering parameter is the diffusion layer thickness ε. Thus, it is critical for high power density cells that the mass transport behavior be optimized. For values of i_0^{Br} above about 100 mA cm^{-2}, diminishing returns are met in terms of increasing the maximum power density. However, if i_0^{Br} is too small, the maximum power density is severely reduced.

4.4 LIST OF SYMBOLS

A	Arrhenius pre-exponential factor, Ω^{-1}cm^{-1}

$a_{\mathrm{Br_2}}$	activity of aqueous bromine
$a_{\mathrm{H_2}}$	activity of hydrogen gas
$a_{\mathrm{HBr(aq)}}$	activity of hydrobromic acid
$c_{\mathrm{Br_2}}$	concentration of bromine, mol L^{-1}
c_{HBr}	concentration of hydrobromic acid, mol L^{-1}
C_O^{bulk}	bulk concentration of oxidized form (Br_2), mol cm^{-3}
C_O^S	concentration of oxidized form (Br_2) near the electrode surface, mol cm^{-3}
C_R^{bulk}	bulk concentration of reduced form (Br^-), mol cm^{-3}
C_R^S	concentration of reduced form (Br^-) near the electrode surface, mol cm^{-3}
D	diffusion coefficient, $\mathrm{cm}^2\ \mathrm{s}^{-1}$
$D_{\mathrm{Br^-}}$	diffusion coefficient of Br^-, $\mathrm{cm}^2\ \mathrm{s}^{-1}$
$D_{\mathrm{Br_2}}$	diffusion coefficient of Br_2, $\mathrm{cm}^2\ \mathrm{s}^{-1}$
E	cell potential, V
E_a	Arrhenius activation energy, kcal mol^{-1}
E_0'	standard cell potential, V
E_{eq}	equilibrium potential, V
$E_{\mathrm{eq,ideal}}$	equilibrium potential, V
$E_{\mathrm{eq,Nernst}}$	equilibrium potential, V
$E_{\mathrm{eq,Yeo}}$	equilibrium potential, V
$f_{\mathrm{H_2}}$	fugacity of hydrogen gas, atm
i	cell current density, mA cm^{-2}
i_0^{Br}	bromine electrode exchange current density, mA cm^{-2}
i_0^H	hydrogen electrode exchange current density, mA cm^{-2}
J	diffusive flux of species, mol $\mathrm{cm}^{-2}\ \mathrm{s}^{-1}$
l	proton-exchange membrane thickness, μm
m	molality, mol kg^{-1}
M	molarity, mol L^{-1}
p	cell power density, mW cm^{-2}
$p_{\mathrm{H_2}}$	hydrogen gas partial pressure, atm
T	temperature, degrees Celsius
X	weight fraction of HBr in solution

Greek letters

α	transfer coefficient

γ_{Br_2}	activity coefficient of Br_2(aq)
γ_{HBr}	activity coefficient of HBr(aq)
γ_{H_2}	activity coefficient of H_2
ΔC	concentration gradient across diffusion layer, mol cm^{-3}
Δx	diffusion layer thickness, equivalent to ε, cm
ε	diffusion layer thickness, cm
η	cell efficiency
η_{Br}	total bromine electrode activation overpotential (including mass transport effects), V
η'_{Br}	concentration-independent bromine electrode activation overpotential, V
η_{H}	hydrogen electrode activation overpotential, V
η_{MT}	bromine electrode mass transport overpotential, V
η_{R}	resistive overpotential, V
μ	viscosity, mPa · s or cP
ν	kinematic viscosity, m^2 s^{-1}
ρ_{H_2O}	density of water, g L^{-1}
ρ_{HBr}	density of hydrobromic acid, g L^{-1}
σ	membrane conductivity, Ω^{-1}cm^{-1}
φ	variable from Yeo and Chin, V

Constants

A_ρ	ρ_{HBr} fit, 59.98
B_ρ	ρ_{HBr} fit, -0.1300
c_0	reference concentration, 1 M
C_ρ	ρ_{HBr} fit, 0.001061
D_ρ	ρ_{HBr} fit, -1.263
E_ρ	ρ_{HBr} fit, 0.02160
F	Faraday's constant, 96485 C mol^{-1}
F_ρ	ρ_{HBr} fit, -0.0001647
MW_{H_2O}	molecular weight of H_2O, 18.0153 g mol^{-1}
MW_{HBr}	molecular weight of HBr, 80.91 g mol^{-1}
n	number of moles of electrons transferred in reaction, 2
p_0	reference pressure, 1 atm
R	ideal gas constant, 8.314 J mol^{-1} K^{-1} or 0.0019859 kcal mol^{-1} K^{-1}

u_0	free stream fluid velocity, 0.1 m s^{-1}
V_1	molecular volume of solute (53.2 for Br_2, 27 for Br^-), cm^3 mol^{-1}
V_2	molecular volume of solvent (18.9 for H_2O), cm^3 mol^{-1}
x	distance downstream from beginning of boundary layer, 10 μm

5

Organic Chemistries in Flow Batteries and the Quinone Bromide Flow Battery

Small organic molecules represent a new frontier in energy storage, in that their use is relatively unexplored, yet their possibilities and advantages are very exciting. Organic molecules have the potential to be very inexpensive, there typically aren't materials/abundance limitations of any kind, and desirable properties can be built into "designer" molecules. However, the vast majority of organic molecules are unacceptable candidates for use in batteries for a variety of reasons: poor reaction kinetics, poor selectivity, expensive syntheses, and safety concerns/flammability issues. The first two are particularly acute problems.

Electrochemical oxidation of many compounds, such as methanol, ethanol, and formic acid, have been exhaustively studied [94–100], yet a variety of issues persist, with poor electrode kinetics being perhaps the most severe issue. Other small organic molecules, like methane or simple alkanes, suffer from the fact that C-H bond activation is only possible at relatively high temperatures [101], far outside the operating range of any aqueous system (operation in a solid-oxide fuel cell is possible, though; see Park *et al.* [101]). These cells also suffer from electrode degradation issues due to carbonaceous buildup.

On top of the issues with electrochemical oxidation of small organic molecules mentioned above, the reverse reactions (i.e. reducing CO_2 back to liquid fuels), are perhaps even more challenging. CO_2 reduction has been studied extensively [102–104], as the economical electrochemical reduction of CO_2 is arguably one of the greatest remaining challenges in electrochemistry. CO_2 reduction to formate and CO is relatively straightforward, but reducing these two products further to yield useful liquid fuels with acceptable selectivities has proven extremely challenging [103].

Because of the myriad issues discussed above, many small organic molecules have limited viability for use in a battery. The demands of C-H bond activation are often too much to overcome, and CO_2 reduction has proven enigmatic.

Despite these issues, there does exist at least one class of organic molecules capable of satisfying the requirements for use in a battery: quinones. A selection of quinones of interest is shown in Figure 5.1a. They adopt a framework where a ketone (containing a C=O bond) moiety appears an even number of times on an aromatic backbone. Other functional groups can be substituted for hydrogen atoms on the ring to tune various properties of the molecule: its solubility, redox potential, and stability, for example. Figure 5.1b shows the electrochemical reaction one type of quinone is capable of undergoing. It is a two-electron, two-proton process in aqueous solution [105, 106], which is true in general for quinones, and not just the one pictured (the pictured quinone is the molecule of interest for much of this chapter though: 9,10-anthraquinone-2,7-disulfonic acid, or AQDS for short). The reaction relies on the reversibility of transforming two carbonyl (C=O) oxygen atoms into hydroxy (C-OH) groups and going back again. This circumvents the C-H bond activation issue seen with many other small organic molecules. [i]

Another important advantage of quinones, besides their tunability and reversibility in aqueous solutions, is the potential low cost of quinones. The precursor molecule anthracene is abundant in crude petroleum and is already oxidized on large scale to anthraquinone. Sulfonated anthraquinones are used on an industrial scale in wood pulp processing for paper [110], and they can be readily synthesized from the commodity chemicals anthraquinone and oleum [111]. Based on this simple electrolyte preparation that requires no further product separation, we estimate chemical costs of \$21 kWh^{-1} for AQDS and \$6 kWh^{-1} for bromine [112] (see the end of the experimental methods section in this chapter for information on cost calculations). For comparison, this is a substantial cost improvement over vanadium flow batteries, which contain

---

[i] Even with this in mind, the reasons for quinones' reversibility and excellent redox kinetics in aqueous solutions are poorly understood. This is despite the fact that quinone reactions were discovered and their properties explored nearly a century ago here at Harvard [105, 107–109].

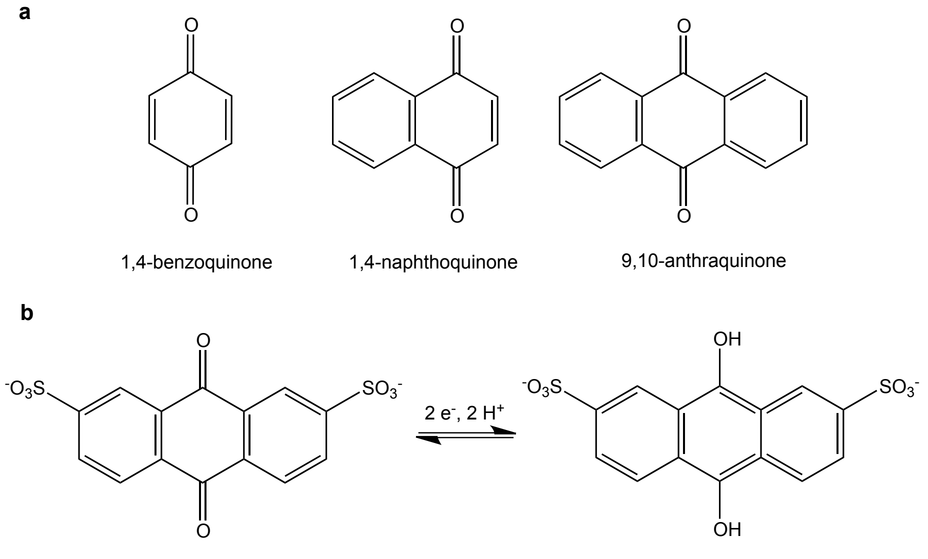

Redox reaction of 9,10-anthraquinone-2,7-disulfonic acid

Figure 5.1. (**a**) Chemical structures of 1,4-benzoquinone, 1,4-naphthoquinone, and 9,10-anthraquinone. The ability to replace H atoms at the various ring positions with any number of functional groups leads to a virtually limitless array of potential molecules that could be implemented in a battery. (**b**) the redox reaction of AQDS in aqueous solution. It is a two-electron, two-proton process.

redox-active materials that cost \$81 kWh^{-1} [113].

This chapter focuses on the use of quinone molecules in a flow battery. It begins by looking at the electrochemical properties of some of these molecules, highlighting their reversibility, fast kinetics, reasonable diffusivities, and high solubilities. After this, the chapter focuses on AQDS and its implementation in a well-functioning battery. The battery uses inexpensive carbon electrodes, combining the AQDS/$\mathrm{AQDSH_2}$ couple with the $\mathrm{Br_2/Br^-}$ redox couple, yielding a peak galvanic power density exceeding 0.6 W cm^{-2} at 1.3 A cm^{-2}. Cycling of the quinone-bromide flow battery (QBFB) showed 99.986% storage capacity retention per cycle over >100 cycles. The absence of active metal components in both redox chemistry and catalysis represents a significant shift away from modern batteries.

5.1 Experimental Methods

Half-cell measurements

Half-cell measurements were conducted using a BASi Epsilon EC potentiostat, a BASi Ag/AgCl aqueous reference electrode (RE-5B, 3M KCl filling solution), and a Pt wire counter electrode. Electrode potentials were converted to the standard hydrogen electrode (SHE) scale using E(SHE) = E(Ag/AgCl) + 0.210 V, where E(SHE) is the potential vs. SHE and E(Ag/AgCl) is the measured potential vs. Ag/AgCl. 2,7-Anthraquinone disulfonate disodium salt 98% was purchased from TCI and used as received. The electrolyte solution was sulfuric acid (ACS, Sigma) in DI-H2O (18.2 MΩcm, Millipore).

For the Pourbaix diagram, aqueous 1 mM solutions of AQDS disodium salt were prepared and pH buffered using the following chemicals: sulfuric acid (1 M, pH 0), $\mathrm{HSO_4^-/SO_4^{2-}}$ (0.1 M, pH

1–2), AcOH/AcO$^-$ (0.1 M, pH 2.65–5), $H_2PO_4^-/HPO_4^{2-}$ (0.1 M, pH 5.3-8), HPO_4^{2-}/PO_4^{3-} (0.1 M, pH 9.28-11.52), and KOH (0.1 M, pH 13). The pH of each solution was adjusted with 1 M H_2SO_4 or 0.1 M KOH solutions and measured with an Oakton pH 11 Series pH meter (Eutech Instruments). This work was done by Michael Gerhardt.

Rotating disk electrode (RDE) measurements were conducted by Dr. Michael Marshak using a BASi rotating disk electrode (RDE-2) and a 3 mm diameter glassy carbon disk electrode. All RDE data represent an average of three runs. Prior to each run, the glassy carbon disk working electrode was polished to a mirror shine with 0.05 µm alumina and rinsed with deionized water until a cyclic voltammogram of a solution of 1 mM AQDS in 1 M H_2SO_4 showed anodic and cathodic peak voltage separation of 34 to 35 mV at a sweep rate of 25 mV s^{-1}. The electrode was then rotated at 200, 300, 400, 500, 700, 900, 1200, 1600, 2000, 2500, and 3600 RPM while the voltage was linearly swept from 310 to 60 mV at 10 mV s^{-1}.

Hydrogen-quinone cell measurements

Early work on the use of quinones in a flow battery was done using a quinone on the positive side of the cell and hydrogen on the negative side. The cell components were identical to the fourth-generation hydrogen-chlorine cell described in Chapter 2 of this work, except a Nafion 211 (25 μm thick) membrane was used and commercial Pt/Ru-C electrodes were used on both sides of the cell. Serpentine flow channels were also used. The cell was operated in galvanic mode using previously described methods [11], with high-purity hydrogen gas flowed through the negative side of the cell near 5 psig and a 0.1 M p-benzoquinone solution in 1 N H_2SO_4 flowed through the positive side using a Cole Parmer Masterflex peristaltic pump. This reaction is spontaneous and drives electrons through an external load. Before each set of measurements, an

N_2 purge was performed to remove any remaining O_2 and to ensure there were no leaks in the assembly. A DC electronic load was used to draw incrementally higher currents from the cell, and, once the voltage stabilized (typically within a few seconds), its value was recorded. Each measurement was done three times at every current density, and the results were averaged. Results are only reported for galvanic operation, as performance in the electrolytic direction was extremely limited due to the low solubility of the reduced quinone molecules (arising from complexing issues discussed later in this chapter).

QBFB measurements

The QBFB comprised a mixture of commercially available and custom-made components, and is identical to the fifth-generation H_2-Cl_2 cell described in Chapter 2. Interdigitated flow fields were used. Pretreated 2 cm^2, stacked (6x) Toray carbon paper electrodes (each of which is about 7.5 μm uncompressed) were used on both sides of the cell. Pretreatment consisted of a 10 min. sonication in isopropyl alcohol followed by a five hour soak in a hot (50 °C) mixture of undiluted sulfuric and nitric acids in a 3:1 volumetric ratio. Nafion 212 (50 μm thick) was used as a proton-exchange membrane (PEM, Alfa Aesar), and PTFE gasketing was used to seal the cell assembly. Membrane pretreatment was done according to previously published protocols (see Chapter 2 in this work). On the positive side of the cell, 120 mL of 3 M HBr and 0.5 M Br_2 were used as the electrolyte solution in the fully discharged state; on the negative side, 1 M 2,7-AQDS in 1 M H_2SO_4 was used. HBr was used on the negative side instead of H_2SO_4 for stability testing results displayed in Figure 5.14. State-of-charge calculations are based on the composition of the quinone side of the cell. 2,7-Anthraquinone disulfonate disodium salt 98% (TCI) was flushed twice through a column containing Amberlyst®15H ion-exchange resin to remove the sodium ions, thereby forming the AQDS used in the battery. Measurements shown here were done at 40 °C. March ®centrifugal pumps were used to circulate the fluids at a rate of approximately 200 mL min^{-1}, except in the case of Figure 5.13, where a Cole-Palmer diaphragm pump was used on the AQDS side of the cell. This pump has a much smaller internal volume than the centrifugal pumps, thereby allowing for the use of a smaller volume of AQDS liquid, reducing the total capacity of the battery and accelerating the cycling experiment seen in Figure 5.13. For characterization, several instruments were used: a CHInstruments 1100C potentiostat (which can be used up to ± 2 A), a DC electronic load (Circuit Specialists, Inc.) for galvanic discharge, a DC regulated power supply (Circuit Specialists, Inc.) for electrolytic characterization, and a standard multimeter for independent voltage measurements. The cell was charged at 1.5 V until a fixed amount of charge ran through the cell. During this process, the AQDS electrolyte color changed from orange to dark green (AQDS to $\mathrm{AQDSH_2}$). Periodically, the open circuit potential was measured, providing the data in Figure 5.10b. Also, at various states of charge (SOCs), potential-current behavior was characterized using the equipment described above: a fixed current was drawn from the cell, and the voltage, once stabilized, was recorded (Figure 5.10). For the cycling data in Figure 5.12b, the potentiostat was used for constant current ($\pm$ 0.5 A cm^{-2}) measurements with cutoff voltages of 0 V and 1.5 V. The discharge capacity retention is calculated as the discharge time of cycle n divided by the discharge time of cycle $n - 1$. For the cycling data in Figure 5.12a, a more dilute quinone solution (0.1 M as opposed to 1 M) was utilized. Here, the half-cycle lengths were programmed to run at constant current for a fixed amount of time, provided the voltage cutoffs were not reached, so that half of the capacity of the battery was utilized in each cycle. The voltage cutoffs were never reached during charging, but were reached during discharge. Current efficiencies are evaluated by dividing the discharge time by the charge time of the previous half-cycle.

Cost and efficiency calculations

Cost calculations were done using the following formula:

$$C = (3.6 \cdot 10^3)\frac{PM}{nFE}, \tag{5.1}$$

where C is the cost of the compound ($\$\ \mathrm{kWh}^{-1}$), P is the cost per kilogram, M is the molecular/atomic mass of the compound, F is Faraday's constant (96485 $\mathrm{C\ mol}^{-1}$), n is the number of moles of electrons transferred per mole of storage compound (2 for the QBFB), and E is the open-circuit voltage (V) of the storage device. In calculating the price for the anthraquinone-bromine battery, a price of \$4.74 kg^{-1} (eBioChem) was used for anthraquinone.[ii] The price of bromine was \$1.76 kg^{-1}, based on estimates from the U.S. Geological Survey [112]. The cell voltage used to calculate costs here was 0.858 V. For vanadium, costs were calculated from USGS prices from 2011 of vanadium pentoxide at \$14.37 kg^{-1} [113], and the cell voltage used was 1.2 V.

The cell voltage efficiency is defined as it was in previous chapters (see Equation 2.1). The current efficiency is defined for the nth cycle in the following manner:

$$\text{current efficiency} = \frac{Q_{d,n}}{Q_{c,n}} \tag{5.2}$$

where $Q_{d,n}$ is the number of coulombs extracted from the discharge portion of cycle n and $Q_{c,n}$ is

---

[ii] Note that, in order to get the sulfonated form actually used here, anthraquinone must be reacted with oleum (H_2SO_4/SO_3), which adds a negligible cost at scale; this cost is not included here.

the number of coulombs extracted from the charge portion of cycle *n*. This number should be as close to 1 as possible. The discharge capacity retention is defined for the *n*th cycle using the following equation:

$$\text{discharge capacity retention} = \frac{Q_{d,n}}{Q_{d,n-1}} \tag{5.3}$$

where $Q_{d,n-1}$ is the number of coulombs extracted from the discharge portion of cycle $(n-1)$.

5.2 HALF-CELL MEASUREMENTS

In order to gain a better understanding of the quinone redox reaction on carbon, AQDS was subjected to half-cell electrochemical measurements. Cyclic voltammetry of a 1 mM solution of AQDS in 1 M sulfuric acid on a glassy carbon disk working electrode shows current peaks corresponding to reduction (lower peak) and oxidation (upper peak) of the anthraquinone species (Figure 5.2). It exhibits a peak separation near 40 mV, which is close to the 59 mV/n, where n is the number of electrons involved, expected for a two-electron process (any number less than 59 mV is a good indicator of a multi-electron process). Also note that E_0, the potential halfway between the reduction and oxidation peaks, is 0.221 V.

Using appropriately pH-buffered solutions, one can measure E_0 for AQDS at a variety of different solution pH values to generate a so-called "Pourbaix diagram." These diagrams are often useful in understanding the corrosion properties of materials in aqueous solutions[iii], but they are helpful here in that they allow for confirmation of the number of protons and electrons involved in the redox reaction of AQDS. As is evident in Figure 5.3, a two-electron, two-proton process

---

[iii] Ref. [114], written by Marcel Pourbaix, has a remarkable amount of information and is a must-own for any electrochemist.

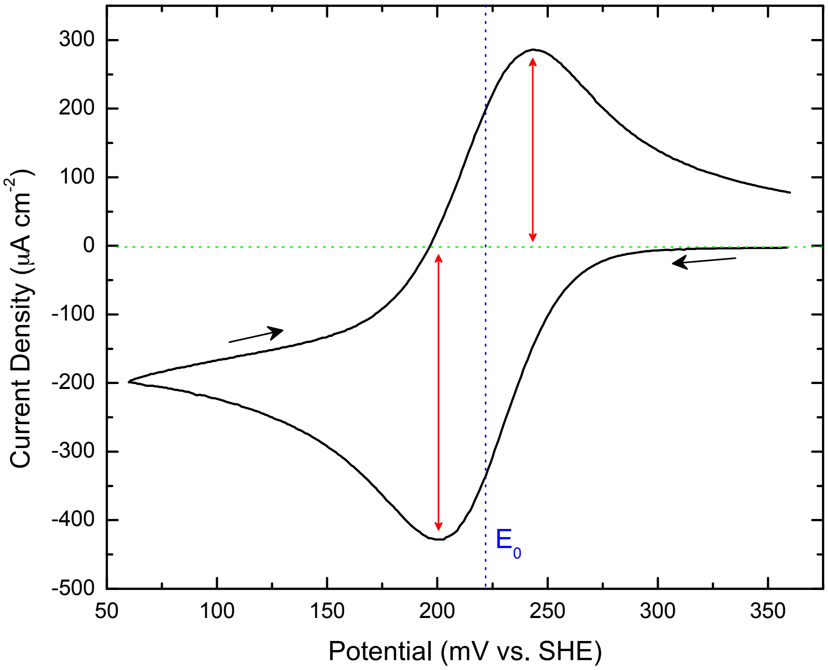

Figure 5.2. Cyclic voltammogram of 1 mM AQDS in 1 M H_2SO_4 on a glassy carbon working electrode. The blue vertical line indicates the position of E_0, halfway between the reduction and oxidation peaks (indicated by the red lines).

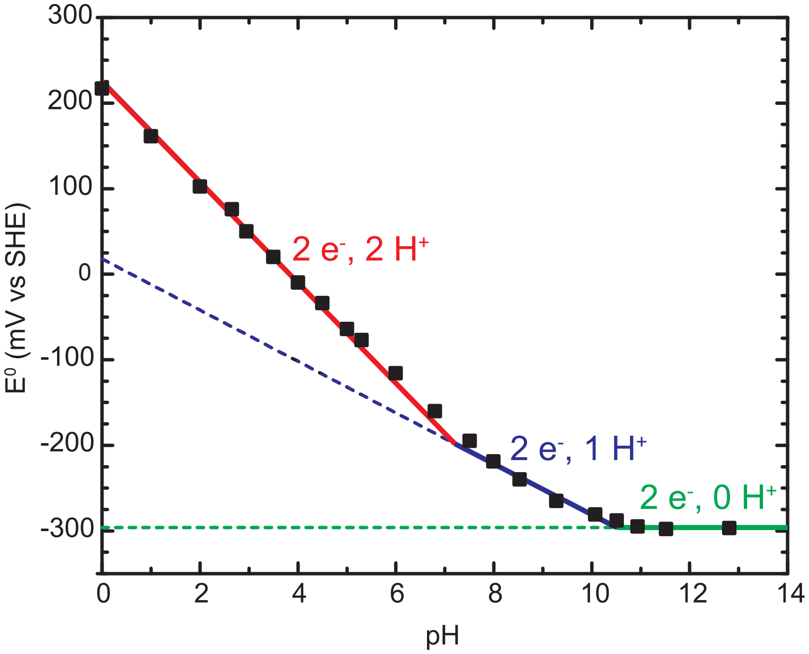

Figure 5.3. Pourbaix diagram (E_0 vs. pH) for AQDS. Data are fit to three solid lines indicating slopes of -59 mV pH^{-1} (red), -30 mV pH^{-1} (blue) and 0 mV pH^{-1} (green), corresponding to two-, one- and zero-proton processes, respectively. The dashed lines linearly extrapolate the one- and zero-proton processes to give E_0 values of 18 mV ($2\ e^{-}$, $1\ H^{+}$) and −296 mV ($2\ e^{-}$, $0\ H^{+}$). Data collected by Michael Gerhardt.

occurs below a pH of about 7, with the measured data points closely following the red line, which has a slope of -59 mV pH^{-1}. In the pH 7-10.5 range, AQDS undergoes a two-electron, one-proton electrochemical reaction, closely following the blue line (slope of -30 mV pH^{-1}). Above pH 10.5, AQDS undergoes a two-electron, zero-proton process, indicating by the horizontal green line. The entirety of the data included in this chapter from this point forward was collected in the low pH (i.e. the two-proton, two-electron) regime.

An important set of methods for making electrochemical measurements involve the use of a rotating disk electrode (RDE). By spinning an electrode with a known geometry at a known rate, the convective-diffusive equation can be solved exactly (see Chapter 9 in Ref. [115] for more details). These forced convection measurements allow for the precise separation of kinetic effects at an electrode and mass transport effects around the electrode, and they allow for the measurement of rate constants, diffusion coefficients, and transfer coefficients, all important electrochemical parameters. From a solution to the convective-diffusive equation, the Levich equation is found:

$$i_l = 0.62nFAD^{\frac{2}{3}}\omega^{\frac{1}{2}}\nu^{-\frac{1}{6}}C_O, \tag{5.4}$$

where i_l is the mass-transport-limited current in A cm^{-2}, n and F are defined as in previous chapters (see section 4.4), A is the electrode area in cm^2, D is the diffusion coefficient in cm^2 s^{-1}, ω is the rotation rate in rad s^{-1}, ν is the kinematic viscosity in cm^2 s^{-1}, and C_O is the concentration of AQDS in mol cm^{-3}. By collecting RDE data at a variety of rotation rates and measuring i_l at each rate, a plot of i_l vs. $\omega^{1/2}$ should yield a straight line with slope $0.62nFAD^{\frac{2}{3}}\nu^{-\frac{1}{6}}C_O$. Figure 5.4a shows the raw RDE data for 1mM AQDS in 1 M H_2SO_4 on a glassy carbon disk electrode, collected at eleven different rotation rates, and Figure 5.4b shows this same data on a plot of i_l vs. $\omega^{1/2}$, with a fit to Equation 5.4 superimposed. This fit yields an AQDS diffusion coefficient D = 3.8 x 10^{-6} cm^2 s^{-1}. For comparison, the diffusion coefficient for Br_2 at 25 °C is 1.42 x 10^{-5} cm^2 s^{-1} [14].

Another important equation in electrochemical analysis is the Koutecký-Levich equation, which takes the following form:

$$\frac{1}{i} = \frac{1}{i_K} + \frac{1}{i_l} = \frac{1}{i_K} + \frac{1}{0.62nFAD^{\frac{2}{3}}\omega^{\frac{1}{2}}\nu^{-\frac{1}{6}}C_O}, \tag{5.5}$$

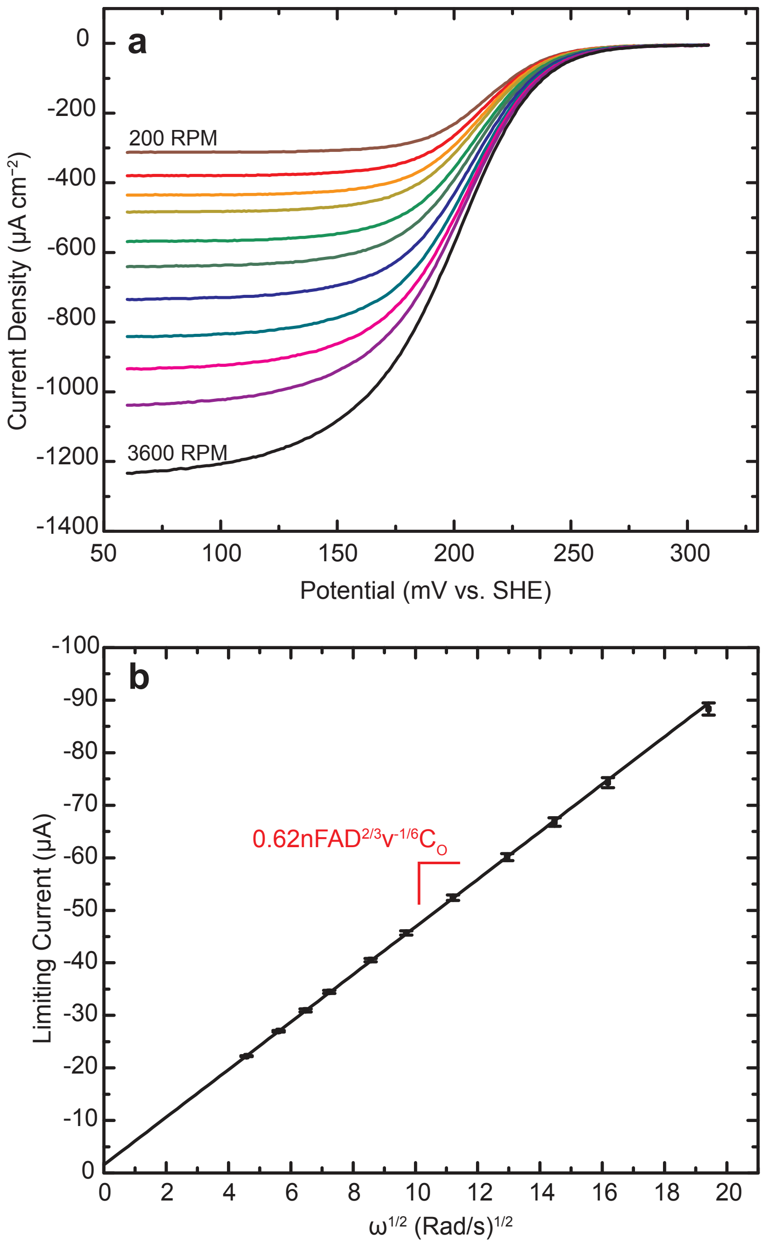

Figure 5.4. (**a**) Rotating disk electrode (RDE) measurements of AQDS using a glassy carbon electrode in 1 M H_2SO_4 at 11 rotation rates: 200, 300, 400, 500, 700, 900, 1200, 1600, 2000, 2500, and 3600 RPM. (**b**) Levich plot (limiting current versus square root of rotation rate ω) of 1 mM AQDS in 1 M H_2SO_4 (the fitted line has a slope of 4.53 μA $s^{1/2}$ $rad^{-1/2}$, giving $D = 3.8 \times 10^{-6}$ cm^2 s^{-1}). Data are an average of three runs; error bars indicate the standard deviation. Data collected by Michael Marshak.

where i is the measured current in A cm^{-2}, i_K is the kinetic current, or the current in the absence of any mass-transfer effects (i.e. infinitely fast transport), in A cm^{-2}, and all of the other terms are defined in Equation 5.4. One can then take the data in Figure 5.4a, and, for a given potential, note the measured current as a function of rotation rate (i.e. draw a vertical line through the curves and determine the points where the individual curves cross this vertical line). If these points are then placed on a plot of $\frac{1}{i}$ vs. $\frac{1}{\omega^{1/2}}$, a straight line should arise with y-intercept $\frac{1}{i_K}$ and slope $\frac{1}{0.62nFAD^{2/3}\nu^{-1/6}C_O}$. This can be done at a variety of potentials and produces the Koutecký-Levich plot seen in Figure 5.5a. These lines should be parallel but have different y-intercepts, which intuitively makes sense since one would expect a larger i_K for larger overpotentials. In Figure 5.5a, Koutecký-Levich lines for six different overpotentials (13, 18, 23, 28, 33, and 38 mV) are shown.

One can take the values for i_K found in Figure 5.5a and plot overpotential vs. $\log(i_K)$ to yield the plot seen in Figure 5.5b. Six data points are shown here, corresponding to the lines seen in Figure 5.5a. A fit to these points can be drawn using the Butler-Volmer equation:

$$i = i_0 \left[\frac{C_O^s(i)}{C_O^{bulk}} \exp\left(\frac{-\alpha nF\eta}{RT}\right) - \frac{C_R^s(i)}{C_R^{bulk}} \exp\left(\frac{(1-\alpha)nF\eta}{RT}\right) \right], \tag{5.6}$$

where i_0 is the exchange current density (in mA cm^{-2}), C_O^{bulk} and C_R^{bulk} are the bulk concentrations of the oxidized and reduced forms, respectively, $C_O^s(i)$ and $C_R^s(i)$ are their respective concentrations near the electrode surface (all in mol cm^{-3}). In the regime where mass-transport is practically infinite, which is the case when calculating i_K, C_R^s is effectively zero, as any reduced quinone is immediately transported away from the electrode. Thus, the second exponential term in Equation 5.6 can be neglected. Furthermore, $C_O^s = C_O^{bulk}$ by this mass transport assumption, leading to a simplified form of the Butler-Volmer equation:

$$i = i_0 \left[\exp\left(\frac{-\alpha n F \eta}{RT} \right) \right] \tag{5.7}$$

which can be written in the following form by taking the natural log of both sides, solving for η, and converting ln to log:

$$\eta = \frac{2.303RT}{\alpha nF} \log i_0 - \frac{2.303RT}{\alpha nF} \log i. \tag{5.8}$$

Thus, a plot of overpotential vs. log(i) will yield a straight line with a slope of $\frac{2.303RT}{\alpha nF}$ and an x-intercept equal to log(i_0), as can be seen in Figure 5.5b. From this fit, values of α=0.474 and i_0= 0.7 mA cm^{-2} were found. The value of α is close to the value of 0.5 expected for an ideally reversible reaction. Using the following equation, i_0, which is a concentration-dependent exchange current density, can be converted to a more generally applicable rate constant:

$$k_0 = \frac{i_0}{FAC_O}, \tag{5.9}$$

so the value k_0 = 7.2 x 10^{-3} cm s^{-1} is found. For comparison, this rate constant is faster than that found for many other species used in flow batteries such as V^{3+}/V^{2+}, Br_2/Br^-, and Fe^{3+}/Fe^{2+}, which have rate constants of 4 x 10^{-3} cm s^{-1} (on Hg), 5.8 x 10^{-4} cm s^{-1} (on vitreous carbon), and 2.2 x 10^{-3} cm s^{-1} (on polycrystalline Au), respectively (see Table 2 in Ref. [116]). It implies that the voltage loss due to the rate of surface electrochemical reactions is negligible.

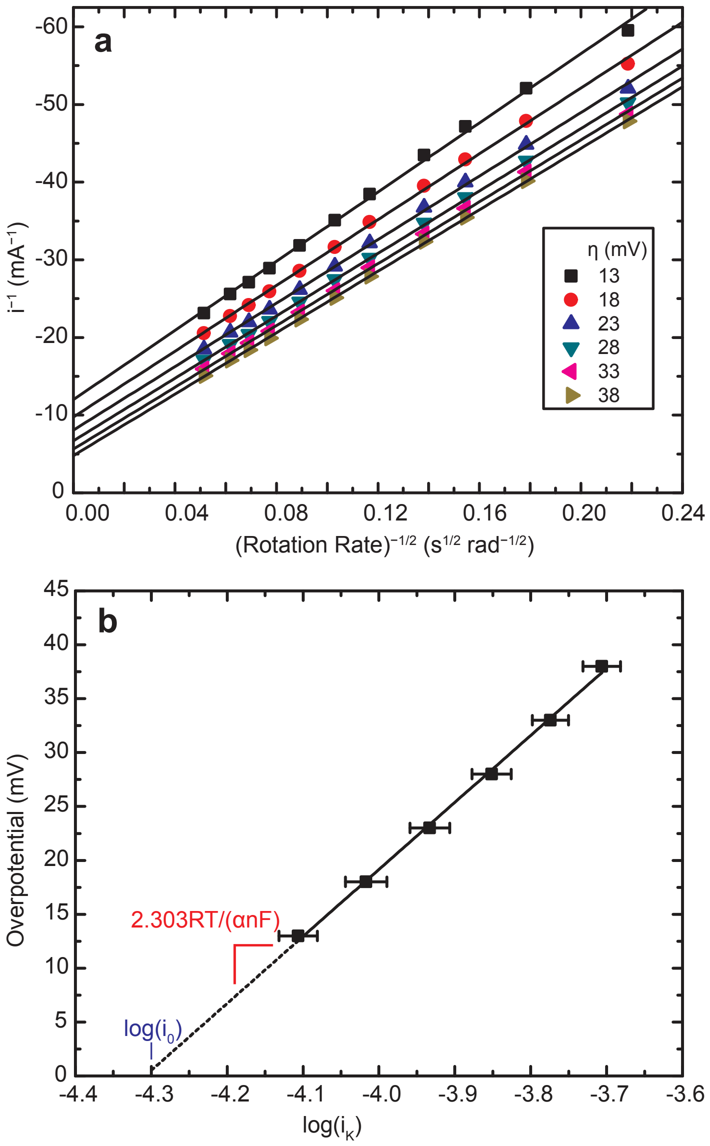

Figure 5.5. (**a**) Koutecký-Levich plot (current^{-1} versus rotation rate$^{-1/2}$) derived from Figure 5.4a at six different AQDS reduction overpotentials. (**b**) Fit of Butler-Volmer equation for AQDS, constructed using the current response in the absence of mass-transport at low AQDS reduction overpotentials; i_K is the current extrapolated from the zero-intercept of (a); the best-fit line yields $\alpha = 0.474$ and $k_0 = 7.2 \times 10^{-3}$ cm s^{-1}.

5.3 HYDROGEN-QUINONE CELL RESULTS

Our exploration of the use of quinones in batteries began with the implementation of several different benzoquinones on the positive side of the battery and H_2 on the negative side. This cell used a Nafion 211 membrane and a Pt/Ru-C electrode on the H_2 side of the cell. Because the behavior of the hydrogen electrode is very well understood, arranging the cell in this manner allows us to "isolate" the performance of the quinone electrode and determine the viability of these organic molecules in a flow battery. Some preliminary results of these studies can be found in Refs. [117] and [118]. Initial studies were done on 1,4-parabenzoquinone, 2,5-dihydroxybenzenesulfonic acid (identical to the reduced form of 1,4-parabenzoquinone with an added sulfonyl group), and catechol-3,5-disulfonic acid (an orthobenzoquinone with 2 sulfonyl groups, also known as tiron). These molecules were first tried because they were very inexpensive. With the latter two molecules, which can be seen in Figure 5.6, cell performance was simply terrible. The equilibrium potentials were well below expected values (possibly due to complexing in solution and/or electrode fouling), and very little current could be drawn from the cell, so these molecules were abruptly abandoned. With the 1,4-parabenzoquinone, however, we achieved reasonable cell performance. Figure 5.7 highlights this fact.

Limiting current densities approaching 250 mA cm^{-2} were achieved, with power densities just under 50 mW cm^{-2}. The cell equilibrium potential is 0.685 V, extremely close to the expected literature value of 0.699 V [82]. One important note is that the flow rate begins affecting the cell performance at relatively small current densities (< 50 mA cm^{-2}), indicating that mass transport is extremely limiting in this cell. Thus, although the power densities are not particularly high, the

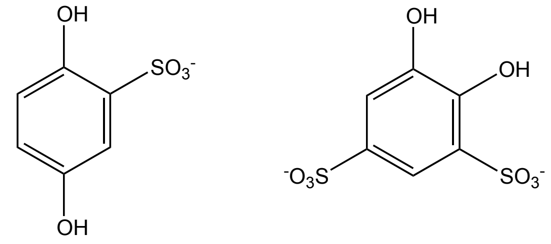

2,5-dihydroxybenzenesulfonic acid

catechol-3,5-disulfonic acid
(tiron)

Figure 5.6. Chemical structures of 2,5-dihydroxybenzenesulfonic acid and catechol-3,5-disulfonic acid (also known as tiron).

fact that mass transport limitations appear to be the dominant loss indicates that there is a lot of room for improvement in this particular cell, which was a promising result at the time. Even more importantly, this was the first experiment from our group that definitively proved that quinones were a viable molecule for use in a flow battery. Ultimately, 1,4-parabenzoquinone proved to be an unsuitable molecule for use in a battery due, we believe, to its propensity to complex with hydroquinone, its reduced counterpart, forming an insoluble compound called quinhydrone [119] that precipitates out of solution and ultimately clogs the cell (Figure 5.8). Quinhydrone is a resonance-stabilized compound where the hydrogen in the -OH groups on the hydroquinone is shared with the carbonyl oxygen atoms on the quinone (the rings also neatly stack on top of each other, like two sheets of paper, as opposed to the side-by-side arrangement shown in Figure 5.8). It is critical to keep in mind that the formation of these types of compounds is possible, as it is obviously an undesirable property. Fortunately, as more rings are added and more functional groups are appended to these rings, this type of reaction becomes less energetically favorable, thereby limiting reactions of this type. Anthraquinones, for example, do not appear to experience this problem, and so far no serious complexing issues have been observed in these larger quinones.

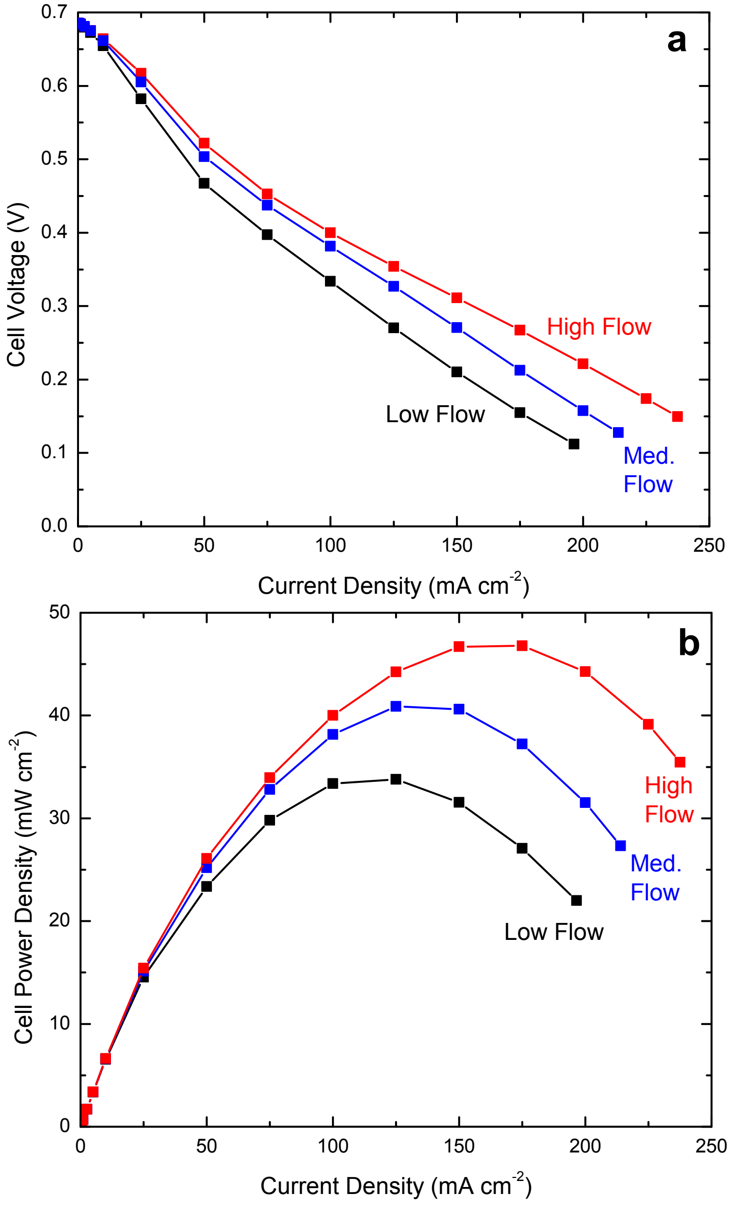

Figure 5.7. (**a**) Cell potential vs. current density for a hydrogen-quinone battery using 5 psig humidified H_2 on the negative side and 0.1 M 1,4-parabenzoquinone in 1 N H_2SO_4 on the positive side. Performance is indicated at three different quinone flow rates. (**b**) Cell power density vs. current density for the same cell.

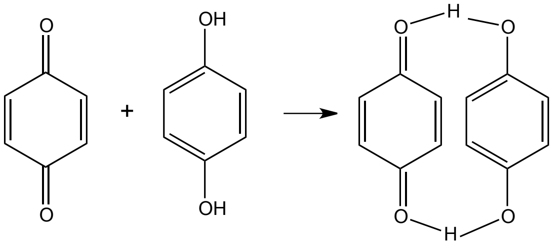

Figure 5.8. Quinydrone formation. When 1,4-parabenzoquinone is reduced to hydroquinone, the two form a complex called quinhydrone, where the hydrogens in the -OH groups on the hydroquinone are shared with the carbonyl oxygen atoms on the quinone, forming a stabilized resonance structure. Quinhydrone is a black, insoluble compound that precipitates out of solution and ultimately causes the cell to fail.

5.4 QBFB RESULTS

After concluding our initial studies of the hydrogen-quinone system, we began testing lower-potential quinones to place on the negative side of a battery against the Br_2/Br^- couple on the positive side. Ideally, a quinone with a redox potential between 0 and 0.2 V would be used. It should be as close to 0 V as possible while still ensuring that hydrogen evolution is minimized (below 0 V, hydrogen evolution is thermodynamically favorable). In general, $E_{0,\text{benzoquinone}} > E_{0,\text{naphthoquinone}} > E_{0,\text{anthraquinone}}$, meaning that anthraquinones are likely to be the most promising candidates for a low-potential quinone.

A schematic of the QBFB is shown in Figure 5.9. The positive side relies on the Br_2/Br^- couple and the negative side on the $AQDS/AQDSH_2$ couple. In Figure 5.10a, a plot of the cell potential vs. current density at five different states of charge (SOCs; measured with respect to the quinone side of the cell) is shown. The limiting current density in the galvanic direction was 1.3 A cm^{-2} in the 90% SOC case. As the SOC increased from 10% to 90%, the open circuit potential increased

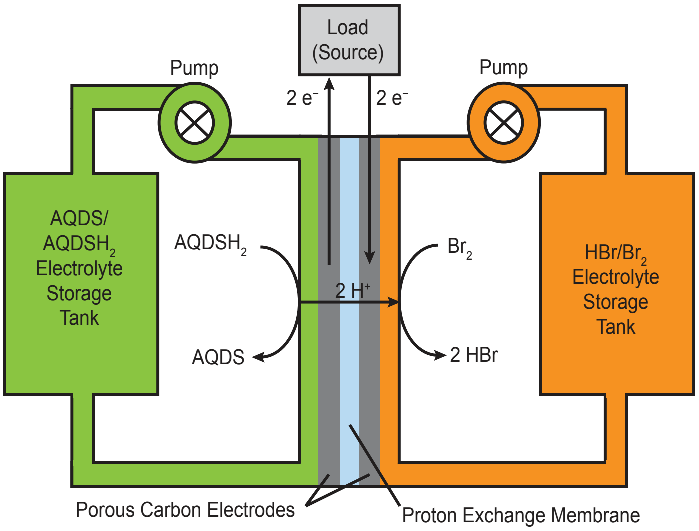

Figure 5.9. Cell schematic of the QBFB. Discharge mode is shown; the arrows are reversed for electrolytic/charge mode. $AQDSH_2$ refers to the reduced form of AQDS.

linearly from 0.69 V to 0.92 V, as is shown in Figure 5.10b.

Figure 5.11 shows the power density vs. current density for the cell at the same five SOCs shown in Figure 5.10a. In the galvanic direction, peak power densities were 0.246 W cm^2 and 0.600 W cm^2 at 10% SOC and 90% SOC, respectively (Figure 5.11a). Vanadium flow batteries took many years to reach the power density performance we have achieved here [120, 121]. Figure 5.11b shows the cell performance in the electrolytic direction. In order to avoid significant water splitting under these oxidizing conditions, we used a cut-off voltage of 1.5 V, at which point the current densities observed at 10% and 90% SOCs were -2.25 A cm^2 and -0.95 A cm^2, respectively, with corresponding power densities of -3.342 W cm^2 and -1.414 W cm^2.

In Figure 5.12 we report the results of initial cycling studies for this battery, to test for consistent performance over longer time scales. Figure 5.12a shows cycling data at $\pm$ 0.2 A cm^2

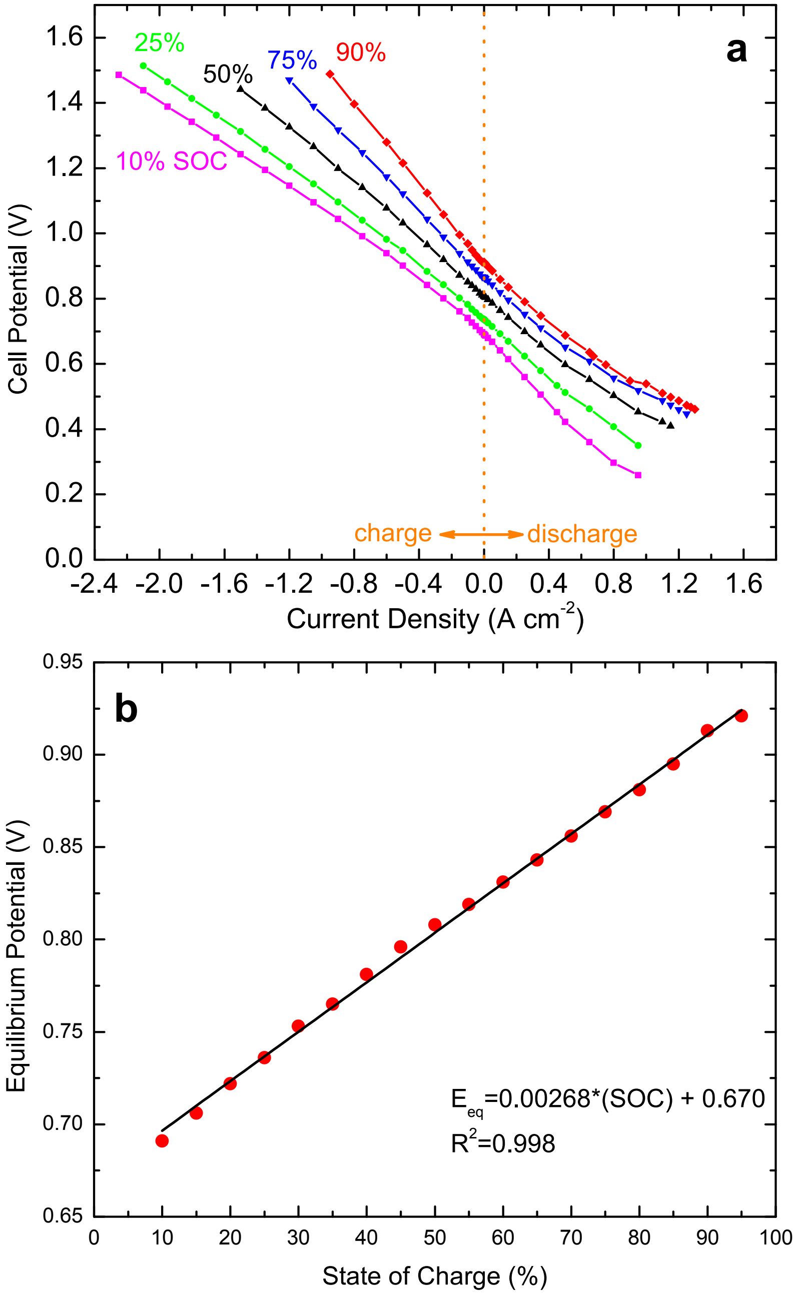

Figure 5.10. (**a**) Cell potential vs. current density at five different states-of-charge (SOCs) for the QBFB. (**b**) equilibrium potential vs. SOC with best-fit line superimposed.

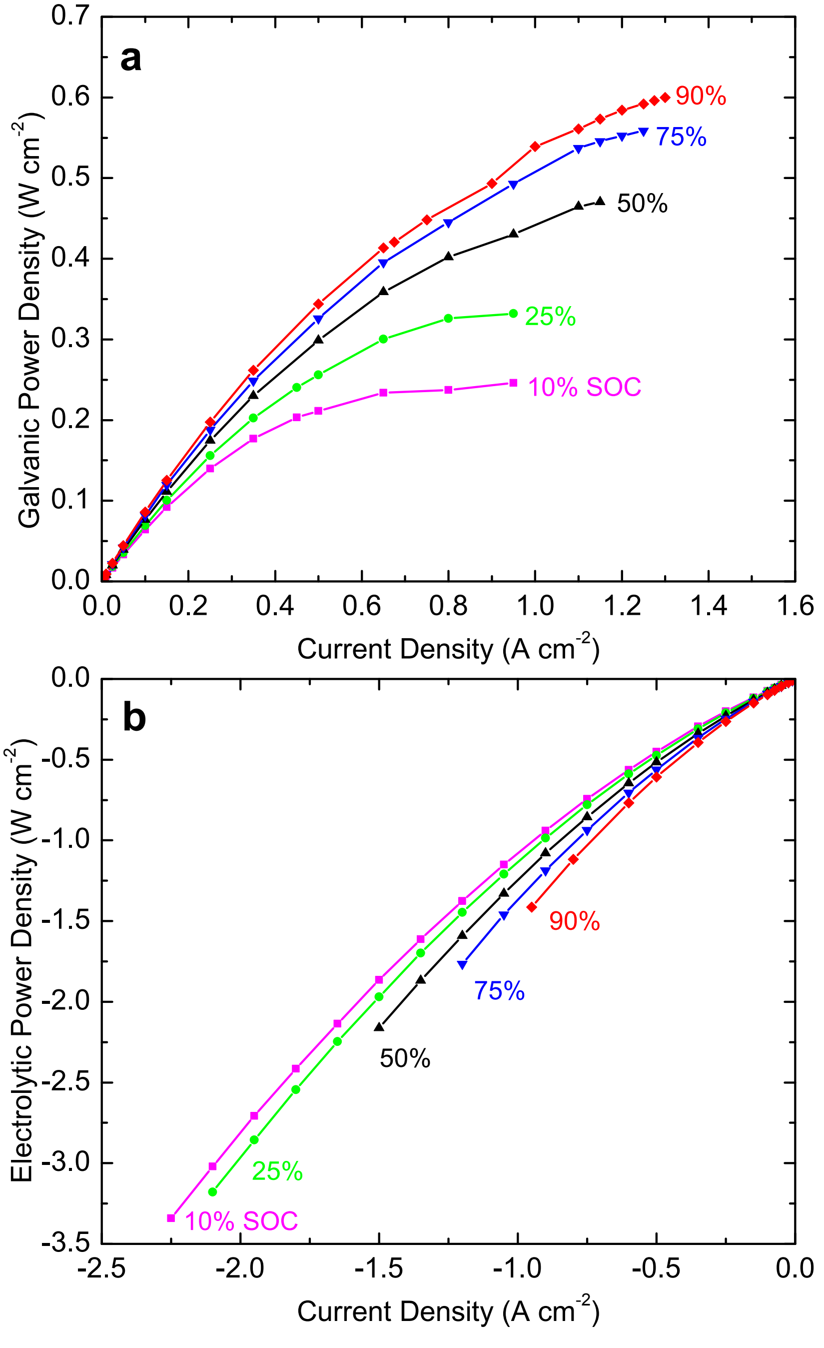

Figure 5.11. (**a**) Cell galvanic power density vs. current density at five different SOCs. (**b**) Cell electrolytic power density vs. current density at these same SOCs.

utilizing 50% of the total capacity of the battery, using a 0.1 M quinone solution. The cycles are highly reproducible and indicate that current efficiencies for the battery are around 95% (see Equation 5.2). Figure 5.12b shows constant-current cycling data, collected at $\pm$ 0.5 A cm^2, using voltage cut-offs of 0 V and 1.5 V. These tests were done using the identical solutions used in the battery for Figures 5.10-5.11. The galvanic discharge capacity retention (i.e. the number of coulombs extracted in one discharge cycle divided by the number of coulombs extracted in the previous discharge cycle; see Equation 5.3) is above 99%, indicating the battery is capable of operating with minimal capacity fade. Full characterization of the current efficiency will require slower cycling experiments and chemical characterization of the electrolyte solutions after extended cycling.

Longer cycling experiments were then conducted using a thicker membrane. The more substantial membrane should have the effect of reducing any crossover in the battery, thereby increasing its ability to retain charge. A diaphragm pump was also used on the quinone side of the cell in lieu of the centrifugal pump used for the previous experiments. Although the diaphragm pump's flow rate is significantly lower than the centrifugal pump, and the diaphragm pump's flow pulses considerably, it is advantageous to use this pump because its internal volume is extremely small relative to that of the centrifugal pump, so less quinone electrolyte can be used. Thus, the total capacity of the battery is reduced, thereby accelerating cycling measurements. A 5 cm^2 electrode was used as well in order to increase the total current that could be drawn from the battery. Figure 5.13 shows the results of these cycling experiments. 106 total cycles are shown. Given the time scale, the individual cycles are difficult to discern, but, when zoomed in (Figure 5.13b), they closely resemble the cycles seen in Figure 5.12. Note the remarkably high capacity retention observed over this larger number of cycles (99.986% average retention per cycle, or

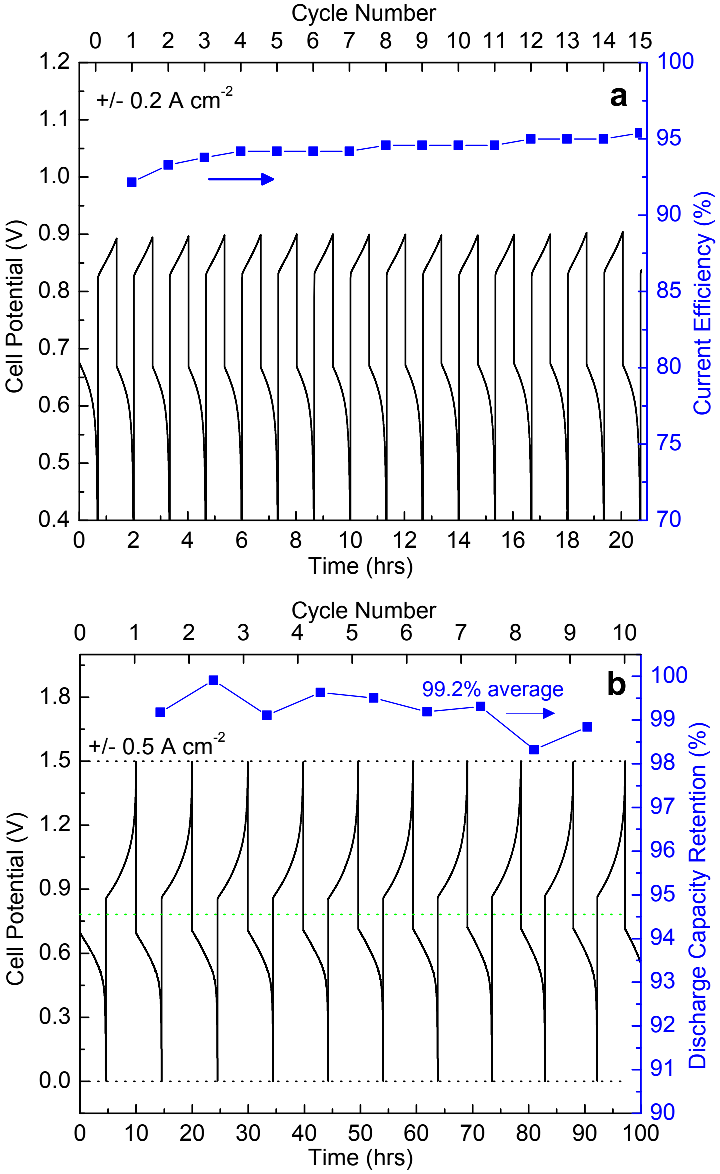

Figure 5.12. (**a**) Constant-current cycling at 0.2 A cm^{-2} at 40 °C using a 2 M HBr + 0.5 M Br_2 solution on the positive side and a 0.1 M AQDS + 2 M H_2SO_4 solution on the negative side; current efficiency is indicated for each complete cycle. (**b**) Constant-current cycling at 0.5 A cm^{-2} at 40 °C using a 3 M HBr + 0.5 M Br_2 solution on the positive side and a 1 M AQDS + 1 M H_2SO_4 solution on the negative side (same solution used in Figures 5.10-5.11); discharge capacity retention is indicated for each cycle.

98.5% retention over the entire 106 cycles), indicating that the stability of the quinones is extremely high and that they are capable of being cycled a large number of times with minimal fade in the capacity[iv]. Further experiments are still needed to determine the reasons for the relatively modest current efficiency observed for these data (72.0% on average).

Lastly, it is important to note that the battery is capable of operating with an identical HBr electrolyte on both sides of the cell. This would simplify operation somewhat in that there would no longer be HBr on one side and H_2SO_4 on the other, so any issues associated with sulfate or bromide diffusion through the membrane would be eliminated. Figure 5.14 demonstrates that the battery can be cycled with comparable performance to that seen in Figure 5.12.

5.5 CONCLUSIONS

This chapter explored the use of organic chemistries in a flow battery and the use of quinones in particular. It began by looking at the electrochemical properties of some of these molecules, highlighting their reversibility, fast kinetics, reasonable diffusivities, and high solubilities. Focusing on AQDS, RDE data were obtained, and Levich and Koutecký-Levich plots were generated. This allowed for the calculation of a diffusion coefficient for AQDS ($D = 3.8 \times 10^{-6}$ $cm^2\ s^{-1}$) and i_K, the current in the absence of any mass transport effects. From this number, a fit to the Butler-Volmer equation can be calculated, and, from this fit, the transfer coefficient (α = 0.474) and rate constant ($k_0 = 7.2 \times 10^{-3}$ cm s^{-1}) for the AQDS/$AQDSH_2$ redox couple on a

---

[iv] The capacity retention is likely to compound over a large number of cycles, so it is absolutely essential that this number is very close to 1. Even with a capacity retention of 99.99%, for example, the battery will have lost nearly 10% of its capacity over 1,000 cycles. This would change to a $<$ 1% loss if the capacity retention could be increased to 99.999%, or would increase to over 60% if the retention fell to 99.9%.

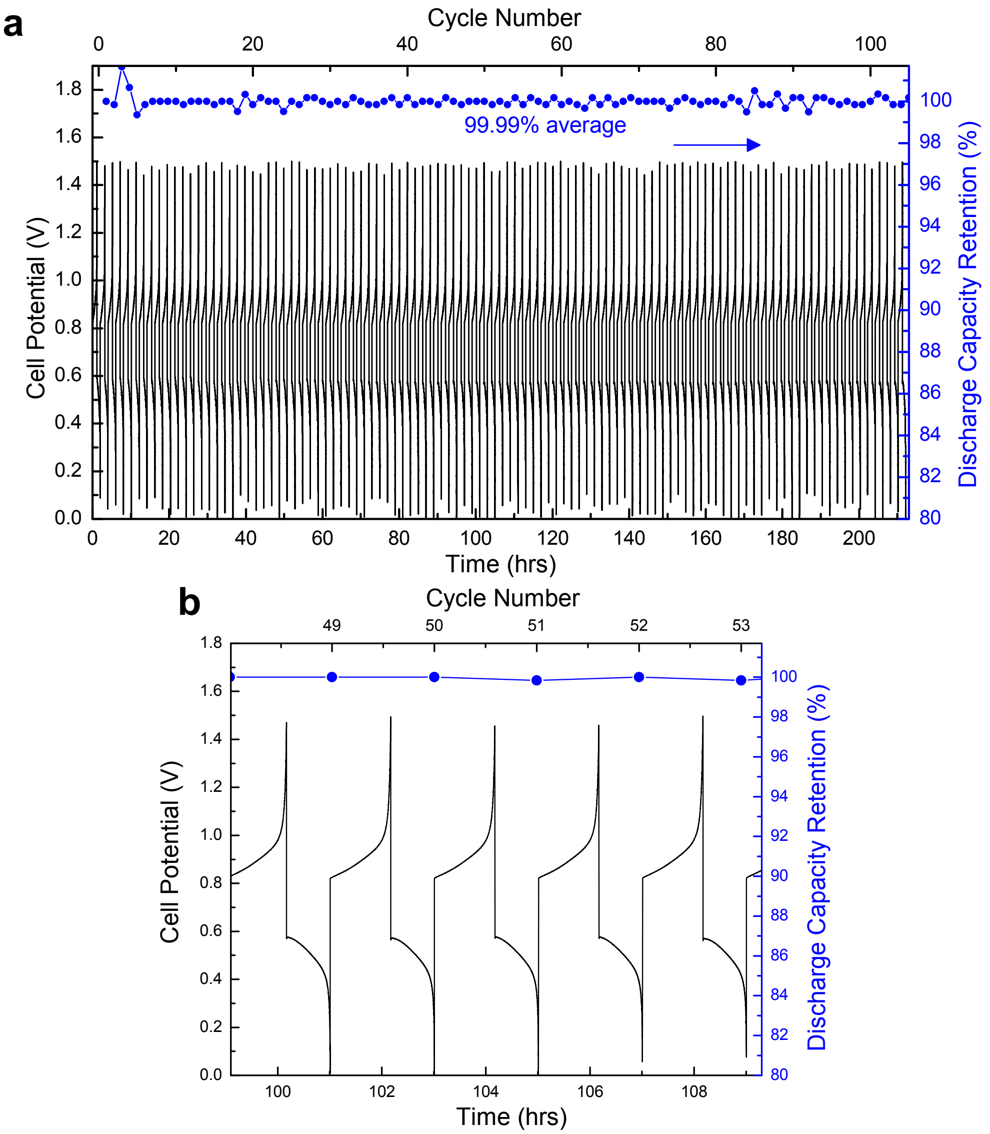

Figure 5.13. (**a**) Constant-current cycling at 0.25 A cm^{-2} at 30 °C using a 3 M HBr + 0.5 M Br_2 solution on the positive side and a 1 M AQDS + 1 M H_2SO_4 solution on the negative side; discharge capacity retention is indicated for each cycle. These data were collected using a thicker membrane (125 μm, Nafion 115) and a lower AQDS volume than previous cycling experiments. (**b**) The same data as in (a), but zoomed in on a smaller time scale to clearly show the shape of the charge-discharge curves. The battery lost 1.5% of its capacity over these 106 cycles.

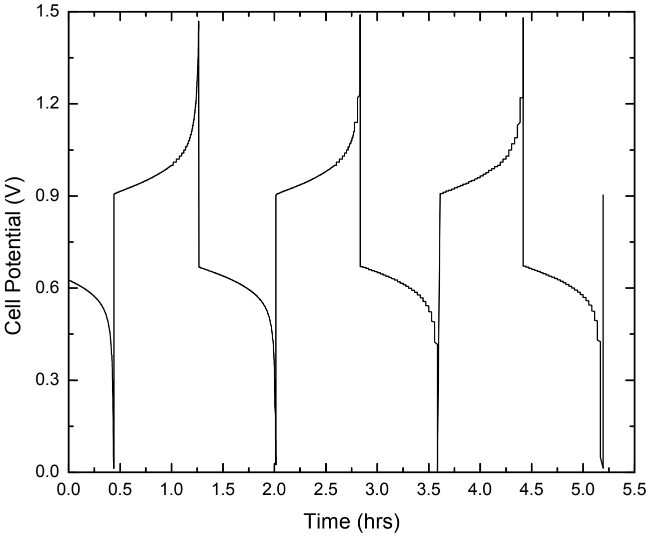

Figure 5.14. Flow battery cycling behavior with HBr electrolyte on both sides. Data collected by cycling the current at 0.2 A cm^{-2} at 40 °C using a 2 M HBr + 0.5 M Br_2 solution on the positive side and a 2 M HBr + 0.1 M AQDS solution on the negative side; cycling performance is comparable to data in Figure 5.12.

glassy carbon electrode were found. After this, the chapter focused on the implementation of various quinones in a flow battery. Initial studies on the use of several benzoquinones were first reported, with 1,4-parabenzoquinone being the most promising. This compound, however, was found to be unsuitable for use in a battery, presumably due to its propensity to complex with its reduced counterpart and form quinhydrone. Finally, the use of AQDS and its use in a well-functioning battery was described. The battery used inexpensive carbon electrodes, combining the AQDS/$AQDSH_2$ couple with the Br_2/Br^- redox couple, yielding a peak galvanic power density exceeding 0.6 W cm^{-2} at 1.3 A cm^{-2}. Cycling of the QBFB showed 99.99% storage capacity retention per cycle.

The organic approach described in this chapter liberates battery redox chemistry from the constraints of the limited number of elemental redox couples of the periodic table. Quinones offer several advantages over current flow battery technologies, and we believe that the use of quinones in batteries represents a very promising development in flow battery R&D. Optimization of engineering and operating parameters such as the flow field geometry, electrode design, membrane separator, and temperature — which have not yet even begun — should lead to even more significant performance improvements in the future.

Now this is not the end. It is not even the beginning of the end. But it is, perhaps, the end of the beginning.

Winston Churchill

6

Conclusions and Future Directions

THIS DISSERTATION explored several different chemistries and materials for applications in grid-scale energy storage. Chapter 2 detailed the development of a high-performance hydrogen-chlorine regenerative fuel cell. Chapter 3 explored the use of a number of different oxide alloys as effective chlorine redox catalysts, determining that ruthenium-cobalt oxide alloys are particularly promising. Chapter 4 delved into a performance model of a hydrogen-bromine flow battery, detailing the effects of various operating conditions and cell parameters on the performance and efficiency of the device. Chapter 5 focused on the use of quinones in a battery, demonstrating some of the desirable properties quinones have.

In addition to some future experiments suggested within the chapters themselves, there is a number of experiments that could be done in the future to further elucidate the results presented here. Both the chlorine-based and quinone-based devices would greatly benefit from extensive modeling of the fluid dynamics occurring in the flow plates and within the electrodes themselves. This could lead to improved cell architectures that would significantly boost performance.

For the oxide alloy work, testing a larger number of alloys would of course be beneficial. Furthermore, if a process could be developed for depositing thin, smooth films of these various alloys, the results in this work could be significantly refined to eliminate surface area effects that could reside in the data. Further stability tests would enhance the work as well, providing further evidence that these materials are capable of excellent performance over extended time periods. This work could also benefit from more extensive chemical analyses, in an attempt to determine the ruthenium concentration as a function of depth into the crystals, as surface area enrichment could complicate the results presented here.

For the hydrogen-bromine modeling work, inclusion of porous electrode theory would likely refine the mass transport behavior of the model and allow it to more accurately predict experimental cell performance. Furthermore, inclusion of electro-osmotic drag and crossover would allow for more nuanced outputs from the model.

Regarding the quinone work, the most obvious advance is to test a larger and larger set of molecules in both half-cell and full-cell experiments. Longer cycling experiments are also needed.

In-depth chemical analyses of the quinone electrolyte as a function of cycle time would greatly increase our understanding of the lifetime of the quinone molecules and of other parisitic losses in the cell. Furthermore, the development of a high-potential quinone would represent a huge advance in this field. There are also likely interesting opportunities for developing solid quinone composite electrodes and pairing these with one of many other possible chemistries (other quinones, lead, etc.).

Energy storage is an exciting and rapidly developing field. With a huge number of potentially transformative applications for storage technologies, I hope this dissertation serves as a small but meaningful advancement in this space.

A

Matlab Code for Chapter 4

The following contains the Matlab code used to produce the results seen in Chapter 4: Modeling the Hydrogen-Bromine Regenerative Fuel Cell. A number of lines of code are commented out. Some of these lines consist of prose meant to explain the purpose of particular pieces of code, but others are commented out because the program, as it is written, is not capable of producing *every* plot in Chapter 4 by running the code once. Rather, the program should be run with certain inputs to get the desired outputs while commenting out other lines that would conflict with this. For example, the line “Tlin=linspace(5,75,20);” creates a vector called Tlin that contains 20 entries evenly-spaced between the values of 5 and 75. The following line “Tlin=50” would erase this vector and reassign Tlin the single value of 50. Thus, if you want to run the code at a variety of temperatures, this second line must be commented out. There are also significant pieces of legacy code that were not used to generate the plots in Chapter 4, but still could be useful at some point down the line nonetheless. These pieces can of course be ignored without affecting the output of the model.

```
clear all;
%Physical constants:
R=8.314472; %ideal gas constant [J/(mol*K)]
F=96485.3399; %Faraday's constant [C/mol_e-]
%OPERATING PARAMETERS
Tlin = linspace(5,75,20); %temperature (C)
%Tlin=50;
M_HBr = linspace(0.5,7,1000); %Molarity [mol/L]
%M_HBr = 1;
M_Br2 = M_HBr;
jlin=linspace(-3000,3000,602); %current density [mA/cm^2]
overpotential_mesh_size = 1000; %sets size of eta_aH_lin and eta_BV_lin
%ENGINEERING PARAMETERS
p_H2 = 1; %hydrogen partial pressure [atm]
j_0_Br = 183.5; %j_0_Br=the exchange current density of the
% Br electrode[mA/cm^2]
j_0_H = 600; %j_0_H=the exchange current density of the H
% electrode[mA/cm^2]
epsilon=27e-4; %electrode thickness/diffusion layer thickness [cm]
L = 0.0178/7*2; %thickness of the Nafion membrane [cm];
%-----------------------------------------------------------------------
%EQUILIBRIUM POTENTIAL:
% The equilirium potential E_eq is a function of several different
% variables, which will be dealt with in a number of different steps here.
% Note that E_eq is INDEPENDENT of the current density j.
%X represents the weight fraction of HBr in the electrolyte. This is a
%function of the HBr molarity (it should be a function of the Br2 molarity
%as well, but Yeo and Chin assume this is 1).
%We'll need to calculate the weight fraction X as a function of these
    %variables.
MW_HBr = 80.91; %MW of HBr [g/mol]
MW_Br2 = 79.904*2; %MW of Br2 [g/mol]
%We need to know the density of HBr as a function of T and M_HBr
phi = zeros(length(Tlin), length(jlin), length(M_HBr));
[T_mesh, j_mesh, M_HBr_mesh]=ndgrid(Tlin, jlin, M_HBr);
M_Br2_mesh = M_HBr_mesh;
```

```
%Fitting parameters and equation are from "Densities of Binary Aqueous
%Solutions of 306 Inorganic Substances" by P Novotny and O. Sohnel, J.
%Chem. and Eng. Data, vol. 33, no. 1, 1988
%%density of pure water (kg/m^3):
rho_H2O = 999.65 + .20438*T_mesh - 0.06174*T_mesh.^(3/2);
%Fitting parameters specific to HBr:
A = 0.5998 *10^2;
B = 1.300 *(-0.1);
C = 1.061 /1000;
D = 1.263 *(-1);
E_ = 2.160 /100;
F_ = 1.647 /(-10000);
%Equation for the density of HBr:
density_of_HBr = rho_H2O + A*M_HBr_mesh + B*M_HBr_mesh.*...
    T_mesh + C*M_HBr_mesh.*(T_mesh.^2) + D*M_HBr_mesh.^(3/2) + ...
    E_*(M_HBr_mesh.^(3/2)).*T_mesh + ...
    F_*(M_HBr_mesh.^(3/2)).*(T_mesh.^2); %[kg/m3]
%Now we can calculate the weight fraction of HBr:
X = MW_HBr*M_HBr_mesh.*(density_of_HBr.^(-1));
%Now we need to define phi according to Yeo and Chin
for k=1:1:(length(Tlin)*length(jlin)*length(M_HBr))
    if ((0.016 < X(k)) && (X(k) < 0.11))
    phi(k) = 1.073-0.0567*log(12.36*X(k)/(1-X(k)));
    end

    if ((0.11 < X(k)) && (X(k) < 0.28))
    phi(k) = 1.095-0.1042*log(12.36*X(k)/(1-X(k)));
    end

    if ((0.28 < X(k)) && (X(k) < 0.58))
    phi(k) = 1.336-0.2581*log(12.36*X(k)/(1-X(k)));
    end
end
%compute the molality of the solution using eqn. 9 in Rugolo J ECS
m = 1000*M_HBr_mesh./(density_of_HBr-MW_HBr*M_HBr_mesh);
%Now we need to compute activity coefficients for HBr; Data is
%from Table 2 in Faita, J Chem Eng Data, 1966
%ROW 1 in gamma data below is from interpolation from CRC data (mean
%activity coefficients of electrolytes as a function of concentration);
%I used the datapoint for 10 mol/kg HBr (33.4) and then interpolated this
%linearly in temp based on the fact that, at 5.551 mol/kg HBr, the activity
%coefficient changes 31% from 0 C to 70 C
molality_gamma = [10
5.551
4.629
3.7
2.775
1.85
1.388
1.119
0.925
0.555
0.277
0.139
0.0555];
temp_gamma = [0 10  20  25  30  40  50  60  70];
gamma =[
33.4   32.118   30.837   29.555   28.273   26.992   25.710   24.428   23.146;
```

```
6.32    6.06    5.76    5.61    5.45    5.15    4.86    4.6     4.36;
3.298   3.114   2.945   2.871   2.798   2.642   2.496   2.373   2.221;
2.217   2.17    2.116   2.079   2.041   1.957   1.898   1.815   1.731;
1.562   1.539   1.51    1.491   1.467   1.429   1.398   1.36    1.316;
1.136   1.117   1.108   1.102   1.091   1.068   1.064   1.04    1.013;
0.945   0.942   0.936   0.933   0.931   0.923   0.918   0.914   0.906;
0.883   0.879   0.873   0.87    0.866   0.857   0.848   0.84    0.827;
0.861   0.857   0.852   0.849   0.846   0.839   0.829   0.815   0.803;
0.801   0.796   0.791   0.788   0.786   0.778   0.765   0.747   0.728;
0.791   0.788   0.784   0.781   0.78    0.776   0.77    0.762   0.756;
0.83    0.828   0.826   0.825   0.823   0.819   0.812   0.808   0.8;
0.838   0.837   0.836   0.836   0.834   0.836   0.828   0.823   0.815];
gamma = gamma';
[temp_gamma_mesh,molality_gamma_mesh] = ...
    ndgrid(temp_gamma,molality_gamma);
%m = reshape(m,1, length(M_HBr));
%T_mesh = reshape(T_mesh,1,length(M_HBr));
%X=reshape(X,1,length(M_HBr));
%phi=reshape(phi,1,length(M_HBr));
%M_Br2_mesh=reshape(M_Br2_mesh,1,length(M_HBr));
%M_HBr_mesh=reshape(M_HBr_mesh,1,length(M_HBr));
%interpolated_gamma = griddata(molality_gamma_mesh, ...
    %temp_gamma_mesh,gamma,m,T_mesh);
%Now we can define the equilibrium potential:
E_eq_yeo = phi-(T_mesh-25).*(4.3+1.86*log(12.36*X./(1-X))).*10^(-4)+...
    4.31*10^(-5)*(T_mesh+273.15).*(log(p_H2)+log(M_Br2_mesh));
% The above equation assumes an activity coefficient of 1 for ...
    %hydrogen and bromine
%The three lines below must be un-commented for the figure
    %generation to work
% E_eq = reshape(E_eq,length(Tlin),length(M_HBr));
% T_mesh_reduced = reshape(T_mesh,length(Tlin),length(M_HBr));
% M_HBr_mesh_reduced = reshape(M_HBr_mesh,length(Tlin), ...
    %length(M_HBr));
E_eq_ideal = 1.267929-0.0006105*(T_mesh+273.15) + ...
    R*T_mesh./(2*F).*log(p_H2*M_Br2_mesh./(M_HBr_mesh.^4));
%------------------------------------------------------------------
%MEMBRANE RESISTANCE OVERPOTENTIAL
%Calculating the Nafion Membrane Resistance as a function of Molarity,
%Temperature, and Current Density
%Defining sigma requires an empirical fit that depends on M and T
T_mesh = zeros(length(Tlin), length(jlin), length(M_HBr));
j_mesh = zeros(length(Tlin), length(jlin), length(M_HBr));
M_HBr_mesh = zeros(length(Tlin), length(jlin), length(M_HBr));
[T_mesh, j_mesh, M_HBr_mesh]=ndgrid(Tlin, jlin , M_HBr);
%INTERPOLATION IN MATLAB:
%Data is from Baldwin (1987) and Sone (1996) for the 0 M data point
molarity_Baldwin = [0 1.34 2.07 3.88 5.15 7.32];
E_a = [0.2629 3.2 3.49 2.32 2.2 2.88];
A_ = [0.1225 14.9582 23.712 3.5704 2.1642 3.4259];
temperature_fit = 5:1:75;
[temperature_fit_mesh, molarity_fit_mesh] = ...
    ndgrid(temperature_fit,molarity_Baldwin);
sigma_fit_0 = A_(1)*exp(-E_a(1)*...
    (0.00198588*(temperature_fit+273.15)).^(-1));
sigma_fit_134 = A_(2)*exp(-E_a(2)*...
    (0.00198588*(temperature_fit+273.15)).^(-1));
sigma_fit_207 = A_(3)*exp(-E_a(3)*...
```

```
    (0.00198588*(temperature_fit+273.15)).^(-1));
sigma_fit_308 = A_(4)*exp(-E_a(4)*...
    (0.00198588*(temperature_fit+273.15)).^(-1));
sigma_fit_515 = A_(5)*exp(-E_a(5)*...
    (0.00198588*(temperature_fit+273.15)).^(-1));
sigma_fit_732 = A_(6)*exp(-E_a(6)*...
    (0.00198588*(temperature_fit+273.15)).^(-1));
sigma_fit_comp = [sigma_fit_0; sigma_fit_134; sigma_fit_207;...
    sigma_fit_308; sigma_fit_515; sigma_fit_732];
sigma_interp_comp = interp2(temperature_fit,molarity_Baldwin,...
    sigma_fit_comp,T_mesh,M_HBr_mesh,'spline');
sigma_interp_comp_reduced = ...
    reshape(sigma_interp_comp(:,1,:),length(Tlin),length(M_HBr));
%To plot conductivity:
%surf(M_HBr_mesh,T_mesh,sigma_interp_comp_reduced)
%Lastly, calculating the resistive overpotential:
eta_R = -(L*(sigma_interp_comp.^(-1)).*j_mesh)./1000;
%-------------------------------------------------------------------------
%HYDROGEN ACTIVATION OVERPOTENTIAL
%Calculating the H2 Activation Overpotential as a Function of Temperature
%The hydrogen activation overpotential is INDEPENDENT of molarity.
alf_H = 0.5; %transfer coefficient of H electrode [dimensionless]
eta_aH_lin=linspace(-max(max(max(E_eq_yeo))),...
    max(max(max(E_eq_yeo))),overpotential_mesh_size);
    %hydrogen activation overpotential [mV]
[T_mesh, j_mesh, eta_aH_mesh, M_HBr_mesh]=...
    ndgrid(Tlin, jlin, eta_aH_lin,M_HBr);
f = F*(((T_mesh+273.15).*R).^(-1)); %useful parameter [1/V]
%Computing eta_aBr: since the Butler-Volmer equation is an implicit
%expression for eta_aBr, here we use a minimization to numerically
%determine which eta_aBr best satisfies the Butler-Volmer equation for a
%given current density
result = j_mesh - j_0_H*(exp(-alf_H*f.*eta_aH_mesh)-...
    exp((1-alf_H)*f.*eta_aH_mesh)); %The Butler-Volmer Equation
result=abs(result); %taking the absolute value of the "result" matrix,
     %so we can do minimizations
[answer,indexOfZeroinResultMatrix]=min(result,[],3);
eta_aH =eta_aH_lin(indexOfZeroinResultMatrix);
eta_aH = reshape(eta_aH,length(Tlin),length(jlin),length(M_HBr));
%-------------------------------------------------------------------------
%MASS TRANSPORT OVERPOTENTIAL
% Calculating the Mass Transport Overpotenial at the Bromine
    %Electrode as a Function of Temperature, Molarity, and Current Density
eta_BV_lin=linspace(-max(max(max(E_eq_yeo))),...
    max(max(max(E_eq_yeo))),overpotential_mesh_size);
    %overpotential from Butler-Volmer equation accounting for
    %concentration effects
alf_Br = 0.5;
[T_mesh, j_mesh, eta_BV_mesh, M_HBr_mesh]=...
    ndgrid(Tlin, jlin, eta_BV_lin,M_HBr); %defines a 4-D matrix for variables
eta_aBr_mesh=eta_BV_mesh; %defining an overpotential regime for the...
    %bromine activation overpotential
M_Br2_mesh = M_HBr_mesh;
eta_aBr_lin = eta_BV_lin;
%The following line calculates the viscosity of pure water as a function of
%temp. using eqn. 11 in Laliberte 2007
viscosity_H2O = (T_mesh+246)./((0.05594*T_mesh +5.2842).*...
    T_mesh+137.37);
```

```
D_Br2 = 10^(-7)*18.0153^0.5*(273.15+T_mesh)./...
    (viscosity_H2O*18.9^(1/3)*53.2^(1/3));
    %Diffusion coefficient [cm2/s]; fit is eq. 2 Reddy 1967
C_ox = M_Br2_mesh./1000 - (j_mesh.*epsilon)./...
    (2*F*D_Br2*1000); %conc. of oxidant at electrode surface [mol/cm3]
%The following for loop ensures that no negative values of C_ox arise (that
% is, C_ox can only go as low as zero, and this loop takes any negative
% values in C_ox and changes them to zero)
for k=1:1:length(Tlin)*length(jlin)*length(eta_BV_lin)*length(M_HBr)
    if C_ox(k) < 0
        C_ox(k) = 0;
    end
end
%Determining the concentration of Cl- near the electrode:
% C_red_eq = M_mesh./1000; %equilibrium concentration of...
     %reduced species in bulk solution [mol/cm3]
D_Br = 10^(-7)*18.0153^0.5*(273.15+T_mesh)./...
    (viscosity_H2O*18.9^(1/3)*27^(1/3));
     %Diffusion coefficient [cm2/s]; fit is eq. 2 Reddy 1967
C_red = M_HBr_mesh./1000 + (j_mesh.*epsilon)./(F*D_Br*1000);
     %concentration of reduced species at the electrode surface [mol/cm3]
f = F*(((T_mesh+273.15).*R).^(-1)); %useful parameter [1/V]
%Computing eta_BV: since the Butler-Volmer equation is an implicit
%expression for eta_aBr, here we use a minimization to numerically
%determine which eta_aBr best satisfies the Butler-Volmer equation for a...
     %given current density
%eta_BV is the CONCENTRATION-DEPENDENT Butler-Volmer Equation
result_BV = j_mesh - j_0_Br*((C_ox./(M_Br2_mesh./1000)).*...
    exp(-alf_Br*f.*eta_BV_mesh)-(C_red./(M_HBr_mesh./1000)).*...
    exp((1-alf_Br)*f.*eta_BV_mesh));
    %The concentration-dependent Butler-Volmer Equation
result_BV=abs(result_BV); %taking the absolute value of the ”result”...
    %matrix, so we can do minimizations
[answer_BV,indexOfZeroinResultMatrix_BV]=min(result_BV,[],3);
eta_BV = eta_BV_lin(indexOfZeroinResultMatrix_BV);
eta_BV = reshape(eta_BV,length(Tlin),length(jlin),length(M_HBr));
%The following for loop ensures that the true limiting current density
%appears on the plot. This is difficult to describe...comment out this loop
%and re-run this program to see the effect that it has. It effectively
%eliminates an artificial ”shelf” that arises because the possible range of
%eta_BV is limited by how one defines eta_BV_lin above.
for k=1:1:(length(jlin)*length(M_HBr)*length(Tlin))
    if eta_BV(k) <= -(max(max(max(E_eq_yeo))))
       eta_BV(k) = -100;
    end
end
%Computing eta_aBr: since the Butler-Volmer equation is an implicit
%expression for eta_aBr, here we use a minimization to numerically
%determine which eta_aBr best satisfies the Butler-Volmer equation for a
%given current density
result_aBr = j_mesh - j_0_Br*(exp(-alf_Br*f.*eta_aBr_mesh)-...
    exp((1-alf_Br)*f.*eta_aBr_mesh));
abs_result_aBr=abs(result_aBr); %The Butler-Volmer Equation
[answer_aBr,indexOfZeroinResultMatrix_aBr]=min(abs_result_aBr,[],3);
eta_aBr = eta_aBr_lin(indexOfZeroinResultMatrix_aBr);
eta_aBr = reshape(eta_aBr,length(Tlin),length(jlin),length(M_HBr));
%Computing eta_MT, where eta_MT is defined as the difference
   %between the concentration-dependent and concentration-independent
```

```
   %Butler-Volmer equations:
eta_MT = (eta_BV-eta_aBr);
%---------------------------------------------------------------------
%THE MODEL
E =  E_eq_yeo  + eta_R  + eta_aBr + eta_aH + eta_MT;
%POWER CALCULATIONS
p = bsxfun(@times,E,jlin); %power density of the cell [mW/cm2]
row_max = max(p,[],1); %computes max power in 1st dimension
column_max = max(row_max,[],2); %computes max power in 2nd dim.
depth_max = max(column_max,[],3); %computes max power in 3rd dim.
[row,col]=find(p==max(depth_max)); %finds the row and column where the ...
     %max power actually occurs
Max_power_2=max(p,[],2); %computes a max power in the current density...
     %dimension (used for plotting purposes)
Max_power_3=reshape(Max_power_2,length(Tlin),length(M_HBr));
     %used for plotting purposes
[M_plot,temp_plot]=meshgrid(M_HBr,Tlin); %used for plotting purposes
row_min = max(p,[],2); %computes max power in jlin dimension
column_min = min(row_min,[],2); %computes min power in temp
depth_min = min(column_min,[],3); %computes min power in conc
[row3,col3]=find(p==min(depth_min));
    %finds the row and column where the max power actually occurs
%---------------------------------------------------------------------
% %FIGURE GENERATION
% figure(1)
% surfc(temp_plot,M_plot,Max_power_3)
% xlabel('Temperature [C]')
% xlim([5 75])
% ylabel('Concentration [mol/L]')
% ylim([0.5 7.5])
% zlabel('Maximum Power Density [mW/cm^2]')
% set(figure(1),'color','white')
% title('Maximum Power Density as a function of Molarity and Temperature')
% figure(2)
% plot(jlin,E(row,:,9),'k',jlin,E_eq(row,:,9),jlin,eta_R(row,:,9),'r',...
     %jlin,eta_aCl(row,:,9),'g',jlin,eta_aH(row,:,9),'y',jlin,eta_MT(row,:,9),'c')
% legend('Overall Cell Potential','Equilibrium Cell Potential',...
%         'Ohmic Overpotential','Chlorine Activation Overpotential',...
%         'Hydrogen Activation Overpotential','Mass Transport Overpotential')
% xlabel('Current Density (mA/cm^2)')
% ylabel('Potential (V)')
% title('Fuel Cell Losses near Optimum Conditions')
% ylim([-1 1.5])
% xlim([0 1500])
% figure(3)
% plot(jlin,E(5,:,2),'k',jlin,E_eq(5,:,2),jlin,eta_R(5,:,2),'r',jlin,...
%         eta_aCl(5,:,2),'g',jlin,eta_aH(5,:,2),'y',jlin,eta_MT(5,:,2),'c')
% legend('Overall Cell Potential','Equilibrium Cell Potential',...
%         'Ohmic Overpotential','Chlorine Activation Overpotential',
%         'Hydrogen Activation Overpotential','Mass Transport Overpotential')
% xlabel('Current Density (mA/cm^2)')
% ylabel('Potential (V)')
% title('Fuel Cell Losses at 25C and 1M HCl')
% ylim([-1 1.5])
% xlim([0 1500])
efficiency = E./E_eq_yeo;
for k=1:1:(length(M_HBr)*length(Tlin)*length(jlin))
    if efficiency(k)>1
```

```
        efficiency(k)=0;
    end
end
efficiency_difference = efficiency - 0.9;
for k=1:1:(length(M_HBr)*length(Tlin)*length(jlin))
    if efficiency_difference(k)<0
        efficiency_difference(k)=1;
    end
end
efficiency_difference = abs(efficiency_difference);
[answer_eff,indexOfZeroinResultMatrix_eff]=min(efficiency_difference,[],2);
current_90percent_eff = jlin(rem(indexOfZeroinResultMatrix_eff,length(jlin)));
%If you run the code at a single temp and/or concentration, define
%E_90percent_ef using the code below:
E_90percent_eff=zeros(length(Tlin),1,length(M_HBr));
for k=1:1:length(M_HBr)*length(Tlin)
    E_90percent_eff(k) = E((k-1)*length(jlin)+indexOfZeroinResultMatrix_eff(k));
end
power_90percent_eff_3d = current_90percent_eff.*E_90percent_eff;
% power_90percent_eff_3d_smooth = smooth3(power_90percent_eff_3d);
% power_90percent_eff_smooth = reshape(power_90percent_eff_3d_smooth,...
     %length(Tlin),length(M_HBr));
power_90percent_eff = reshape(power_90percent_eff_3d,...
    length(Tlin),length(M_HBr));
row_max = max(p,[],1); %computes max power in 1st dimension
column_max = max(row_max,[],2); %computes max power in 2nd dim.
depth_max = max(column_max,[],3); %computes max power in 3rd dim.
[row,col]=find(p==max(depth_max)); %finds the row and column where the...
     %max power actually occurs
power_90percent_eff_max = max(power_90percent_eff); %maximum
     %power density of the cell [mW/cm2]
%-----------------------------------------------------------------
%DATA COMPARISONS TO MODEL
%Kreutzer/Nguyen from Fig. 10: first column is current density, second is
%potential, third is calculated power; data found using PlotDigitizer
kreutzer_23 = [0.00102225    0.993378     0.001015481;
0.037283     0.988464     0.036852903;
0.0856428    0.973334     0.083359049;
0.129183     0.947878     0.122449724;
0.184809     0.9225   0.170486303;
0.257389     0.871495     0.224313227;
0.305763     0.846071     0.258697207;
0.354152     0.810352     0.286987782;
0.395254     0.800322     0.316330472;
0.429127     0.774804     0.332489316;
0.477509     0.744233     0.355377956;
0.499283     0.728931     0.363942856;
0.537982     0.708591     0.381209203;
0.559778     0.677849     0.379444958;
0.57915 0.652238     0.377743638;
0.598507     0.636921     0.381201677;
0.605801     0.606085     0.367166899];

kreutzer_35 = [0.00343185    0.998541     0.003426843;
0.0711488    0.968093     0.068878655;
0.121947     0.937537     0.114329825;
0.175148     0.917291     0.160661684;
0.228349     0.897044     0.2048391;
```

```
0.283982    0.866519    0.246075799;
0.332341    0.851389    0.282951472;
0.387967    0.826011    0.32046501;
0.433924    0.800571    0.347386971;
0.472616    0.785378    0.371182209;
0.513762    0.744466    0.382478341;
0.554879    0.724142    0.401811189;
0.588752    0.698624    0.411316277;
0.615359    0.683353    0.420507419;
0.644413    0.64751 0.417263862;
0.668619    0.62193 0.415834215;
0.685573    0.596304    0.408809922];

kreutzer_45 = [0.00343915   0.993393    0.003416428;
0.066315    0.968062    0.064197032;
0.13401 0.953056    0.127719035;
0.194476    0.922562    0.179416168;
0.264595    0.902425    0.238777143;
0.325054    0.877078    0.285097712;
0.385513    0.851731    0.328353373;
0.443555    0.826369    0.366540102;
0.491937    0.795797    0.391481989;
0.530629    0.780604    0.41421112;
0.571753    0.755133    0.431749558;
0.615294    0.729678    0.448966495;
0.644326    0.709276    0.457004968;
0.678199    0.683758    0.463723992;
0.709647    0.663372    0.47075995;
0.729026    0.632613    0.461191325;
0.748413    0.596708    0.446584024];
%Livshits\Peled from Fig. 5, 80 C, 0.9 M Br2 curve; first column is ...
    %current density, second is %potential, third is calculated power;
    %data found using PlotDigitizer
livshits_80 = [0    0.914084    0;
0.129231    0.903756    0.116793292;
0.290769    0.877934    0.255275991;
0.452308    0.857277    0.387753245;
0.603077    0.841784    0.507660569;
0.732308    0.826291    0.60509951;
1.15231 0.779812    0.898585166;
1.37846 0.748826    1.032226688;
1.69077 0.707512    1.196240064;
2.04615 0.666197    1.363138992;
2.30462 0.635211    1.463919975;
2.49846 0.604225    1.509631994;
2.66    0.568075    1.5110795;
2.76769 0.547418    1.515083324];
figure(1)
plot(jlin,E)
xlim([0 1000])
ylim([0 1.1])
hold on;
% scatter(kreutzer_23(:,1)*1000,kreutzer_23(:,2))
% scatter(kreutzer_35(:,1)*1000,kreutzer_35(:,2))
% scatter(kreutzer_45(:,1)*1000,kreutzer_45(:,2))
scatter(livshits_80(:,1)*1000,livshits_80(:,2))
% 90percent_power_temperature = Tlin(row) %finds the temperature at...
    %which the maximum power density occurs
```

```
% power_90percent_molarity = M_HBr(ceil(col/length(jlin)))
ans1=[jlin' E' eta_R' eta_aBr' eta_aH' eta_MT' efficiency' p'];
% figure(2)
% surfc(temp_plot,M_plot,power_90percent_eff_smooth)
% xlabel('Temperature')
% xlim([5 75])
% ylabel('Concentration')
% ylim([0.5 7.5])
% zlabel('Power Density at 90% Efficiency [mW/cm^2]')
% set(figure(2),'color','white')
% title('Power Density at 90% Efficiency as a ...
    %function of Molarity and Temperature')
% row_max_eff = max(p,[],1); %computes max power in 1st dimension
% column_max_eff = max(row_max,[],2); %computes max power in 2nd dim.
% depth_max_eff = max(column_max,[],3); %computes max power in 3rd dim.
% [row_eff,col_eff]=find(p==max(depth_max_eff)); %finds the row and column
     %where the max power actually occurs
% Max_power_eff = depth_max_eff; %maximum power density
    %of the cell [mW/cm2]
% Max_power_temperature_eff = Tlin(row_eff); %finds the temperature at
     %which the maximum power density occurs
% % Max_power_molarity = M(floor(col/length(jlin)))
% % Max_power_currentdensity = jlin(rem(col,length(jlin)))
% Max_power__eff_2=max(p,[],2); %computes a max power in the current
     %density dimension (used for plotting purposes)
% Max_power__eff_3=reshape(Max_power__eff_2,length(Tlin),length(M));
      %used for plotting purposes
% [M_plot,temp_plot]=meshgrid(M,Tlin); %used for plotting purposes
% plot(efficiency(2,:,2))
% Max_power_molarity = M(floor(col/length(jlin)))
%Max_power_currentdensity = jlin(rem(col,length(jlin)))
% figure(3)
% for k=1:1:(length(M)*length(Tlin)*length(jlin))
%     if E(k)<0
%         E(k)=0;
%     end
% end
% p = bsxfun(@times,E,jlin); %power density of the cell [mW/cm2]
% efficiency = E./E_eq;
% Max_power_450 = [];
% for k=1:1:(length(Tlin)*length(M))
%     if ((Max_power_3(k) <455) && (Max_power_3(k)>445))
%         Max_power_450(end+1)=Max_power_3(k);
%     end
% end
```

B

Matlab Code for Chapter 5

The following contains the Matlab code used to produce the cycling results seen in Chapter 5: Organic Chemistries in Flow Batteries and the Quinone Bromide Flow Battery. Instructions for executing the code are included in the comments below.

```
%Instructions: create a .csv file called ’time’ and a .csv file called
%potential and put them in the same folder as this file.
%Once you have those, just click ”Run” and the code will run, generating
%the variables below. Note that this program needs to start with a CHARGE
%half−cycle, not a discharge.
cycle_end_times = 0;
cycle_length = 0;
current_efficiency =0;
capacity_retention = 0;
time=csvread(’cycling_data.csv’,:,0);
time=time(:,1);
potential=csvread(’cycling_data.csv’,:,1);
%Loop to determine the time at which each half−cycle ends (basically, if
%the difference in potential between two consecutive data points is > 0.2
%V, then that is used as the indicator that the sign of the current has
%flipped and a new half−cycle has begun). This loop creates a matrix called
%cycle_end_times that lists the times where each of these switches happens
for k=1:1:(length(time)−1)
    if abs(potential(k)−potential(k+1)) > 0.2
    cycle_end_times = [cycle_end_times ; time(k)];
    end
end

cycle_end_times = [cycle_end_times ; time(length(time))];

%Loop to determine the length of each cycle. It compares the end time of
%one cycle to the end time of the previous cycle and puts the difference in
%a vector called cycle_length
for k=2:1:(length(cycle_end_times))
    cycle_length(k−1) =  cycle_end_times(k) − cycle_end_times(k−1);
end

%Loop to determine current efficiency
for k=2:2:(length(cycle_length))
   current_efficiency(k/2) =  cycle_length(k)/cycle_length(k−1);
end

%Loop to determine discharge capacity retention
for k=4:2:(length(cycle_length))
   capacity_retention(k/2−1) =  cycle_length(k)/cycle_length(k−2);
end
```

References

[1] OECD. *Renewable energy*. OECD Factbook 2011-2012: Economic, Environmental and Social Statistics (OECD Publishing, 2011).

[2] Kassakian, J. G. & Schmalensee, R. (eds.) *The Future of the Electric Grid*. An Interdiscplinary MIT Study (Massachusetts Institute of Technology, 2011).

[3] Rastler, D. Electricity Energy Storage Technology Options. Tech. Rep. 1020676, Electric Power Research Institute (2010).

[4] Barnhart, C. J. & Benson, S. M. On the importance of reducing the energetic and material demands of electrical energy storage. *Energy & Environmental Science* **6**, 1083–1092 (2013).

[5] OECD. *Electricity generation*. OECD Factbook 2011-2012: Economic, Environmental and Social Statistics (OECD Publishing, 2011).

[6] Eyer, J. & Corey, G. Energy storage for the Electricity Grid: Benefits and Market Potential Assessment Guide. Tech. Rep., Sandia National Laboratories (2010).

[7] Ibrahim, H., Ilinca, A. & Perron, J. Energy storage systems–Characteristics and comparisons. *Renewable and Sustainable Energy Reviews* **12**, 1221–1250 (2008).

[8] Hittinger, E., Whitacre, J. F. & Apt, J. What properties of grid energy storage are most valuable? *Journal of Power Sources* **206**, 436–449 (2012).

[9] Rugolo, J. & Aziz, M. J. Electricity storage for intermittent renewable sources. *Energy & Environmental Science* **5**, 7151–7160 (2012).

[10] Rugolo, J., Huskinson, B. & Aziz, M. J. Model of Performance of a Regenerative Hydrogen Chlorine Fuel Cell for Grid-Scale Electrical Energy Storage. *Journal of the Electrochemical Society* **159**, B133–B144 (2012).

[11] Huskinson, B., Rugolo, J., Mondal, S. K. & Aziz, M. J. A high power density, high efficiency hydrogen–chlorine regenerative fuel cell with a low precious metal content catalyst. *Energy & Environmental Science* **5**, 8690–8698 (2012).

[12] Bommaraju, T., Chen, C. & Birss, V. Deactivation of Thermally Formed RuO_2+ TiO_2 Coatings During Chlorine Evolution: Mechanisms and Reactivation Measures. In Moorhouse, J. (ed.) *Modern Chlor-Alkali Technology*, 57–81 (Blackwell Science, Ltd., London, 2001).

[13] Rugolo, J. *Electricity Storage and the Hydrogen-Chlorine Fuel Cell*. Ph.D. thesis, Harvard University, Cambridge, MA (2010).

[14] Huskinson, B. & Aziz, M. J. Performance Model of a Regenerative Hydrogen Bromine Fuel Cell for Grid-Scale Energy Storage. *Energy Science and Technology* **5**, 1–16 (2013).

[15] Huskinson, B. *et al.* A Metal-Free Organic-Inorganic Aqueous Flow Battery. *Nature* **505**, 195–198 (2014).

[16] Mellentine, J. A., Culver, W. J. & Savinell, R. F. Simulation and optimization of a flow battery in an area regulation application. *Journal of Applied Electrochemistry* **41**, 1167–1174 (2011).

[17] Gileadi, E. *et al.* An electrochemically regenerative hydrogen–chlorine energy storage system for electric utilities. *Journal of Power Sources* **2**, 191–200 (1977).

[18] Savinell, R. & Fritts, S. Theoretical performance of a hydrogen-bromine rechargeable SPE fuel cell. *Journal of Power Sources* **22**, 423–440 (1988).

[19] Yeo, R. & Chin, D. A Hydrogen-Bromine Cell for Energy Storage Applications. *Journal of the Electrochemical Society* **127**, 549–555 (1980).

[20] Yeo, R., McBreen, J., Tseung, A., Srinivasan, S. & McElroy, J. An electrochemically regenerative hydrogen-chlorine energy storage system: electrode kinetics and cell performance. *Journal of Applied Electrochemistry* **10**, 393–404 (1980).

[21] Thomassen, M., Sandnes, E., Børresen, B. & Tunold, R. Evaluation of concepts for hydrogen – chlorine fuel cells. *Journal of Applied Electrochemistry* **36**, 813–819 (2006).

[22] Chin, D., Yeo, R., McBreen, J. & Srinivasan, S. An Electrochemically Regenerative Hydrogen-Chlorine Energy Storage System. *Journal of the Electrochemical Society* **126**, 713–720 (1979).

[23] Livshits, V., Ulus, A. & Peled, E. High-power H_2/Br_2 fuel cell. *Electrochemistry communications* **8**, 1358–1362 (2006).

[24] House, K. Z., House, C. H., Schrag, D. P. & Aziz, M. J. Electrochemical acceleration of chemical weathering for carbon capture and sequestration. *Energy Procedia* **1**, 4953–4960 (2009).

[25] House, K. Z., House, C. H., Schrag, D. P. & Aziz, M. J. Electrochemical Acceleration of Chemical Weathering as an Energetically Feasible Approach to Mitigating Anthropogenic Climate Change. *Environmental Science & Technology* **41**, 8464–8470 (2007).

[26] Thomassen, M., Børresen, B., Hagen, G. & Tunold, R. Chlorine reduction on platinum and ruthenium: the effect of oxide coverage. *Electrochimica Acta* **50**, 1157–1167 (2005).

[27] Gasteiger, H., Panels, J. & Yan, S. Dependence of PEM fuel cell performance on catalyst loading. *Journal of Power Sources* **127**, 162–171 (2004).

[28] Thomassen, M., Børresen, B., Hagen, G. & Tunold, R. H_2/Cl_2 fuel cell for co-generation of electricity and HCl. *Journal of Applied Electrochemistry* **33**, 9–13 (2003).

[29] Neyerlin, K., Gu, W., Jorne, J. & Gasteiger, H. Study of the exchange current density for the hydrogen oxidation and evolution reactions. *Journal of the Electrochemical Society* **154**, B631–B635 (2007).

[30] Yeo, R. & McBreen, J. Transport properties of Nafion membranes in electrochemically regenerative hydrogen/halogen cells. *Journal of the Electrochemical Society* **126**, 1682–1687 (1979).

[31] Nuttall, L., McElroy, J., Srinivasan, S. & Hart, T. Feasibility study of a regenerative solid polymer electrolyte fuel cell system using hydrogen/chlorine reactants for high efficiency energy storage. In *Alternative energy sources; Proceeding of the Miami International Conference*, A79–34106 13–44 (Miami Beach, Fl, 1977).

[32] Balko, E., McElroy, J. & Laconti, A. Halogen acid electrolysis in solid polymer electrolyte cells. *International Journal of Hydrogen Energy* **6**, 577–587 (1981).

[33] Anderson, E., Taylor, E., Wilemski, G. & Gelb, A. A high performance hydrogen/chlorine fuel cell for space power applications. *Journal of Power Sources* **47**, 321–328 (1994).

[34] Beer, H. The invention and industrial development of metal anodes. *Journal of the Electrochemical Society* **127**, 303C–307C (1980).

[35] Trasatti, S. Electrocatalysis in the anodic evolution of oxygen and chlorine. *Electrochimica Acta* **29**, 1503–1512 (1984).

[36] Trasatti, S. Physical electrochemistry of ceramic oxides. *Electrochimica Acta* **36**, 225–241 (1991).

[37] Ardizzone, S., Carugati, A., Lodi, G. & Trasatti, S. Surface Structure of Ruthenium Dioxide Electrodes and Kinetics of Chlorine Evolution. *Journal of the Electrochemical Society* **129**, 1689–1693 (1982).

[38] Lodi, G., Sivieri, E., Battisti, A. & Trasatti, S. Ruthenium dioxide-based film electrodes. *Journal of Applied Electrochemistry* **8**, 135–143 (1978).

[39] Mondal, S. K., Rugolo, J. & Aziz, M. J. Alloy Oxide Electrocatalysts for Regenerative Hydrogen-Halogen Fuel Cell. In He, T., Swider-Lyons, K. E., Park, B. & Kohl, P. (eds.) *MRS Proceedings* (2011).

[40] Bard, A. J. & Faulkner, L. R. Bulk Electrolysis Methods. In *Electrochemical Methods*, 417–470 (John Wiley & Sons, 2001).

[41] Beckmann, R. & Lüke, B. Know-how and Technology - Improving the Return on Investment for Conversions, Expansions, and New Chlorine Plants. In Moorhouse, J. (ed.) *Modern Chlor-Alkali Technology*, 196–212 (Blackwell Science, Ltd., London, 2001).

[42] Beer, H. Coating of protected electrocatalytic material on an electrode. **US Patent 3,933,616** (1976).

[43] Duvigneaud, P. & Coussement, A. Effect of chlorine on solid solution formation in ruthenium titanium dioxide coatings. *Journal of Solid State Chemistry* **52**, 22–31 (1984).

[44] Harrison, J. The oxidation of chloride ions and bromide ions on ruthenium dioxide electrodes. *Journal of Electroanalytical Chemistry* **225**, 159–175 (1987).

[45] Trasatti, S. Progress in the understanding of the mechanism of chlorine evolution at oxide electrodes. *Electrochimica Acta* **32**, 369–382 (1987).

[46] Aromaa, J. & Forsén, O. Evaluation of the electrochemical activity of a Ti–RuO_2–TiO_2 permanent anode. *Electrochimica Acta* **51**, 6104–6110 (2006).

[47] Hepel, T., Pollak, F. H. & O'Grady, W. E. Chlorine Evolution and Reduction Processes at Oriented Single-Crystal RuO_2 Electrodes. *Journal of the Electrochemical Society* **133**, 69–75 (1986).

[48] Ardizzone, S., Fregonara, G. & Trasatti, S. "Inner" and "outer" active surface of RuO_2 electrodes. *Electrochimica Acta* **35**, 263–267 (1990).

[49] Arikado, T., Iwakura, C. & Tamura, H. Electrochemical behaviour of the ruthenium oxide electrode prepared by the thermal decomposition method. *Electrochimica Acta* **22**, 513–518 (1977).

[50] Lodi, G., Bighi, C. & de Asmundis, C. Deposition and characterization of RuO_2 films on various substrates. *Materials Chemistry* **1**, 177–187 (1976).

[51] Chen, R. *et al.* Anodic Electrocatalytic Coatings for Electrolytic Chlorine Production: A Review. *Zeitschrift für Physikalische Chemie* 1–16 (2012).

[52] Loučka, T. The reason for the loss of activity of titanium anodes coated with a layer of RuO_2 and TiO_2. *Journal of Applied Electrochemistry* **7**, 211–214 (1977).

[53] Shrivastava, P. & Moats, M. Wet film application techniques and their effects on the stability of RuO_2–TiO_2 coated titanium anodes. *Journal of Applied Electrochemistry* **39**, 107–116 (2009).

[54] Burke, L. & McCarthy, M. Modification of the electronic transfer properties of Co_3O_4 as required for its use in DSA-type anodes. *Journal of the Electrochemical Society* **135**, 1175–1179 (1988).

[55] Boggio, R., Carugati, A. & Trasatti, S. Electrochemical surface properties of Co_3O_4 electrodes. *Journal of Applied Electrochemistry* **17**, 828–840 (1987).

[56] Da Silva, L. M., Boodts, J. & DeFaria, L. A. 'In situ' and 'ex situ' characterization of the surface properties of the $RuO_2(x)+ Co_3O_4(1- x)$ system. *Electrochimica Acta* **45**, 2719–2727 (2000).

[57] Da Silva, L. M., Boodts, J. & De Faria, L. A. Oxygen evolution at $RuO_2(x)+ Co_3O_4(1-x)$ electrodes from acid solution. *Electrochimica Acta* **46**, 1369–1375 (2001).

[58] Makarova, M. V. *et al.* The electrocatalytic behavior of $Ru_{0.8}Co_{0.2}O_2$–x—the effect of particle shape and surface composition. *Electrochimica Acta* **53**, 2656–2664 (2008).

[59] Hamdani, M., Singh, R. & Chartier, P. Co_3O_4 and Co-Based Spinel Oxides Bifunctional Oxygen Electrodes. *International Journal of Electrochemical Science* **5**, 556–577 (2010).

[60] Morita, M., Iwakura, C. & Tamura, H. The anodic characteristics of manganese dioxide electrodes prepared by thermal decomposition of manganese nitrate. *Electrochimica Acta* **22**, 325–328 (1977).

[61] Morita, M., Iwakura, C. & Tamura, H. The anodic characteristics of massive manganese oxide electrode. *Electrochimica Acta* **24**, 357–362 (1979).

[62] Davidson, C. R. Halogen evolution with improved anode catalyst. **US Patent 4,333,805** (1982).

[63] Macounová, K., Makarova, M., Jirkovský, J., Franc, J. & Krtil, P. Parallel oxygen and chlorine evolution on $Ru_{1x}Ni_{x}O_{2y}$ nanostructured electrodes. *Electrochimica Acta* **53**, 6126–6134 (2008).

[64] Gaudet, J., Tavares, A., Trasatti, S. & Guay, D. Physicochemical Characterization of Mixed RuO_2-SnO_2 Solid Solutions. *Chemistry Of Materials* **17**, 1570–1579 (2005).

[65] Iwakura, C., Inai, M., Uemura, T. & Tamura, H. The anodic evolution of oxygen and chlorine on foreign metal-doped SnO_2 film electrodes. *Electrochimica Acta* **26**, 579–584 (1981).

[66] Comninellis, C. & Vercesi, G. Problems in DSA® coating deposition by thermal decomposition. *Journal of Applied Electrochemistry* **21**, 136–142 (1991).

[67] Ardizzone, S. & Trasatti, S. Interfacial properties of oxides with technological impact in electrochemistry. *Advances in colloid and interface science* **64**, 173–251 (1996).

[68] Coteiro, R., Teruel, F., Ribeiro, J. & Andrade, A. Effect of solvent on the preparation and characterization of DSA®-type anodes containing RuO_2-TiO_2-SnO_2. *Journal of the Brazilian Chemical Society* **17**, 771–779 (2006).

[69] Price charts. URL `http://www.platinum.matthey.com/prices/price-charts`.

[70] USGS National Minerals Informaiton Center. Cobalt. Tech. Rep., U.S. Geological Survey (2013).

[71] USGS National Minerals Informaiton Center. Nickel. Tech. Rep., U.S. Geological Survey (2013).

[72] USGS National Minerals Informaiton Center. Tin. Tech. Rep., U.S. Geological Survey (2013).

[73] USGS National Minerals Informaiton Center. Titanium and titanium dioxide. Tech. Rep., U.S. Geological Survey (2013).

[74] USGS National Minerals Informaiton Center. Manganese. Tech. Rep., U.S. Geological Survey (2013).

[75] Cullity, B. The Determination of Crystal Structure. In *Elements of X-Ray Diffraction*, 297–323 (Addison-Wesley, 1956).

[76] Sheasby, J. S. The Oxidation of Niobium in the Temperature Range 450 °–720 ° C. *Journal of the Electrochemical Society* **115**, 695–700 (1968).

[77] Norman, N. Metallic oxide phases of niobium and tantalum I. X-ray investigations. *Journal of the Less Common Metals* **4**, 52–61 (1962).

[78] Roberson, J. A. & Rapp, R. A. Electrical properties of NbO and NbO_2. *Journal of Physics and Chemistry of Solids* **30**, 1119–1124 (1969).

[79] Kreutzer, H., Yarlagadda, V. & Van Nguyen, T. Performance Evaluation of a Regenerative Hydrogen-Bromine Fuel Cell. *Journal of the Electrochemical Society* **159**, F331–F337 (2012).

[80] Zhang, R. & Weidner, J. W. Analysis of a gas-phase Br_2–H_2 redox flow battery. *Journal of Applied Electrochemistry* **41**, 1245–1252 (2011).

[81] Lide, D. CODATA Key Values for Thermodynamics. CRC Handbook of Chemistry and Physics, 91st Edition (2005).

[82] Lide, D. Electrochemical Series. CRC Handbook of Chemistry and Physics, 92nd Edition (2011).

[83] Novotny, P. & Sohnel, O. Densities of binary aqueous solutions of 306 inorganic substances. *Journal of Chemical and Engineering Data* **33**, 49–55 (1988).

[84] Baldwin, R. NASA Technical Memorandum 89862: Electrochemical performance and transport properties of a Nafion membrane in a hydrogen-bromine cell environment. Tech. Rep., NASA (1987).

[85] Sone, Y., Ekdunge, P. & Simonsson, D. Proton Conductivity of Nafion 117 as Measured by a Four-Electrode AC Impedance Method. *Journal of the Electrochemical Society* **143**, 1254–1259 (1996).

[86] Bard, A. J. & Faulkner, L. R. Kinetics of Electrode Reactions. In *Electrochemical Methods*, 87–136 (John Wiley & Sons, 2001).

[87] White, R. E., Lorimer, S. E. & Darby, R. Prediction of the Current Density at an Electrode at Which Multiple Electrode Reactions Occur under Potentiostatic Control. *Journal of the Electrochemical Society* **130**, 1123–1126 (1983).

[88] Mastragostino, M. & Gramellini, C. Kinetic study of the electrochemical processes of the bromine/bromide aqueous system on vitreous carbon electrodes. *Electrochimica Acta* **30**, 373–380 (1985).

[89] Wilke, C. & Chang, P. Correlation of diffusion coefficients in dilute solutions. *A.I.Ch.E. Journal* **1**, 264–270 (1955).

[90] Reddy, K. & Doraiswamy, L. Estimating liquid diffusivity. *Industrial & Engineering Chemistry Fundamentals* **6**, 77–79 (1967).

[91] Laliberté, M. Model for calculating the viscosity of aqueous solutions. *J. Chem. Eng. Data* **52**, 321–335 (2007).

[92] Beckwith, R., Wang, T. & Margerum, D. Equilibrium and kinetics of bromine hydrolysis. *Inorganic Chemistry* **35**, 995–1000 (1996).

[93] Liebhafsky, H. The equilibrium constant of the bromine hydrolysis and its variation with temperature. *Journal of the American Chemical Society* **56**, 1500–1505 (1934).

[94] Wasmus, S. & Küver, A. Methanol oxidation and direct methanol fuel cells: a selective review. *Journal of Electroanalytical Chemistry* **461**, 14–31 (1999).

[95] Aricò, A. S. Comparison of Ethanol and Methanol Oxidation in a Liquid-Feed Solid Polymer Electrolyte Fuel Cell at High Temperature. *Electrochemical and solid-state letters* **1**, 66 (1999).

[96] Bagotzky, V. S. & Vassilyev, Y. B. Mechanism of electro-oxidation of methanol on the platinum electrode. *Electrochimica Acta* **12**, 1323–1343 (1967).

[97] Carrette, L., Friedrich, K. A. & Stimming, U. Fuel cells: principles, types, fuels, and applications. *ChemPhysChem* **1**, 162–193 (2000).

[98] Zhu, Y., Ha, S. Y. & Masel, R. I. High power density direct formic acid fuel cells. *Journal of Power Sources* **130**, 8–14 (2004).

[99] Rice, C., Ha, S., Masel, R. I. & Wieckowski, A. Catalysts for direct formic acid fuel cells. *Journal of Power Sources* **115**, 229–235 (2003).

[100] Rice, C. *et al.* Direct formic acid fuel cells. *Journal of Power Sources* **111**, 83–89 (2002).

[101] Park, S., Vohs, J. M. & Gorte, R. J. Direct oxidation of hydrocarbons in a solid-oxide fuel cell. *Nature* **404**, 265–267 (2000).

[102] Hori, Y. Electrochemical CO_2 Reduction on Metal Electrodes . In Vayenas, C. (ed.) *Modern Aspects of Electrochemistry*, 89–189 (Springer, 2008).

[103] Barton Cole, E. *et al.* Using a One-Electron Shuttle for the Multielectron Reduction of CO_2 to Methanol: Kinetic, Mechanistic, and Structural Insights. *Journal of the American Chemical Society* **132**, 11539–11551 (2010).

[104] de Tacconi, N. R. *et al.* Electrocatalytic Reduction of Carbon Dioxide Using Pt/C-TiO_2 Nanocomposite Cathode. *Electrochemical and solid-state letters* **15**, B5 (2012).

[105] Conant, J. B., Kahn, H. M., Fieser, L. F. & Kurtz, S. S., Jr. An Electrochemical Study of the Reversible Reduction of Organic Compounds. *Journal of the American Chemical Society* **44**, 1382–1396 (1922).

[106] Guin, P., Das, S. & al, e. Electrochemical reduction of quinones in different media: a review. *International Journal of Electrochemistry* **2011**, 1–22 (2011).

[107] Conant, J. B. & Fieser, L. F. Free and total energy changes in the reduction of quinones. *Journal of the American Chemical Society* **44**, 2480–2493 (1922).

[108] Conant, J. B. & Fieser, L. F. Reduction potentials of quinones. I. The effect of the solvent on the potentials of certain benzoquinones. *Journal of the American Chemical Society* **45**, 2194–2218 (1923).

[109] Conant, J. B. & Fieser, L. F. Reduction potentials of quinones. II. The potentials of certain derivatives of benzoquinone, naphthoquinone and anthraquinone. *Journal of the American Chemical Society* **46**, 1858–1881 (1924).

[110] Gordon, O. W., Plattner, E. & Doppenberg, F. Production of pulp by the soda-anthraquinone process (SAP) with recovery of the cooking chemicals. **US Patent 5,595,628** (1997).

[111] Crossley, M. L. The Separation of Mono-B-, 2, 6-and 2, 7-Sulfonic Acids of Anthraquinone. *Journal of the American Chemical Society* **37**, 2178–2181 (1915).

[112] USGS National Minerals Information Center. Bromine. Tech. Rep., U.S. Geological Survey (2010).

[113] USGS National Minerals Information Center. Vanadium. Tech. Rep., U.S. Geological Survey (2012).

[114] Pourbaix, M. *Atlas of Electrochemical Equilibria in Aqueous Solutions* (National Association of Corrosion Engineers, Houston, TX, 1974).

[115] Bard, A. J. & Faulkner, L. R. *Electrochemical Methods.* Fundamentals and Applications (John Wiley & Sons, 2001), 2nd edn.

[116] Weber, A. Z. *et al.* Redox flow batteries: a review. *Journal of Applied Electrochemistry* **41**, 1137–1164 (2011).

[117] Nawar, S., Huskinson, B. & Aziz, M. J. Benzoquinone-Hydroquinone Couple for Flow Battery. In *MRS Proceedings: 2012 Fall Meeting* (2013).

[118] Huskinson, B., Nawar, S., Gerhardt, M. R. & Aziz, M. J. Novel Quinone-Based Couples for Flow Batteries. *ECS Transactions* **53**, 101–105 (2013).

[119] LaMer, V. K. & Baker, L. E. The effect of substitution on the free energy of oxidation-reduction reactions. I. Benzoquinone derivatives. *Journal of the American Chemical Society* **44**, 1954–1964 (1922).

[120] Skyllas-Kazacos, M., Chakrabarti, M. H., Hajimolana, S. A., Mjalli, F. S. & Saleem, M. Progress in Flow Battery Research and Development. *Journal of the Electrochemical Society* **158**, R55 (2011).

[121] Skyllas-Kazacos, M., Kasherman, D., Hong, D. R. & Kazacos, M. Characteristics and performance of 1 kW UNSW vanadium redox battery. *Journal of Power Sources* **35**, 399–404 (1991).

Colophon

This thesis was typeset using LaTeX, originally developed by Leslie Lamport and based on Donald Knuth's TeX. The body text is set in 12 point Arno Pro, designed by Robert Slimbach in the style of book types from the Aldine Press in Venice, and issued by Adobe in 2007. A template, which can be used to format a PhD thesis with this look and feel, has been released under the permissive MIT (x11) license, and can be found online at github.com/suchow/ or from the author at suchow@post.harvard.edu.